Structure-based Search for novel c-di-AMP Synthase Inhibiting Fragments

Dissertation

for the award of the degree

"Doctor rerurm naturalium"

of the Georg-August-Universität Göttingen

within the doctoral program

"Biomolecules: Structure-Function-Dynamics"

of the Georg-August University School of Science (GAUSS)

Submitted by

Tim Benedict Garbers

from Buchholz in der Nordheide

Göttingen, 2022

Members of the thesis advisory committee

Prof. Dr. Ralf Ficner (Reviewer 1)
Georg-August-University Göttingen
Department of Molecular Structural Biology

Prof. Dr. Jörg Stülke (Reviewer 2)
Georg-August-University Göttingen
Department of General Microbiology

Prof. Dr. Kai Tittmann
Georg-August-University Göttingen
Department of Molecular Enzymology

Members of the examination board

Prof. Dr. Carsten Lüder
University Medical Center Göttingen
Department of Medical Microbiology

Prof. Dr. Kai Heimel
Georg-August-University Göttingen
Department of Microbial Cell Biology

Prof. Dr. Ivo Feußner
Georg-August-University Göttingen
Department of Plant Biochemistry

Date of oral examination: 17th January, 2023

Table of contents

1 Introduction

The rise of antimicrobial resistance among bacteria and fungi over the last decades endangers effective health care and has a drastic influence on economy(Lee Ventola, 2015). The observed increase of antibiotic resistance is directly caused by the misuse and overuse of antibiotics worldwide (Mittal *et al*, 2020). Combined with the lack of both, investments, and progress in the drug development pipelines for new antibiotics, the world is now facing the problem that resistance mechanisms have evolved for nearly every antibiotic, regardless of the antibiotic class or target (Altarac *et al*, 2021). Thus, there is an urgent need for new and novel classes of antibiotics to be able to treat the increasing cases of infections with multi-resistant bacteria.

Multi-resistant bacteria are directly responsible for growing costs in the public health sector and an increased mortality rate (O'Neill, 2014): According to WHO estimations, infections with antibiotic resistant bacteria cause around 50.000 deaths per year in North America and Europe and more than 700.000 deaths per year worldwide (WHO, 2019). If the misuse of antibiotics will not be reduced and no new antibiotics are developed, the worldwide death toll due to antibiotic resistance is expected to reach 10 million deaths annually by 2050 (Fig. 1.1). It will thus outnumber the estimated deaths from cancer, cholera, tetanus, and measles combined (O'Neill, 2016). The expected rise in mortality will be mostly due to the increased pressure on the modern health care system, as simple infections will once more become potentially deadly. Without the ability to treat simple bacterial infections with appropriate antibiotics, basic surgical operations and even childbirth could again become life threating. The WHO further predicts that the rise of antibiotic resistant bacteria will be responsible for a loss in the global gross domestic product by 2-3.5 % by the year 2050. This loss is equal to the reduction of the worldwide economic performance caused by the financial crisis in 2008-2009 (WHO, 2019).

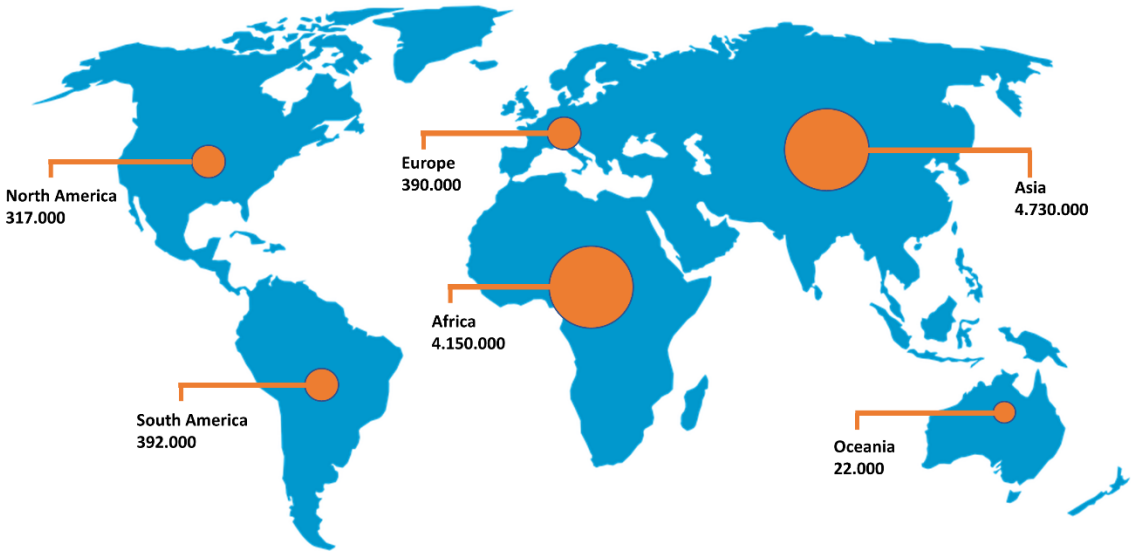

Figure 1.1: Estimated annual death in 2050 due to antibiotic resistant bacteria. The WHO estimates that in 2050, there will be around 10 million deaths annually.

Therefore, there is an urgent need to develop new antibiotics. This thesis focusses on finding inhibitors for the enzyme CdaA, a novel antibiotic target which product cyclic-di-AMP (c-di-AMP) is essential for gram positive bacteria (Stülke & Krüger, 2020). In the first section of the following introduction, the mechanisms of currently used antibiotics and how bacteria develop resistance against them are outlined. The second part explains the role of a novel antibiotic target within the cell and its regulation. The last part describes several methods and strategies used to identify compounds which interact with a protein of interest, and which can serve as starting points for further drug development.

1.1 Antibacterial drugs and resistance mechanism

1.1.1 Antibiotic drugs

Among the different classes of available antibiotics, β-lactams, aminoglycosides, tetracyclines, fluroquinolones, rifamycin, macrolides and folate pathway synthesis inhibitors are most important for treating bacterial infections. These drugs target different pathways in the bacterial cell, like DNA replication, RNA synthesis, cell wall synthesis, folate synthesis or protein production. These antibiotics and their targets are schematically represented in Figure 1.2.

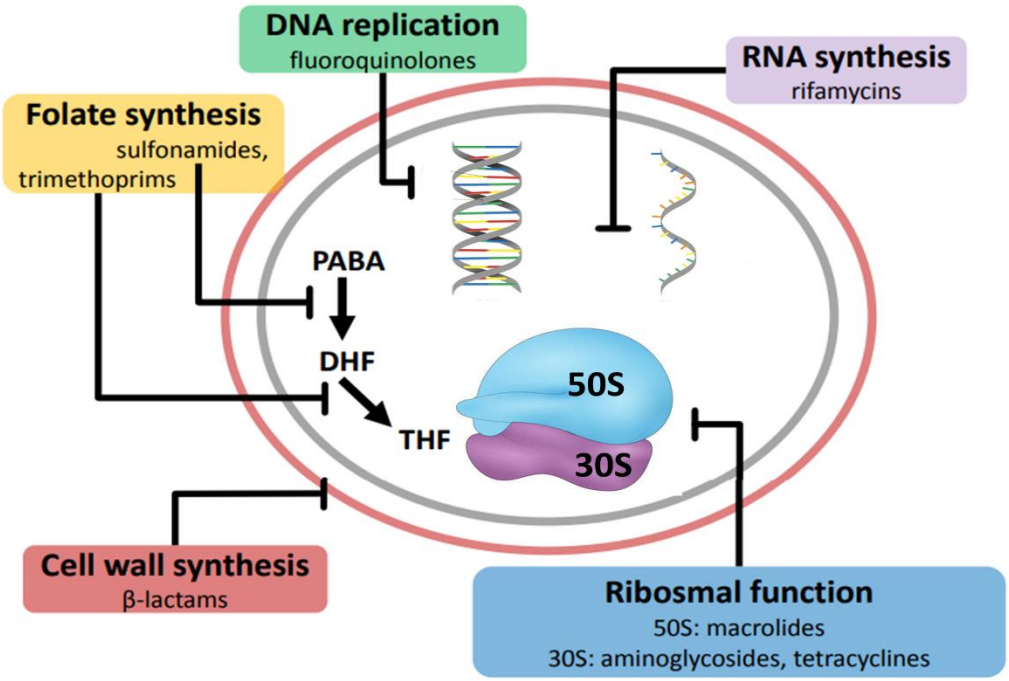

Figure 1.2: Schematic representation of common antibiotics targets. The most commonly used antibiotics, β-lactams, rifamycin, macrolides, tetracycline fluoroquinolones, sulfonamides and trimethoprim, as well as their respective targets, cell wall synthesis, 50S/30S ribosome, RNA synthesis, DNA replication or folate synthesis, are shown. Image was adopted from (van Oosten, 2020).

Penicillin, the first antibiotic from the class of β-lactams is also the most famous antibiotic and was identified by Alexander Fleming in 1928 (Alexander Fleming, 1929). All drugs within the

β-lactam family inhibit the assembly of the bacterial cell wall membrane by binding to so-called penicillin-binding proteins, which catalyze the polymerization of the glycan strand and the crosslinking between the glycan strands and forms an irreversible covalent bond when coming in contact with β-lactams (Beadle *et al*, 2001). Therefore, the penicillin binding proteins can no longer catalyze the crosslinking reaction between the peptidoglycan molecules and thus the bacterial cell wall is not properly formed, which ultimately leads to the rupture of the bacterial cell.

Another class of antibiotics, the sulfonamides, was discovered in the early 1930s in the laboratories of Bayer AG under the supervision of Gerhard Domagk (Otten, 1986). These antibiotics are so-called antimetabolite drugs as they act as competitive inhibitors of the dihydropteroate synthase, a key enzyme in the bacterial folate synthesis pathway, which catalyzes the transformation of para-aminobenzonic acid to dihydropteroate. The folate pathway also delivers essential precursors for nucleic acid biosynthesis. Blocking this pathway does not lead to immediate cell death, but it does inhibit growth and cell division. Derivatives from this family are commonly used in the treatment of allergies and coughs.

Another class of antibiotics, called trimethoprim-like drugs, also acts on the folate synthesis pathway, but at a later stage compared to sulfonamides. Trimethoprim was first used in 1962 to battle infections with pathogenic bacteria. The target of this drug class is the enzyme dihydrofolate reductase, which catalyses the transition of dihydrofolic acid to tetrahydrofolic acid (Eliopoulos & Huovinen, 2001).

Other antibiotics which can be used to fight bacterial infections are found in the family of fluoroquinolones. Members of the fluoroquinolone family inhibit DNA replication by suppressing the DNA-ligase activity of the enzymes DNA-gyrase, topoisomerase type II and topoisomerase IV. All of these enzymes cut the bacterial DNA and re-ligate it to introduce supercoiling. Due to the fluoroquinolone-inhibited ligase activity, these enzymes release DNA with single or double strand breaks, which ultimately lead to cell death (Fàbrega *et al*, 2009).

Another class of antibiotics which influence the interaction of bacterial proteins with genomic DNA are rifamycins. These antibiotics interact with the prokaryotic DNA-dependent RNA polymerase and block the synthesis of RNA by causing steric clashes with the growing RNA chain (Wehrli, 1983). Thus, they inhibit the production of RNA which eventually leads to cell death. Rifamycine was discovered in 1957 from a *Streptomyces mediterranei* culture and was used in 1958 for treating infections with tuberculosis (Sensi, 1983).

The following last three classes of antibiotics all directly interact with the ribosome, thereby inhibiting protein synthesis. The class of tetracyclines was discovered by Benjamin Brugger in 1948 (Brugger, 1948). These antibiotics interact with the 30S ribosome subunit by reversibly binding to its A-site. This prevents the attachment of aminoacyl-tRNA and therefore the growth of the peptide chain (Chopra & Roberts, 2001). The first antibiotics from the class of aminoglycosides were isolated from Streptomyces griseus in 1944 and were directly used in

clinical tries. These antibiotics also bind to the A-site of the 30s ribosome, but instead of inhibiting the growth of the polypeptide chain they alter the conformation of the A-site. The effect of this alteration leads to incorrect translation of the mRNA by codon slipping (Krause *et al*, 2016). The last class of antibiotics interfering with protein biosynthesis are macrolides, which were discovered in 1952. These drugs bind near the P-site of the 50S ribosome in a reversible manner, thereby preventing the peptidyl-transferase from adding an amino acid and inhibiting the elongation of the polypeptide chain (Kricker *et al*, 2021). Independently of the exact mechanism of inhibition, all three antibiotic classes acting on the ribosome cause cell death.

All of the antibiotics described above originate from the “Golden Age” of the antibacterial drug discovery and target well known, major synthesis pathways of bacterial cells (Hutchings *et al*, 2019). After this era, several other antibiotic drugs have entered the market, but with only few exceptions, these new drugs are all members of already known antibiotic classes. For example, cephalosporins and carbapenems entered the market after this era, but they also possess the typical structure of β-lactams antibiotics, making them susceptible to the increasing drug resistance against this antibiotic class (Ali Syed, 2016; Papp-Wallace *et al*, 2011). This is also true for almost every other new drug which entered the market since then, they act on well-known targets with just minor differences in the chemical structure of the drug. As the mechanism of action stays the same, these "follow-ups” offer no real solution in the fight against the rising antibiotic resistance (Melander & Melander, 2017).

1.1.2 Antibiotic resistance mechanisms of bacteria

Bacteria can acquire antibiotic resistance by mainly two different ways: The first route is by mutations in pathways which can confer antibiotic resistance (Martinez, 2014). The second possibility is the acquisition of antibiotic resistance via transformation, conjugation or transposition, all of which mechanisms which are referred to as horizontal gene transfer. Plasmid mediated uptake of extra chromosomal DNA encoding antibiotic resistance is the most common way of how bacteria gain capability to withstand antibiotic drugs (Evans *et al*, 2020).

Antimicrobial resistance mechanism can be divided into four different categories: The first mechanism it the limitation of the drug uptake. This limitation can be caused through several mechanism of action. Staphylococcus aureus is able to thicken its cell well, hindering the antibiotic vancomycin to enter the cell (Cong *et al*, 2020). Often, antibiotic drugs enter the bacteria cell via porin channels. Members of the family of Enterobacteriaceae can reduce the number of porin channels and therefore limit the import of the antibiotic drug (Kong *et al*, 2018). The amino acids of the porin channels can also be altered und thus the selectivity of the channels can be modified to reduce the uptake of antibiotic drugs (Dé *et al*, 2001). Another mechanism is the formation of a biofilm. The thick layer formed consists of polysaccharides,

proteins and DNA and makes it difficult for antibiotic drugs to reach the bacterial cells. Furthermore, bacterial cells in this specific state tends to reduce their metabolic rate, limiting the effect of antibiotic drugs which target metabolism or cell division pathways (Sharma *et al*, 2019).

The second mechanism how bacterial cells can gain resistance towards antibiotic drugs is the inactivation of the antibiotic. This can occur in two different ways: The first possibility is modification of the antibiotic's core structure. The most commonly used group of antibiotic drugs, the β-lactam family, all share the same structural motif, a four-membered β-lactam ring. This ring can be cleaved by proteins of the family β-lactamases, disrupting the drug's capability to bind to penicillin-binding proteins (Furniss *et al*, 2022). The other possibility is modification by addition of chemical groups. This happens most frequently by transferring acetyl, phosphoryl and adenyl groups, with acetylation of the antibiotic drug being the most common modification (Blair *et al*, 2015).

The third mechanism of developing antibiotic resistance is the modification of the antibiotic target within the bacterial cell. This can happen to nearly every target of antibiotic drugs regardless of whether it is a protein or a component?? of the bacterial cell. Gram-positive bacteria developed resistance against antibiotics from the β-lactam family by alteration of their penicillin-binding proteins (Haenni & Moreillon, 2006). Another famous example is the resistance of *Staphylococcus aureus* against the antibiotic vancomycin caused by changes to peptidoglycan precursors (Gardete & Tomasz, 2014).

The last possibility how bacteria can develop resistance against antibiotic drugs are alterations in their efflux system to improve their capability to export antibiotic drugs. One common adaptation is the overexpression of export channels, which can be observed in the gram-negative bacterium *Escherichia coli* (Thanassi *et al*, 1997). Another possibility is to gain the ability to express specific pumps for antibiotic drugs via horizontal gene transfer, for example a transposon element in *Staphylococcus epidermidis* which encodes for a member of the small multidrug resistance efflux pump family and which can provide resistance against ampicillin, erythromycin, and tetracycline (Fuentes *et al*, 2005).

It can be concluded that the possibilities for bacteria to escape antibiotic drugs are very versatile. As a result, there is an urgent need to develop new ways to treat infections with multi-resistant bacteria. One possibility is to use a mixture of two different drugs to treat patients with an infection. One example for this method is how β-lactamase resistant bacteria are treated: a combinatorial therapy consisting of a β-lactam and a β-lactamase inhibitor. Another often-used combination is a mixture of amoxicillin, which binds to the penicillin-binding protein and clavulanic acid, which inhibits β-lactamase proteins (Ball, 2007).

But as antibiotic resistance bacteria are on the rise, novel antibiotics with a new mechanism of action are desperately needed. Nevertheless, search for novel antibiotic drug targets has been very inconclusive in recent years as just two antibiotic drugs with a new mechanism of

action have entered the market since 2000 (WHO, 2019). The antibiotic Obiltoxaximab interacts and therefore blocks directly a pathogenic factor of the bacterium *Bacillus anthracis* (Henning *et al*, 2018). The other, Bezlotoxumab interacts with Toxin B protein of *Clostridium difficile* to neutralize the activity of this protein (Orth *et al*, 2014). One reason for this lack is the low number of potential targets for new antibiotic drugs. The genomics era was thought to deliver various new targets, but the target-directed approach failed to deliver potential new candidates for novel antibiotics.

1.2 Nucleotide-derived second messengers in bacteria

One novel path to specifically target bacteria is the expanding diversity of second messenger nucleotides. These metabolites are involved in the signal transduction, which is an essential mechanism in bacteria to adapt to changes in their direct environment such as temperature, pH or atmosphere. Therefore, bacteria possess many sensors and signal transduction pathways to adapt in a suitable way. Key players in theses pathways are second messengers derived from nucleotides (Thompson & Malone, 2020).

The first second messenger metabolite derived from nucleotides was discovered during studies of the hormone epinephrine and was called cyclic AMP (cAMP). This metabolite was identified in mammalian as well as bacterial cells (Botsford & Harman, 1992; Makman & Sutherland, 1964). However, other nucleotides can form stable cyclic monophosphate forms to serve in signaling pathways as well, like cyclic UMP (cUMP), cyclic CMP (cCMP) and cyclic GMP (cGMP) (Bähre *et al*, 2015; Ashman *et al*, 1963). Investigations using nutritional limitation gave rise to the discovery of linear second messenger guanosine-(penta)-tetraphosphate (p)ppGpp which also originates from a nucleotide (Cashel & Gallant, 1969). In 1987, the first metabolite descended from two nucleotide molecules was discovered and named bis-(3´, 5´)-cyclic-di-guanosine monophosphate (cyclic-di-GMP/c-di-GMP)(Ross *et al*, 1987). In the recent years, many second messenger metabolites derived from nucleotides were discovered in linear, or in cyclic mono-, di-, or tri-nucleotide form (Whiteley *et al*, 2019; Severin & Waters, 2019).

In 2008, the structure of the DNA integrity scanning protein DisA from *Thermotoga maritima* in complex with bis-(3´, 5´)-cyclic di- adenosine monophosphate (cyclic di-AMP/c-di-AMP) was published (Witte *et al*, 2008). Since then, c-di-AMP was shown to be synthesized by a family of proteins which share the diadenylate cyclase (DAC) domain (Commichau *et al*., 2019). Importantly, it has been reported that the c-di-AMP second messenger metabolite is essential for bacteria under standard conditions (Fahmi *et al*., 2017; Gundlach *et al*., 2017) and that it has not been detected in humans. This renders proteins containing a DAC domain as potential targets for the development of new antibiotics.

1.2.1 Enzymes synthesizing c-di-AMP in bacteria

Enzymes comprising a DAC domain were detected in different species, mostly in gram-positive bacteria from the Firmicutes and Actinobacteria groups like the human pathogens *Streptococcus pneumoniae, Staphylococcus aureus* and *Enterococcus faecium*, but also in gram-negative bacteria and archaea (Blötz *et al*., 2017; Corrigan *et al*., 2011; Römling, 2008). These enzymes can be divided into five different classes, namely CdaA, DisA, CdaS, CdaM and CdaZ, which all have the DAC domain in common but differ by additional domains or motifs (Römling, 2008b; Corrigan *et al*, 2011; Blötz *et al*, 2017; Sureka *et al*, 2014). An overview of the domain organization of c-di-Amp generating enzymes is depicted in Figure 1.3.

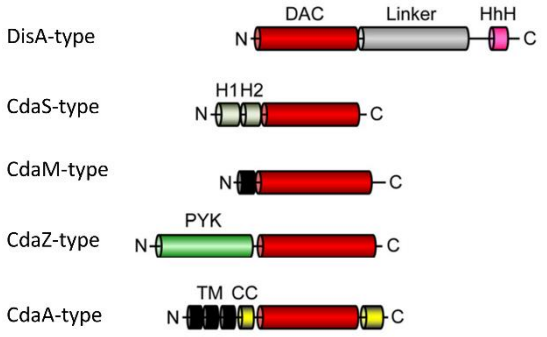

Figure 1.3: Overview of organization of enzymes containing a diadenylate cyclase domain. The conserved DAC domain is represented in red. HhH is a helix-hinge-helix domain, H1 and H2 are inhibitory helices 1 and 2, PYK is a pyruvate kinase-like domain, CC is a coiled-coiled motif, while TM is a transmembrane helix. This Figure was adapted from (Commichau *et al*., 2019).

All DAC proteins depend on divalent cations (Mg^{2+}, Mn^{2+} or Co^{2+}) and they transform two ATP molecules into one molecule c-di-AMP and two molecules of the side product pyrophosphate (Heidemann *et al*., 2019; Tosi *et al*., 2019; Witte *et al*., 2008). Another common feature is the dimerization of DAC proteins as a prerequisite for the synthesis of c-di-AMP. Two DAC domain monomers each binding an ATP molecule need to face each other in order to form one reaction center (Müller *et al*, 2015). While some bacteria from the *Bacillus* genus possess up to three different classes of DAC proteins, many pathogenic bacteria contain just a single class of DAC proteins (Woodward *et al*, 2010; Mehne *et al*, 2013).

1.2.2 Functions of the second messenger c-di-AMP in bacteria

The product of DAC domain containing proteins, c-di-AMP, is involved in many different regulatory cellular processes. Notably, c-di-AMP is the first secondary messenger metabolite identified which can influence the cell not only by regulating the activity of various proteins but also by binding to riboswitches (Gundlach *et al*., 2019; Nelson *et al*., 2013). c-di-AMP plays a major role in various cell processes like DNA damage sensing, gluconeogenesis, regulation of fatty acid synthesis, cell wall homeostasis, inorganic carbon regulation, potassium ion transport, regulating the virulence or regulation of the (p)ppGpp synthesis (Agostoni *et al*., 2018; Bai *et al*., 2014; Gundlach *et al*., 2019; Jackson-Litteken *et al*., 2021; Krüger *et al*., 2021; Selim *et al*., 2021; Witte *et al*., 2008). In the sense of antibiotic drug design, the role of c-di-AMP in potassium homeostasis is the most important regulatory function, as the involvement in the osmotic regulation makes this second messenger metabolite essential (Bai *et al*., 2014;

Gundlach *et al*., 2019; Sureka *et al*., 2014). Potassium ions are the most abundant cations in cells and are the main regulators of maintaining the pH of the cell (Epstein, 2003). The important role of c-di-AMP in potassium regulation is underlined by the fact that cells accumulate c-di-AMP if they face a high external potassium concentration which leads to limited uptake of these ions (Gundlach, *et al*., 2017).

It has been reported that c-di-AMP can influence the activity of various proteins, mostly transporters by binding to their respective RCK_C domain. These proteins are capable of forming a gating component in ion channels like KtrCD from *Bacillus subtilis* or interacting with the transcription factor BusR to negatively regulate the expression of the glycine betaine transporter BusAB (Bandera *et al*., 2021; Gundlach, *et al*., 2017; Pham *et al*., 2018). This underlines that c-di-AMP is not only involved in regulation of potassium levels within the bacterial cell, but also in osmolyte transport, and therefore homeostasis in general.

Another class of proteins which can bind c-di-AMP are proteins which contain the Bateman, also called CBS, domain. Proteins with these domains are capable to bind a wide range of adenine derivates (Meyer *et al*, 2007; Maya-Bernal *et al*, 2017; Anashkin *et al*, 2015). It is important to note that just a minority of them are able to bind c-di-AMP (Devaux *et al*, 2018; Gundlach *et al*, 2019a). These are the Mg^{2+} transporter MgtE, the glycine-betaine-carnitine transporter OpuCA and the protein DarB, which is involved in the regulation of the citric acid cycle and in the regulation of another second messenger metabolite, (p)ppGpp (Gundlach *et al*., 2019; Heidemann *et al*., 2022; Krüger *et al*., 2021, 2022; Schuster *et al*., 2016).

As c-di-AMP is a key player in maintaining the osmolyte homeostasis, its intracellular concentration needs to be tightly regulated, which means it also has to be broken down or secreted. Enzymes which are able to degenerate c-di-AMP are called phosphodiesterases (PDE). In total, four different classes of PDEs have been identified, which can degrade c-di-AMP via hydrolysis similar to the tow-step mechanism for the synthesis (Commichau *et al*., 2019; Manikandan *et al*., 2014).

1.2.3 CdaA, the most prevalent diadenylate cyclase

Many bacteria, mostly gram-positive bacteria, possess at least one enzyme with a DAC domain. The most widespread and, in many pathogenic bacteria (*Staphylococcus aureus*, *Streptococcus pneumoniae*, *Enterococcus faecium)*, only enzyme with a DAC domain is the cyclic-di-adenylate cyclase A (CdaA). CdaA is a membrane bound protein, which consists of three N-terminally located transmembrane helices. These are followed by a linker in the form of a so-called coiled-coil motif and the DAC domain (Fig 1.3). In the nearly all bacteria from the phylum firmicutes, the gene of CdaA is placed gene cluster consisting of CdaA, a regulatory protein CdaR and the glucosamine mutase enzyme GlmM which is conserved in firmicutes (Mehne *et al*, 2013; Rismondo *et al*, 2016; Gibhardt *et al*, 2020).

The first structure of CdaA DAC domain was published in 2015 and was of the protein in complex with ATP and a Mg^{2+}-ion (Rosenberg *et al*, 2015). The crystallized construct misses its three transmembrane helices, as this makes the handling and purification of this construct easier compared to the full-length version. Therefore, it consists just of the N-terminal coiled-coil motif and the DAC domain. In the following years, several structures of CdaA from different organism in various enzymatic states were published (Heidemann *et al*., 2019; Pathania *et al*., 2021; Tosi *et al*., 2019). Notably, if CdaA was crystallized in the inactive APO state, it always exhibited a back-to-back arrangement (Fig 1.4 B), therefore it's not clear if this is a stable structural state or crystallization artefact (more details in the chapter Discussion). Biochemical characterization of the different CdaAs indicated that all of them require a divalent metal ion in order to be catalytically active. Independent of the source organism, all CdaAs seems to be active in the presence of manganese. *Staphylococcus aureus* CdaA is also functional in the presence of magnesium, as opposed to the CdaA from *Listeria monocytogenes,* which is inactive in the presence of magnesium but active in the presence of cobalt. Similarly, the related DAC-domain containing enzyme DisA is only catalytically active in the presence of manganese or magnesium (Heidemann *et al*., 2019; Tosi *et al*., 2019; G. Witte *et al*., 2008).

The DAC domains of DisA, CdaS and CdaA all share an overall similar, globular fold. The DAC domain core is formed by seven parallel and antiparallel β-strands (β1- β7) surrounded by five α-helices (α1- α5) (Fig. 1.4 A) (Rosenberg *et al*, 2015; Witte *et al*, 2008; Hao *et al*, 2022).

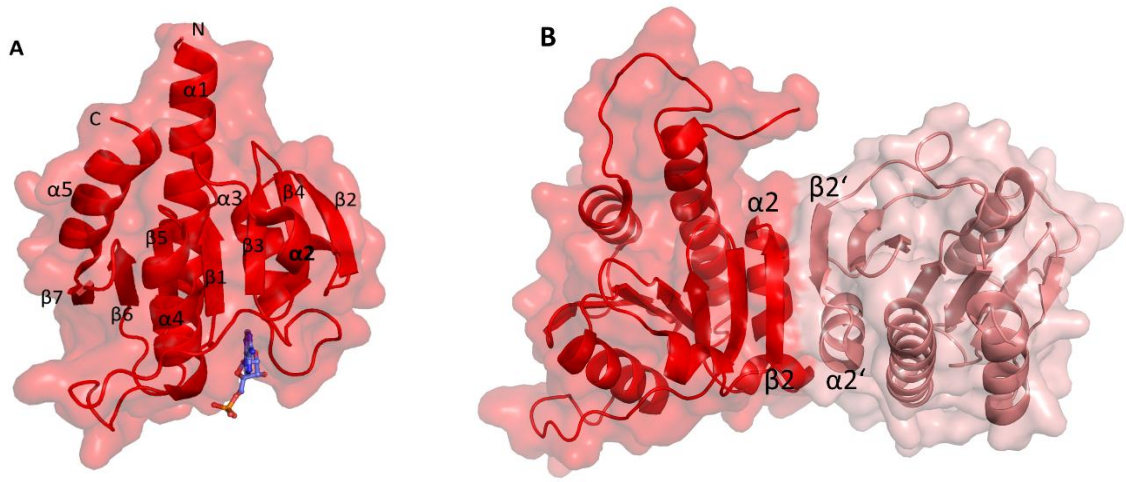

Figure 1.4: Representation of CdaA. **A** Overall structure of CdaA consisting of seven central, slightly twisted β-strands surrounded by five α-helices. AMP is bound to the active site of the enzyme. The protein structure is depicted in *cartoon* mode in red and the *surface* is represented in light red. **B** Representation of back-to-back dimer of CdaA observed in the X-ray structure (PDB-ID: 6HVL,6GYW). The protomers are as *cartoon* and *surface* in red and salmon. The interface of the dimer is formed by the α-helix2, β-strand 2 and their corresponding counterparts from the other protomer

The activity of the enzyme CdaA can be regulated by the two proteins which are encoded in the previously described conserved gene cluster, CdaR and GlmM. CdaR consists of an N-terminally located transmembrane domain followed by four YbbR domains (Barb *et al*, 2010).

It has been shown that this protein interacts with CdaA *via* its Ybbr domains. Depending on the growth conditions and the cellular environment, the enzymatic activity of CdaA can be up- or downregulated by its interaction with CdaR (Gundlach *et al*, 2015; Rismondo *et al*, 2016; Gibhardt *et al*, 2020).

The second protein involved in the regulation of CdaA is the cytosolic phosphoamine mutase GlmM, which synthesizes glucosamine-1-phosphate from the precursor glucosamine-6-phosphate. Therefore, the protein is directly involved in the peptidoglycan biosynthesis pathway (Tavares *et al*, 2000). Upon complex formation with CdaA, the cyclase activity of CdaA is greatly reduced, which marks GlmM as a negative regulator of CdaA. This was shown in different organism and by several experiments (Gibhardt *et al*, 2020; Pathania *et al*, 2021).

1.2.4 CdaA as a new antibiotic target

Bacteria can adapt rapidly to changing environmental conditions and can therefore also quickly adapt to antibiotics, developing an arsenal of escape techniques which can be shared *via* horizontal gene transfer. The WHO declared rising antibiotic resistance a “global health concern” since bacteria and viruses can spread worldwide and are not stopped by national borders (WHO, 2019a). Even in countries with an excellent health care system like Germany, there are still an estimated 10.000 to 15.000 deaths each year due to a lack of efficient antibiotics (German Federal Government, 2020). It will be not enough to just develop new antibiotics in the fight against multi-resistant bacteria (MRSA): The over- and misuse of antibiotics also needs to be reduced (Mallah *et al*, 2022). In 2017, the WHO released a priority list, the so-called “list of the dirty dozen” in which 12 different bacteria strains are listed: For all of these we urgently need new antibiotics to be able to treat infections, as they have become mostly resistant against commonly used antibiotics. Although there was progress in the last years to reduce infections with MRSA, it was nullified by the ongoing corona crisis according to latest reports (Mallah *et al*, 2022). The reasons for this development vary, but it is a fact that the number of patients infected with MRSA increased by around 15 % in the last 3 years (CDC, 2022). Summarized, there is an urgent need to develop new antibiotics to tackle the global health problem caused by increasingly resistant bacteria.

Proteins catalyzing c-di-AMP synthesis and especially CdaA, were previously suggested as possible targets for the development of new antibiotics (Rosenberg *et al*, 2015; Commichau *et al*, 2019). As they occur CdaA fits the majority of requirements which a novel antibiotic target has to fulfill, such as a high degree of conservation among different bacterial species and that deletion of the target should lead to a decreased growth rate. Moreover, it should not have a structural or functional homologue in the human proteome in order to avoid side effects by the potential drug (Hughes & Karlén, 2014). So far, neither enzymes possessing a DAC domain nor c-di-AMP were detected in humans.

Furthermore, it was shown that proteins with a DAC domain are essential in bacteria under normal growth conditions due to their role in controlling the potassium and general osmolyte homeostasis (Gundlach *et al*., 2017; Gundlach *et al*., 2017b). A deletion of the gene encoding a protein with a DAC domain also let to a higher sensitivity to β-lactams like methicillin, oxacillin or cefuroxime. This increased sensitivity might be a result of a reduced stability of the cell wall (Dengler *et al*, 2013). Moreover, in many pathogenic bacteria, like *S. aureus, S. pneumoniae, L. monocytogenes* or *E. faecium,* CdaA is the only enzyme with an DAC domain, rendering this protein an ideal target for the development of a new antibiotic.

1.2.5 Inhibitors of DAC containing proteins

Enzymes with a DAC domain are suitable targets for the development of new antimicrobial drugs because they catalyze the synthesis of the essential second messenger c-di-AMP. Substances which were able to inhibit this catalytic activity were first reported for the enzyme DisA (Müller *et al*, 2015; Zheng *et al*, 2014; Opoku-Temeng & Sintim, 2016b, 2016a). One of the first inhibitors for DisA was the ATP analogue 3´-deoxy-ATP, which misses its 3´-hydroxyl group, and therefore cannot be processed to c-di-AMP. This competitive inhibitor strongly reduces the activity of DisA, with an IC_{50} (50% inhibitory concentration) of 3.8 µM (Müller *et al*., 2015). Nevertheless, this can hardly be used as antibiotic drug as it is very similar to ATP and would thus affect all proteins requiring ATP.

The screening of a 2000 compounds library revealed a well-known inhibitor for ATP-binding enzymes, suramin, as a potential candidate for inhibiting DisA. Docking experiments showed that this drug binds in the active site of DisA which was further proven by *in vitro* experiments. Suramin is able to inhibit DisA with an IC_{50} of 1.1 µM (Opoku-Temeng & Sintim, 2016a). Another compound which inhibits DisA *in vitro* is theaflavin digallate (TF-dG), featuring an IC_{50} of 3.4 µM. Interestingly, additional experiments showed that the inhibitory effect of this compound is non-competitive with ATP, suggesting an allosteric inhibition (Opoku-Temeng & Sintim, 2016b). The small compound bromophenol thiohydantoin (Br-TH) is able to inhibit the cyclase activity of DisA, with an IC_{50} value of 56 µM. Br-TH was discovered by screening a kinase inhibitor library to uncover new ATP-competitive inhibitors. However, the authors stated that the inhibitory effect of BR-TH towards the enzymatic activity of DisA is non-competitive with ATP (Zheng *et al*, 2014). BR-TH was also tested against the protein CdaA from *Enterococcus faecalis*. This study revealed that this compound not only exhibits inhibitory effects against CdaA *in vitro,* but is also able to reduce the bacterial growth and biofilm formation *in vitro*. Interestingly, docking experiments showed that Br-TH most likely binds to the active site of CdaA, therefore serving as a competitive inhibitor against this enzyme, which is in direct contrast to the earlier findings regarding the protein DisA (Chen *et al*, 2018). Screening of a kinase inhibitor library against an N-terminal truncated CdaA construct from *Streptococcus suis* revealed the strong inhibitory effect of 2,2′-dihydroxy-1,1′-dinapthyldisulfide (IPA-3), with an IC_{50} value of 33.22 µM. Moreover, this compound was able to reduce the growth rate of

various gram-positive pathogenic bacterial strains *in vivo* but not the growth of the gram-negative bacteri*um Escherichia coli*. A model from *Streptococcus suis* CdaA calculated by I-Tasser was used to carry out docking simulations. These simulations, combined with a molecular dynamics simulation, revealed that IPA-3 is most likely interacting with strongly conserved residues in the active center of CdaA (Li *et al*, 2022a). All of the known inhibitors of protein containing a DAC domain contain at least one aromatic ring (Fig. 1.5).

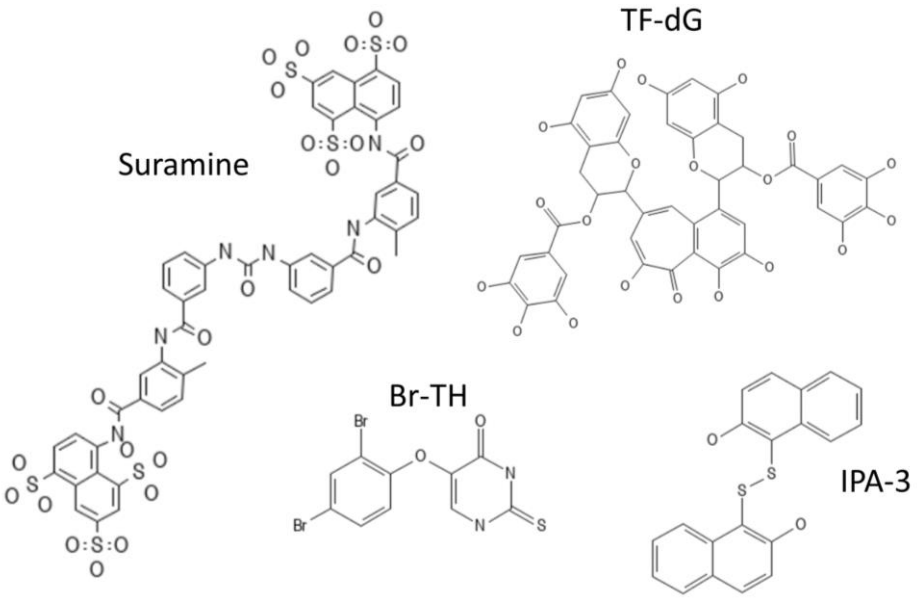

Figure 1.5: Skeletal presentation of the four known inhibitor of proteins consisting of a DAC domain, Suramine, Bromophenol-Thiohydantonin (Br-TH), theaflavin digallate(TF-dG) and 2,2'-dihydroxy-1,1'-dinapthyldisulfide (IPA-3).

1.3 Drug design

Drug design describes the inventive progress to develop or identify a small molecule which is able to activate or inhibit the function of a biomolecule. Several different methods exist to reach this aim. Some of them, including high-throughput screening and structure-based drug design are described in detail in the following part.

1.3.1 Development of inhibitors by high-throughput screening

Three decades ago, large pharma companies invested billions of dollars to set up the infrastructure required for high-throughput screening (HTS). Enormous effort was made to establish libraries consisting of thousands or even millions of compounds and to also establish the robotic automation of the screening process itself (Zweigenbaum *et al*, 1999; Oldenburg *et al*, 1998). These libraries typically consist of drug- or lead-like compounds which have a

molecular weight of about 500 Da and follow Lipinskis rule of 5 (less than five hydrogen bond donors and less than 10 hydrogen bond acceptors) (Lipinski *et al*, 2001). These libraries deliver hits which already bind the target with an affinity in the micro- to nanomolar range and greatly reduce the activity of the protein of interest (Szymański *et al*, 2011). One significant problem in HTS campaigns is the large number of false-positive hits, therefore all hits identified in the screening need to be validated (Sink *et al*, 2010). Afterwards, the validated hits are optimized to achieve compounds with better biological and physiochemical properties. Figure 1.6 illustrates a typical HTS approach.

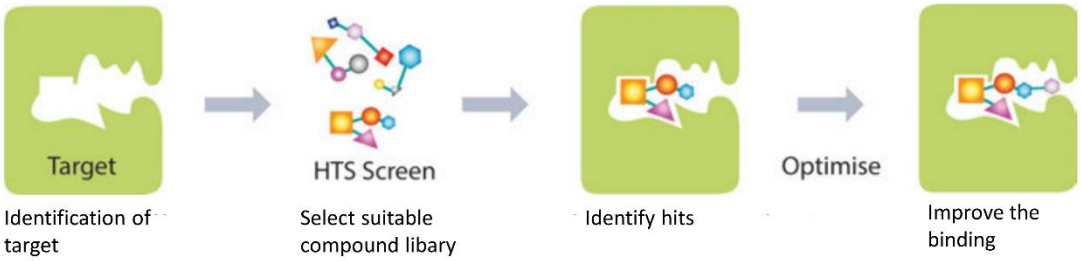

Figure 1.6: Depiction of an HTS workflow. The first step is the identification of a target which fulfills all given requirements. The next step is the screening for inhibitory compounds by combining a suitable assay with a compound library. The resulting hits are chemically improved to achieve better binding between the follow-up compound and the protein of interest. Figure was adapted from (FitzGerald, 2021).

Unfortunately, many of the hits fail to make it to the market, even after several rounds of improvements. The main reason for this is that even if libraries can contain millions of compounds, they can lack the required complexity and insufficiently cover the available chemical space which is needed to identify inhibitors against novel targets (Karawajczyk *et al*, 2015). Another reason for the failing of HTS approaches is the limited chemical flexibility of the compounds as they are already often lead-like compounds with a relatively large size. Moreover, drugs deriving from HTS campaigns often suffer the problem of poor solubility or oral bioavailability (Di & Kerns, 2012).

1.3.2 Fragment-based drug discovery

Over the last 30 years, fragment-based drug discovery (FBDD) has emerged as an efficient way to develop lead compounds which has finally led to FDA/EMA approved drugs. Today, there are six FBDD derived drugs which are now commonly used in oncology (Hamilton *et al*, 2022). These drugs are depicted in Figure 1.7.

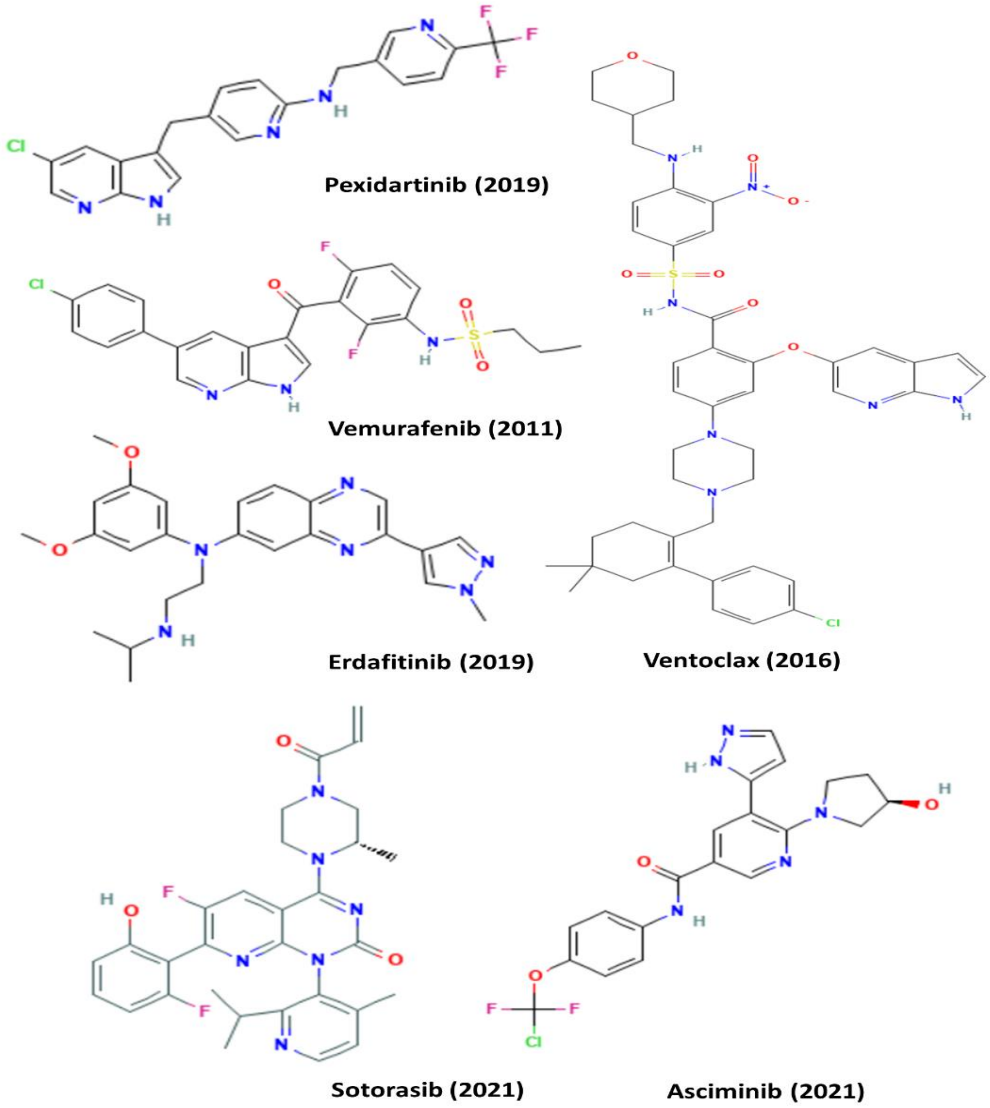

Figure 1.7: Structures of six approved drugs derived from FBDD. These drugs were develop using different FBDD techniques. Remarkably, all of them are used in the treatment of different kinds of cancer. Two of them, Pexidartinib and Vemurafenib were built from the same fragment namely 7-azaindole (Bollag *et al*, 2012; Zhang *et al*, 2013).

Moreover, there are around 30 drug candidates deriving from the FBDD approach which are currently tested in clinical tries against various diseases like cancer, Alzheimer´s disease and type 2 diabetes (Wyatt *et al*, 2008; Artis *et al*, 2009; Whitley *et al*, 2016). FBDD has been adopted as a mainstream technique for drug design by large pharma companies, but it is also used in academia as method to develop chemical lead compounds in a highly reliable way (Kashyap *et al*, 2019; Murray & Rees, 2009).

The core concept of FBDD is the identification of low molecular weight compounds which bind to the protein of interest with a low affinity and are referred to as “fragments”. These fragments follow the “Rule of 3” (RO3) which means that they have a molecular weight below 300 Da, a logP of ≤ 3, H-bond donors ≤ 3 and H-bond acceptors ≤ 3 (Congreve *et al*, 2003). The

fragments which interact with the protein of interest can be identified by several techniques for example surface plasmon resonance (SPR), isothermal calorimetry (ITC), thermal shift assays (TSA) and mass spectrometry (MS). The evaluated fragment hits can be elaborated into larger and more potent compounds while the key interactions are maintained. A typical FBDD pipeline is depicted in Figure 1.8.

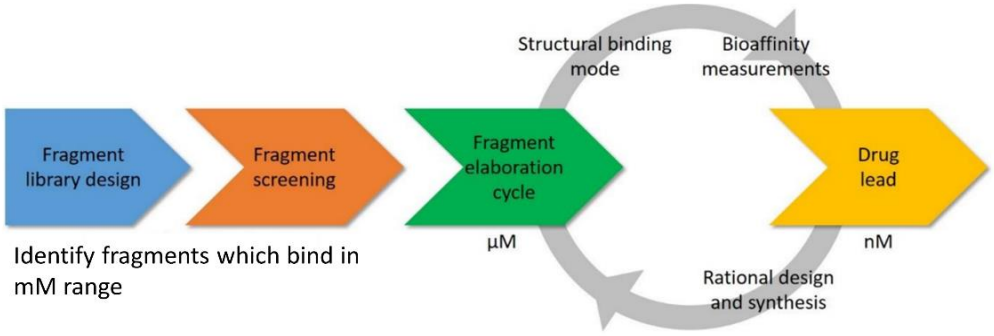

Figure 1.8: Depiction of a FBDD pipeline**.** The first step is the identification of a suitable target, followed by choosing a convenient fragment library. After identification of fragments hits, these are improved via a loop of identifying the exact interaction mode between fragment and protein of interest, bio affinity measurements and improvement via rational drug design. Figure was adapted from (Mitchell, 2018).

1.3.3 Experimental methods for the detection of ligand binding

Several different methos can be applied to detect the interaction between a protein and a fragment. Thereunder, surface plasmon resonance (SPR), isothermal calorimetry (ITC), thermal shift assay (TSA) and mass spectrometry (MS) have been successfully used in fragment-based drug discovery, but these methods only provide little information about the exact binding mode and provides no platform for further rational development of the fragments (Schiavina *et al*, 2022; Ye *et al*, 2022; Sanchez *et al*, 2022; Abbas *et al*, 2011). The two structure-based methods nuclear magnetic resonance (NMR) and X-ray crystallography provide more accurate information about the binding location and the interactions between fragment and protein and also generally deliver fewer false-positive hits compared to the other methods (Napolitano *et al*, 2022; Ciulli *et al*, 2006; Kozakov *et al*, 2015).

1.3.4 Surface plasmon resonance

SPR has become the most commonly used technique in fragment screening campaigns due to the high sensitivity of this method (Lundquist *et al*, 2021). Other great advantages of this method are the relatively low costs compared to other methods and also the low amounts of protein required (approximately 50µg per fragment screening campaign) (Chavanieu & Pugnière, 2016). In order to perform a SPR experiment, the protein of interest is tethered to the surface of a biosensor chip. The fragments are passed over the chip and the attached

protein while a beam of polarized light is directed towards the surface of the biosensor and the change in the refractive index is measured. These changes can be correlated to the combined mass of the protein of interest and the fragment, which can reveal binding events as well as kinetic information. A number of successful SPR-based fragment screening campaigns on different targets have been reported, including HSP70, different target of SARS-CoV-2 and lactate dehydrogenase A (Basso *et al*, 2021; O'Connor *et al*, 2022; Ward *et al*, 2012).

1.3.5 Thermal Shift Assays (TSA)

TSA monitors the changes in the thermostability of a protein of interest. It can be used to find suitable conditions for purification or storage of a protein (Huynh & Partch, 2015). Any protein denatures at a distinct temperature, exposing its hydrophobic core and making it accessible to a sensitive fluorescent dye. Fragments bound the protein of interest are expected to change the thermal stability of the protein upon complex formation which results in a detectable change of the melting point. TSA is a very rapid and easy method for fragment screening, and it does not require large amounts of protein as a suitable protein concentration for a TSA assay is between 0.5 – 2 µM depending on the interactions with the fluorescent dye. Nevertheless, as the interactions between fragments and proteins are expected to be comparatively weak, the thermal shifts will be small. A fragment is considered a hit if the melting temperature is shifted by 1°C or more. TSA was successfully applied to find inhibitors for prolyl-tRNA synthase and mitogen-activated protein kinase 4 (Pang *et al*, 2021; Krishna *et al*, 2013).

1.3.6 Isothermal Titration

ITC is a biophysical method which allows very precisely the determine of changes in temperature occurring when two samples are mixed. These changes can be correlated to the binding profile of a ligand to a receptor. ITC measures the free energy of the binding event ΔG (affinity) and the enthalpy ΔH, which can be used to calculate the entropy ΔS and the reaction stoichiometry (n). Having access to such binding profiles makes ITC to a very powerful method in the detection of protein-ligand interaction and in the optimization of ligands. Particularly the discrimination between the enthalpic and entropic compounds of a binding event makes this method very valuable to identifying fragments that are more enthalpic binders. These fragments are considered to be better starting points for further development steps for potential drugs (Scott *et al*, 2009). However, this method requires relatively high amounts of protein, which, combined with the often low solubility of fragments, means that this method is not suitable for large scale screening. Indeed, it is better suited to confirm potential fragment hits discovered by other approaches or to verify improved binding of follow-up compounds (Ladbury *et al*, 2010). Nevertheless, this method was already used successfully in the development of an inhibitor against acetylcholine-binding protein and is

expected to play a major role in the discovery of new antibiotics (Lamoree & Hubbard, 2018; Edink *et al*, 2011).

1.3.7 Mass spectrometry

Electrospray ionization mass spectrometry (ESI-MS) is an analytical method which consist of the measurement of the mass-to-charge ratio of an ionized molecule to detect its molecular weight. This technique can be applied to detect the binding of a fragment to a protein, as the detected molecular weight will increase upon binding. Moreover, it allows the calculation of the dissociations constant (K_D) and also the stoichiometry (n) (Pedro & Quinn, 2016). As ESI-MS requires only small amounts of protein, is can be considered as fast primary fragment screening technique (Vaaltyn *et al*, 2022). Although ESI-MS is not often used as primary screening technique, there are some success stories for the inhibitor development against Hsp90 (Li *et al*, 2020).

1.3.8 Nuclear magnetic resonance

FBDD owes a lot to NMR, as it this was the first method to deliver successes in a fragment-based approach, also called structure-activity relationship (SAR by NMR) (Shuker *et al*, 1996). NMR is a structural method which can be used to determine a 3D model of a proteins. It can also be used to investigate the interaction between a protein of interest and a ligand (Sugiki *et al*, 2018). This method, NMR spectroscopy, is based on the magnetic properties of the atomic nuclei and can be used to gain knowledge about the surrounding chemical environment. The two main approaches for NMR spectroscopy employed in fragment screening are protein-detected NMR and ligand-detected NMR (Vuckovic *et al*, 2021; Viegas *et al*, 2010). Protein-detected NMR can provide information about the binding affinity in a mM to nM range and deliver details about the binding site between a protein and a fragment. The drawback of this method is the large amount of labelled protein (50-200 mg) required to perform an experiment making it inappropriate for fragment screening campaigns. Ligand-detected NMR can be utilized by different techniques, whereby saturation transfer difference (STD) and water-ligand observed by gradient spectroscopy (WaterLOGSY) are the most common ones (Viegas *et al*, 2011; Dalvit *et al*, 2002). Both methods make use of an irradiation pulse which is applied with the suitable resonance frequency for the biomolecule or the water bulk. From the ^{1}H NMR signal the relaxation properties of the fragments can be calculated, allowing to distinguish between bound and unbound fragments. NMR was already successfully applied in several FBDD campaigns, developing inhibitors against HDM2, HSP90 or PDK1 (Medina *et al*, 2010; Fradera *et al*, 2022; Li *et al*, 2020).

1.3.9 X-ray crystallography

X-ray crystallography is a method which can provide structural information at a very high resolution down to an atomic level (Li, 2020)**.** Crystallography is essential and called the "gold-standard" in fragment-based drug design, as a structure of a complex consisting of the protein of interest and a fragment delivers both the proof of a binding event and also exact information of how the fragment interacts with the protein (Patel *et al*, 2014a). The first step in the employment of this method is the establishment of a suitable crystallization system, as it has to be able to deliver hundreds of crystals which reliable diffract to a high resolution. Preferably, crystals should be grown from low salt conditions with relatively high contents of solvent reagents, as high salt conditions may disturb the (ionic) interaction of the protein with low-affinity binding fragments (Begley *et al*, 2011). Another requirement is that regions of interest in the protein are exposed to the crystals solvent channels to ensure that fragments can diffuse to these areas (Luan & Huynh, 2022). To obtain crystals which contain both the protein of interest and the fragment, two main approaches are commonly used: soaking and co-crystallization. Soaking means preparing a single fragment or pools of fragments, which are added to the mother liquor of preformed crystals of apo-protein. The usage of fragment pools for soaking can speed up to process, but a drawback of this method can be that the different fragments within the pool compete for the same binding site, which will lead to fewer fragment species identified bound to the protein. Therefore, the composition of fragment pools has to be chosen carefully. If crystals are soaked with only a single fragment, the workload is increased but the information about each fragment is more accurate. Exact information about the binding mode of a fragment to a protein enables a more precise downstream development of the fragment into a potential lead compound. Historically, the comparatively low throughput of this method confined it to being used as a second or third level screening method. However, due to the rise of screening possibilities at synchrotrons in combination with the availability of more suitable fragment libraries, it can now also be used as a primary fragment screening technology (Thomas *et al*, 2019). X-ray crystallography has been used in various fragment-based drug design campaigns, for example against several SARS-CoV-2 proteins as well as BACE-1 or Janus kinase 2 (Yamamoto *et al*, 2022; Antonysamy *et al*, 2009; Freidel & Armen, 2021; Wyss *et al*, 2011).

1.3.10 Hit to lead generation

Hit-to-lead generation uses structural information as starting points for rational development of fragments into lead compounds and finally drug candidates. (Murray & Blundell, 2010). While NMR was the technique which was first applied to perform fragment screening and successful hit-to-lead campaigns, nowadays X-ray crystallography is by far the preferred structural method in FBDD (Maveyraud & Mourey, 2020). During optimization the ligand efficiency (LE) metrics are used to determine the relative efficacy of a fragment development step (Hopkins *et al*, 2014). The LE score gives the binding energy of the fragment or follow-up

compound per atom and is calculated by converting the K_D into the Gibbs energy (ΔG) of binding at 300 K and then dividing by the number of heavy (non-hydrogen) atoms (Hopkins *et al*, 2004). The LE score can be understood as a tool to compare the size and the potency of a fragment or follow-up compound. Analysis of successful hit-to-lead campaigns have shown that the LE of the starting fragments was around 0.38 (Hopkins *et al*, 2014). In general, there are three different ways of how fragments can be developed into potential lead compounds: By merging different fragments, by linking different fragments or by growing a single fragment. All of these methods require structural information about the interaction of the fragments and the protein of interest and are therefore a distinct field of FBDD, namely structure-based drug design (SBDD)(Batool *et al*, 2019). In Figure 1.9, two developing methods of fragments are depicted.

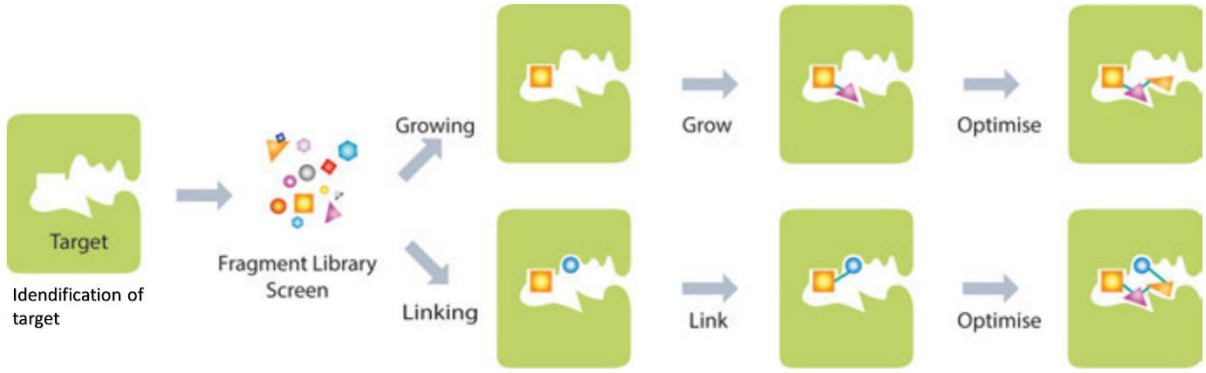

Figure 1.9: Depiction of a FBDD campaign. The first step is the identification of a target of interest. The second step is the identification of interacting fragments. These fragments can now be further grown by structural and medical chemistry, or different fragments can be linked together to develop a follow up compound which binds with high affinity. Figure was adapted from (FitzGerald, 2021).

1.3.11 Fragment Linking

Fragment linking was the first successful approach to develop an inhibitor derived from fragments (Shuker *et al*, 1996). For an efficient joining procedure, two fragments individually bound in close proximity are needed. The link between these two fragments can be rigid or flexible, but it should have a positive influence on the ΔG values of the final follow-up compound (Jencks, 1981). In practice, this method is often challenging, as linkers can restrain the follow-up compound too much. This can result in suboptimal interactions and therefore a loss in binding affinity (Ciulli & Abell, 2007). A fragment linking approach was employed successfully for the development of the drug Venetoclax, a BCL-2 inhibitor used in the treatment of chronic lymphocytic leukemia (Oltersdorf *et al*, 2005).

1.3.12 Fragment growing

Growing describes the development of an initial hit via extension along a defined vector. It has emerged as the most frequently used hit-to-lead strategy (Lamoree & Hubbard, 2017).

This method is based on the stepwise growing of a fragment, targeting a new interaction with each added extension. Structure guided development is able to fulfill special requirements of a potential follow-up compound like adding a hydrogen donor/acceptor or filling a small lipophilic cave with a methyl group. This method was successful employed in the development of Vemurafenib, a selective inhibitor of the B-Raf V600E mutant kinase, which is used in the treatment of late-stage melanoma (Bollag *et al*, 2012).

1.3.13 Fragment merging

Fragment merging describes the process of merging several fragment hits with overlapping regions into a single follow-up compound with higher potency. It strongly relies on structural information of the regions where fragments overlap. Up to this date, no drug emerging from this method has entered the market.

1.3.14 SAR by catalogue

Another fragment optimization method is the so-called structure-activity relationship (SAR) by catalogue. It is one of the most commonly used techniques in SBDD and can be described as substructure or similarity search (Wilson *et al*, 2021). Using the initial hit, vendor catalogues or in house databases are searched for follow-up compounds which could also bind to the protein of interest in a similar manner. This limits this method to existing molecules, however, this also poses the advantage that existing molecules can be rapidly acquired as they do not need to be synthesized. This approach was used to develop inhibitor for the farnesyl pyrophosphatase synthase, which may be used in the treatment of breast and prostate cancer (Park *et al*, 2021).

1.4 Scope of the thesis

The rise of antibiotic resistance in bacteria is one of the global concerns regarding health and wealth. The mis- and overuse of antibiotics in agriculture and during the Covid pandemic leads to an increase of bacterial strains which are resistant to one or more antibiotic substances (Lai *et al*, 2021; O'Neill, 2014). Therefore, the number of effective antibiotics is decreasing, resulting in an urgent need to develop new antibiotics. The identification of new targets, which inhibition can lead to cell death is a difficult task, as the target need to be essential. Moreover, it should not have any homologue in the human system to ensure the specificity towards the bacterial cell (Boyd *et al*, 2021).

The second messenger c-di-AMP was described to serve as a key factor in the regulation of different osmolyte homeostasis pathways and is therefore essential for many pathogenic bacteria (Stülke & Krüger, 2020). Moreover, this second messenger is not produced in the

human system, rendering its synthesizing enzymes as potential target for the development of new antibiotics (Commichau *et al*, 2015). This work focuses on the establishment of a crystallization system of the most abundant diadenylate cyclase CdaA which is suitable for the performance of a crystallographic fragment screen (CFS). Therefore, crystallization experiments employing truncated CdaA constructs originating from the organisms *Bacillus subtilis*, *Enterococcus faecium, Listeria monocytogenes, Staphylococcus aureus* or *Streptococcus pneumoniae* were carried out. After identification of such a system, a fragment screening campaign was performed using the fragment library F2X-Entry screen. Furthermore, a rational drug design approach was applied, using the structure of *Bacillus subtilis* CdaA in complex with AMP as starting point. The fragments and compounds deriving from both approaches was further biochemically characterized to gain insights into their inhibitory effects towards CdaA and to identify suitable starting point for inhibitor design.

2 Material and methods

2.1 Material

2.1.1 Fine chemicals

All fine chemicals and organic components were purchased from the companies AppliChem, Biomol, Bio-Rad, Bld-Pharma, Enamine, Merck, Molport, Roth, or Sigma-Aldrich in the highest available purity grade. Generally, the supplier with the lowest price was chosen.

2.1.2 Devices

Adjustable pipets	Eppendorf
Agarose gel electrophoresis chamber	Bio-Rad
Centrifuge Allegra 21R	Beckman Coulter
Centrifuge Avanti J-20 A	Beckman Coulter
Centrifuge Avanti J-30 I	Beckman Coulter
Centrifuge Avanti JA-20	Beckman Coulter
Fine balance	Satorius
Microfluidizer 110 S	Microfliuds
Mosquito pipet robot	SPT Labtech
NanoDrop	Thermofisher
pH-meter	Beckman Coulter
Real-Time PCR Biometra Detection System CFX 96	Bio-Rad
Rotor JA-20	Beckman Coulter
Rotor JA-30.50 Ti	Beckman Coulter
Rotor JLA 8.100	Beckman Coulter
SDS-PAGE chamber miniVE	Hoefer
Spectrolight 600	Xtal concepts
Table top centrifuge 5417 R	Eppendorf
Thermomixer comfort	Eppendorf
UV/VIS photometer	GE Healthcare
VICTOR nivo multimode microplate Reader	PerkinElmer

2.1.3 Supplemental material

24 well crystallization plates	Hampton Research
96 well crystallization plates	Hampton Research
Adhesive Clear qPCR Seals	Biozyme
Assay Plate 96 well, flat bottom, black polystyrene, NBS	Corning
Crystal Clear tape	Henkel
Multiple well plate, 96-well flat bottom with Lid	Sarstedt
Nylon loops for crystals	Molecular dimensions
Reactions tubes (0.5, 1.5, 2.0 mL)	Eppendorf
Real-time PCR plate 96 well	Bio-Rad
Ultra centrifugal filter units	Milipore
Viewseal Sealer, clear	Greiner

2.1.4 Cell Media

In this work, 2YT and autoinduction media was used for cloning and recombinant protein expression. For 2YT, the components were dissolved in desalted H_2O and autoclaved at 121 °C for 20 minutes. Antibiotics were added as required with a final concentration of 50 µg/mL for kanamycin and 34 µg/mL for chloramphenicol. The components for the autoinduction media were autoclaved separately and mixed directly prior to usage. Agar plates were produced by supplementing 2YT media with 1.5% (w/v) agar prior autoclaving

2YT media

1% (w/v) Trypton

1% (w/v) Yeast extract

1% (w/v) NaCl

Autoinduction medium was prepared by mixing 450 mL ZY-media with 10 mL M-mixture, 10 mL 5052-solution und 100µL Trace elements. Furthermore, ddH_2O was added to a total volume of 500 mL

5000x Trace elements	**50x M-buffer**	**50x 5052-buffer**
50 mM $FeCl_3$	1.25 M K_2HPO_4	25% (w/v) Glycerol
20 mM $CaCl_2$	1.25 M NaH_2PO_4	2.5% (w/v) Glucose
10 mM $MnCl_2$	2.5 M NH_4CL	10% (w/v) α-lactose
10 mM $ZnSO_4$	0.25 M Na_2SO_4	
2 mM $CoCl_2$		
2 mM $NiSO_4$	**ZY-media**	
2 mM Na_2MoO_4	1% (w/v) Tryptone	
2 mM Na_2SeO_3	0.5% (w/v) Yeast extract	
2 mM H_3BO_3		

Minimal medium was used for growth experiments with *B. subtilis*. These experiments were performed by Robert Warnecke (Department of General Microbiology, Göttingen).

100x Trace elements		**5x MSSM Stock**		**100x Iron-citrate**	
2.5 mM	$CaCl_2$	250 mM	Na_2HPO_4	0.5 mM	$FeCl_3$
0.5 mM	$MnCl_2$	130 mM	NaH_2PO_4	3.5 mM	Na_3-citrate
1.2 mM	$ZnCl_2$	20 mM	Na_3-citrate		
0.2 mM	$CuCl_2$	4 mM	$MgSO_4$		
0.25 mM	$CoCl_2$				
0.2 mM	Na_2MoO_4				

For the final MMSM minimal medium, 200 mL auf 5x MSSM stock, 10 mL 100x trace elements, 10 mL 100x iron-citrate, 5g glucose, 10 ml trypothophane (5 mg/mL), 10 ml ammonia solution (20% w/v) and 5 mL KCl (1M) were mixed together and ddH_2O was added to a final volume of 1 L.

2.1.5 Chromatography systems and columns

All chromatographic methods were performed using the Äkta Prime system from GE Healthcare. To load samples on the respective columns, superloops with a volume of 150 mL as well as loops with a volume of 5 mL were used. Utilized columns are listed below.

HisTrap 5 mL Ni-NTA Sepharose	GE Healthcare
Superdex 75 26/60	GE Healthcare

2.1.6 Organisms

The used *E. coli* strains Rosetta II (DE3) and XLI-Blue were part of the collection of the Department for Molecular Structural Biology, Göttingen.

The used *B. subtilis* strains were part of the collection of the Department of General Microbiology, Göttingen.

2.1.7 Plasmids

In the table below, all vectors are listed which were used for recombinant protein expression in this work. The plasmids which were used for cloning of the *L. monocytogenes* and *B. subtilis* constructs used in this work were a kind gift of the Department of General Microbiology, Götingen. Vectors which encoded for the CdaA of *S. pneumoniae*, *S. aureus* and *E. facelis* were purchased as codon optimized constructs from BioCat. The only expression vector which was used in this work was pet28a, which has an N-terminal 6x His-tag. Between the inevitable amino acids and the protein sequence, a PreScission protease site was cloned. The sequences of the primers used are listed in table 2.1

Name	Cloning method	Oligonucleotide
Pet28a_LmCdaA (102-255)	Restriction site cloning	TG1, TG2
Pet28a_SaCdaA (110-260)	Restriction site cloning	TG3, TG4
Pet28a_EfCdaA (121-270)	Restriction site cloning	TG5, TG6
Pet28a_SpCdaA (82-256)	Restriction site cloning	TG7, TG8
Pet28a_BsCdaA (103-254)	Restriction site cloning	TG9, TG10
Pet28a_BsCdaA (98-260)	Restriction site cloning	TG11, TG12
Pet28a_BsCdaA (94-273)	Restriction site cloning	TG13, TG14

2.1.8 Size Standards

Size standards that were used during the agarose-gel electrophoresis and SDS-PAGE are listed below

GeneRuler 1kb DNA ladder	Fermentas
PageRuler Prestained Protein Ladder #26617	Fermentas

2.1.9 DNA Oligos

Table 2.1: DNA oligonucleotides used for the cloning of the plasmids mentioned in table 2.1. All oligonucleotides were purchased from Sigma-Aldrich

Name	Sequence (5´-3´)
TG1	CTAGCTAGCCTGGAAGTGCTGTTTCAGGGTCCGTCAAGAATTGAGCGTGAACAGCATC
TG2	CGGGATCCTTATGTGACTAGTTCTTTAAGAAGAATT TTATGTAACTC
TG3	CTAGCTAGCCTGGAAGTGCTGTTTCAGGGTCCGAGCAAAGATGAAGAAAAACTGATTCAGAGTG
TG4	CGGGATCCTCATTCAATCAGTTCCAGATTCAGC
TG5	CTAGCTAGCCTGGAAGTGCTGTTTCAGGGTCCGAGCGAACAGCAGGAAGATGAAAAAATG
TG6	CGGGATCCTTAAATCAGTTCACGACGCAGAATGGCC
TG7	CTAGCTAGCCTGGAAGTGCTGTTTCAGGGTCCGGCCGAAGAACAGATGATTCGTGC
TG8	CGGGATCCTTAACCAAACCAATGTTCTGCCAGCAG
TG9	CTAGCTAGCCTGGAAGTGCTGTTTCAGGGTCCGACGATTGAGGCCATTACAAAAGC
TG10	GCGGGATCCTTAAAACTCGGCTTCAAGCATTTCTTTCAGC
TG11	CTAGCTAGCCTGGAAGTGCTGTTTCAGGGTCCGACGATTGAGGCCATTACAAAAGC
TG12	GCGGGATCCTTATCTGTGAAGGTCGCCGTTCTTTGC
TG13	CTAGCTAGCCTGGAAGTGCTGTTTCAGGGTCCGGAAGCGCAGCAGAAAACGATTGAG
TG14	CGGAATTCTTACTTAAACTCGGCTTCAAGCATTTCTTTCAGC
T7 forward	TAATACGACTACTATAGGG
T7 reverse	GCTAGTTATTGCTCAGCGG

2.1.10 Crystallization Screens

The following screens were used during initial screening for crystallization conditions of different CdaA constructs.

Ammonium sulfate suite	Qiagen
JBScreen Classic (1,2,4,5)	Jena Bioscience
JBScreen Classic (6-8, 10)	Jena Bioscience
JBScreen Nuc-Pro HTS	Jena Bioscience
JCSG+ Suite	Jena Bioscience
Midas	Molecular Dimensions
Midas diluted	Molecular Dimensions
Morpheus	Molecular Dimensions
Natrix	Hampton Research
Pact++	Molecular Dimensions
PGA	Molecular Dimensions
ProPlex	Molecular Dimensions

2.1.11 Computer programs and databases

Acedrg v13.1	(Long *et al*, 2017)
CCP4 suite 8.0	(Winn *et al*, 2011)
Coot 0.9.4.1	(Emsley *et al*, 2010)
Chainsaw 6.0.2	(Stein, 2008)
Dimple 11.9.1	(Wojdyr *et al*, 2013)
ESPript	(Robert & Gouet, 2014a)
FragMAXapp	(Lima *et al*, 2021)
LSQMAN 5.4	(Kleywegt, 1996)
Mosflm 7.4.0	(Battye *et al*, 2011)
Pandda v0.2	(Pearce *et al*, 2017a, 2017b)
Phaser	(McCoy *et al*, 2007)

Phenix 1.19.2-4158	(Liebschner *et al*, 2019)
GraphdPad Prism 6	Dotmatics
Protparam	(Wilkins *et al*)
Pymol 2.5.3	Schrödinger LLC
SeeSar 12.1	BioSolveIt GmbH
XDS (10.1.22)	(Kabsch, 2010)

2.2 Molecular biological methods

2.2.1 Polymerase chain reaction

The Polymerase chain reaction (PCR) is a powerful tool to amplify the desired regions of a specific DNA sequence. A general PCR setup using Phusion Polymerase consists of 1 ng/µL template DNA, 10 pmol forward and reverse oligonucleotides, 0.01 U/µL of Phusion polymerase, 1x HF-buffer, 0.04 mM dNTP mixture and 3%5 µL DMSO added up to 50 µL with ddH_2O. A typical PCR programm is shown below

cycles	**temperature [°C]**	**step**	**time [s]**
1x	98	initial denaturation	30
25x	98	denaturing	10
	52-60	annealing of oligonucleotides	30
	72	elongation	15s/kb
1x	72	final elongation	300

The resulting product was purified using the PCR clean-up Kit from Machery&Nagel and analysed by agarose gel electrophoresis.

2.2.2 Agarose Gel electrophoresis

Agarose gel electrophoresis is a commonly used method to separate oligonucleotides according to their size. In this work, this method was used to separate the DNA fragments resulting from PCR and enzymatic digestion. To cast a gel, TAE buffer was supplied with 1% agarose and boiled in a microwave. After the solution were cooled down, GelRed staining

solution were added in a ratio of 1:10000 according to the manufacturer's instructions. The resulting gel was transferred in the appropriate running chamber. The samples containing the oligonucleotides were mixed with DNA loading dye in a ratio of 1:10 and loaded onto separate lanes. The agarose geld was run with a voltage of 12 V/cm. Recipes for the TAE buffer and 10x DNA loading dye are listed below

10x DNA loading dye	TAE buffer
0.25 % (v/v) bromophenol blue	40 mM Tris pH 7.5
0.25 % (v/v) xylene glycol	20 mM acetic acid
30 % (v/v) glycerol	1 mM EDTA

2.2.3 DNA sequencing

All sequencing of DNA was performed using the service of the company SeqLab, Miyrosynth, Göttingen. The sequence of oligonucleotides T7 forward and T7 reverse which were used for sequencing PCR are listed in table 2.1.

2.2.4 Determination of DNA concentration

The concentration of DNA in solution was determined by absorption measurements at 260 nm using the Nanodrop. The purity was determined by calculating the ratio of the absorption at 260 nm and 280nm. For samples comprised of pure DNA, this ratio should be around 1.8. If the DNA samples exhibit lover values, this indicates contamination with protein.

2.2.5 Enzymatic DNA digest

In order to perform a ligation of DNA, both the PCR product and the vector DNA need to be digested to create suitable endings of the DNA. Therefore, the oligonucleotides were transferred into a suitable buffer and incubated with the respective restriction enzymes at 37 °C for 1hr. Afterwards, the restrictions enzymes were inactivated by incubation the sample at 80 °C for 10 minutes. Finally, the resulting samples were mixed with 10x DNA loading dye and applied to an agarose gel.

2.2.6 Molecular cloning

The gene of interest was amplified by PCR with the appropriate oligonucleotides. The resulting DNA as well as the destination vector were digested with restriction enzymes to create matching ends at the 3´ and 5´ ends of the PCR product and cleaved vector DNA. Furthermore, the vector was incubated with shrimp alkaline phosphatase (SAP) at 37°C for 1hr. Afterwards,

the SAP was inactivated by incubation the sample at 65 °C for 15 minutes. The ligations set up typically consisted of 50 ng vector DNA with a 5x molar excess of insert DNA. Furthermore, 1 µL T4-ligase and 1 µL of the supplemented 10x reaction buffer were added. DdH_2O was added to the sample until a volume of 10 µL was reached. The sample were incubated at 4 °C for 72hrs. The entire reaction volume was transformed into *E. coli* XLI-Blue cells and plated on agar plates which contained the appropriate antibiotic.

2.2.7 Transformation of chemical competent *E. coli* cells

To transform circular plasmid DNA into *E. coli* cells, 100 ng of plasmid DNA were mixed with 50 µL chemical competent cells. The sample were incubated on ice for 30 minutes, followed by a heatshock at 42 °C for 1 min. The Eppendorf tube was placed back on ice for 2 minutes. Afterwards, 500 µL 2YTmedia were added and the cells were incubated at 37°C and 400rpm for 45 minutes. Finally, the reaction vessel was centrifuged at 3000x g for 1 minute, the supernatant discarded, and the cells dissolved in 50 µL fresh 2YT media. The cell suspension was then plated on 2YT agar plates supplied with the appropriate antibiotic.

2.2.8 Preparation of plasmid DNA

To amplify plasmid DNA for further cloning steps, sequencing or recombinant protein expression, the plasmid of interest was transformed (2.2.7) into *E. coli* XLI-Blue cells and plated onto 2YT agar plates supplied with the appropriate antibiotic. A single colony was used to inoculate 5 mL of 2YT media with the appropriate antibiotic and incubated at 37°C overnight. Plasmid preparation was performed with the Plasmid Prep Kit from Machery&Nagel according to the manufacturer's instructions. The resulting DNA samples were stored at -20 °C for further usage.

2.2.9 Recombinant protein expression

For the recombinant protein expression, the plasmid which encodes the desired protein was transformed into the *E. coli* strain Rosetta II (DE3) (2.2.7). This plasmid is constructed in a way in which the coding gene is under control of an inducible promotor. All the plasmids used in this work contain the lac-promotor, which can be induced be either lactose or the lactose derivate isopropyl-β-d-thiogalactopyranosid (IPTG). For expression, 50 mL of 2YT media were supplemented with the appropriate antibiotic and inoculated with several colonies of *E. coli* from an agar plate which carries the desired plasmid. The culture was incubated at 37 °C, 210 rpm overnight. The expression media (2.1.4) were inoculated with 2 mL from the preculture, incubated at 37°C and 210 rpm for 2 hrs. Afterwards, the temperature was reduced to 16 °C and the cells were further incubated for 72 hrs. As the media already contains lactose, it will

automatically induce the expression of the target protein by itself. This method was adapted from (Studier, 2005).

2.2.10 Cell harvest and lysis

In order to purify the target protein, the expression cultures have to be harvested and lysed. Therefore, the expression cultures were harvested by centrifugation at 4 °C, 4800x g for 45 minutes. The supernatant was discarded, and the cell pellet resuspended in ddH_2O. This sample was again centrifugated at 4800x g, 4 °C for 30 minutes. The obtained cell pellet was flash frozen in liquid nitrogen and stored at -20 °C for further usage.

Lysis of the cells were performed by dissolving the pellet in the appropriate lysis buffer with an additional 10 mM $MgCl_2$, a scoop tip of lysozyme and 0.1 U/mL DNase I. After one hour of incubation, the cell suspension was applied seven times to a Microfluidizer 110S, in which the cells pass a chamber at high pressure which leads to the collision of the cell membrane. The resulting cell lysate was clarified by centrifugation at 30000x g at 4 °C for 45 minutes. Subsequently, the supernatant was filtered by hand using a cut-off of 0.45 µM. Finally, the cell lysate was loaded into a super loop and applied to a chromatography purifications protocol.

2.2.11 Chromatographic methods

To separate the target protein from the cell lysate and purify it to a high homogeneity, several chromatographic steps was performed. All the columns used were stored in 20% (v/v) ethanol, washed with 1 column volume (CV) ddH_2O and equilibrate in the appropriate buffer prior to usage. After usage, the columns were washed with 1 CV of ddH_2O and 1 CV 20% (v/v) ethanol before they were stored.

2.2.11.1 Histidine affinity chromatography

All of the protein constructs contained a 6x histidine tag. Therefore, the first protein purification step performed was an immobilized metal chelating affinity chromatography (IMAC) step using a Ni-NTA Sepharose column. The lysis-, the wash-, and the high salt-buffer contained additional 20 mM imidazole to reduce the unspecific binding of proteins to the column. The elution buffer contained 500 mM imidazole und was applied over a gradient of 120 mL to elute the target protein. The buffer composition in this step was 50 mM Tris/HCl pH 7.5, 500 mM NaCl.

2.2.11.2 Size exclusion chromatography

Size exclusion chromatography is a method to separate molecules according to their size using a porous material. Smaller molecules will enter more pores and therefore migrate slower than larger molecules. Moreover, this method also enables a buffer exchange to store the target protein in a suitable buffer.

2.2.12 Concentrating protein solutions

Protein solutions were concentrated by transferring them into the upper chamber of a Millipore concentrator (Merck) with a vertical membrane which has pores of defined size. By centrifugation, proteins with a size larger than the indicated cut-off remains in the upper chamber, while smaller molecules, water und ions can pass the membrane. The concentration process was continued until the desired protein concentration was reached.

2.2.13 Determination of protein concentrations

Two different methods were used to determine the protein concentration, the Bradford assay, and UV-absorption measurements.

Bradford measurements was performed to determine the protein concentration of the pool after the first purification step, the affinity chromatography. This method is based on the dye Coomassie Blue-G250, which interacts with arginine or aromatic sidechains and thereby undergoes a shift in the absorption maximum from 470 nm to 595 nm when bound to protein. The difference in absorption is directly proportional to the protein concentration. This method was adopted from (Ernst & Zor, 2010).

UV absorption was measured at wavelengths 260 and 280 nm using a Nanodrop. The absorbance was used in combination with the molecular weight of the target protein and its molar extinction coefficient to calculate the protein concentration. Furthermore, the ratio of the absorbance at 260/280 nm gives a hint about remaining nucleotide impurifications, with a ratio between 0.52 and 0.65 considered to be pure protein.

2.2.14 SDS-Polyacrylamide gel electrophoresis

SDS-PAGE was used to analyse the composition of a protein sample by separating the single proteins according to their molecular weight. In this work, only separating gels with a concentration of 15 % acrylamide were used. The gels were prepared by filling the pouring chamber to about 80 % with separating gel solution. To ensure a straight upper edge of the gel, isopropanol was added. After polymerization, the isopropanol was removed and the remaining space was filled with stacking gel, followed by insertion of a 15-pronged comb. The

gels were stored for further usage at 4 °C. Below, the composition of the stacking and the separating gel is listed.

SDS-PAGE separating gel	**SDS-PAGE stacking gel**	
15 % (v/v)	5 % (v/v)	acrylamide
0.4 % (v/v)	0.13 % (v/v)	bis-acrylamide
0.375 M pH 8.80	0.125 M pH 6.8	Tris/HCl
0.1 % (w/v)	0.1 % (w/v)	SDS
0.1 % (v/v)	0.1 % (v/v)	TEMED
0.05 % (w/v)	0.05 % (w/v)	APS

Prior to SDS-PAGE electrophoresis, the samples were mixed with Laemmli buffer and applied to the gel. Electrophoresis was run for about 70 minutes at 400 V and 35 mA. Afterwards, the gel was stained using staining solution. This method was adapted from (Laemmli, 1970).

SDS-PAGE running buffer		**2x Laemmli sample buffer**	
25 mM	Tris/HCl pH 8.3	65.2 mM	Tris/HCl pH 6.8
192 mM	Glycine	0.1 % (w/v)	SDS
0.1 % (w/v)	SDS	55 % (v/v)	Glycerol
		0.1 % (w/v)	Bromophenol blue
		5 % (v/v)	β-Mercaptoethanol

2.2.15 Proteolytic digestion with PreScission Protease

To remove the 6x histidine tag and the dispensable amino acids, of the multiple-cloning site all constructs were cloned with a PreScission protease recognition site located N-terminally between the histidine tag and the protein of interest. Therefore, PreScission protease was added to the protein solution in a 1:100 (w/w) ratio. In order to remove divalent cations, 10 mM EDTA were also added. The protein pool was incubated at 4 °C overnight.

2.2.16 *In Vivo* growth assays

The respective cell strains were cultivated in rich medium overnight and diluted with MSSM minimal medium (MM) in the morning. The cultures were cultivated at 37°C to an OD_{600} of 0.4. A 96-well plate was prepared with 50µL 3xMSSM, 0-100 µL of the inhibitor stock solution

or 1x PBS. 50 µL of the preculture was used to inoculate each well to an OD_{600} of 0.1. The growth rate of the cultures was monitored by measuring the OD_{600} in a microplate reader. The strain *E. coli* Bl21(DE3) and the *B. subtilis* strains 168, GP989 and GP1361 were used (Mehne *et al*, 2013). The *B. subtilis* strain 168 is the wild type-like strain, while GP989 is missing the genes *cdaS* and *cdaA*. GP1361 is missing the genes *cdaS* and *disA*.

2.3 Biophysical Methods

2.3.1 Determination of the cyclase activity

For the determination of the cyclase activity of a protein, two different assays were carried out. The first one is based on the detection of the final product of the reaction, c-di-AMP, via its interaction with coralyne (Zhou *et al*, 2014). The second one is based on the detection of the second product of the reaction, namely pyrophosphate. Therefore, the Malachite Green assay kit from Sigma Aldrich was used.

2.3.1.1 Coralyne assay

This assay is based on the interaction of the product of CdaA, c-di-AMP, with coralyne. The fluorescence of the molecule coralyne is quenched in the presence of halide ions, but coralyne can be protected by c-di-AMP. The standard reaction setup contained 40 mM Tris/HCl pH 7.4, 100 mM NaCl, 10 mM of $MnCl_2$, 100 µM ATP and 10 µM CdaA. For carrying out ion specificity experiments, $MnCl_2$ was substituted by the corresponding metal ion. Inhibition experiments were carried out with a concentration of 100 µM potential inhibitor and in presence of 20 % DMSO. The experiment was started by adding ATP to the reaction setup. Afterwards, the sample was incubated at 37°C for 15 minutes. The reaction was stopped by boiling the Eppendorf tube at 95 °C for 5 minutes. 250 mM KBr and 10 mM coralyne were added and incubated at RT for 15 minutes. Subsequently, the samples were transferred to a 96 well, flat bottom plate (2.1.3) and their fluorescence measured using a platereader. The sample was irradiated with an excitation wavelength of 420nm (Excitation filter: 420/10 BP HH35000917) and the emission was measured at a wavelength of 475 nm (Emission filter: 380/30 nm). Measurements were always performed as triplicates. This method was adapted from (Zhou *et al*, 2014; Heidemann *et al*, 2019).

2.3.1.2 Malachite Green assay

For this assay the Malachite Green assay kit from Sigma Aldrich was used. This assay can be used to quantify the amount of free orthophosphate. As one of the products of CdaA is pyrophosphate, the pyrophosphate can be broken down into orthophosphate, enabling its

detection by complex formation with Malachite Green and molybdate. Figure 2.1 depicts the reaction setup.

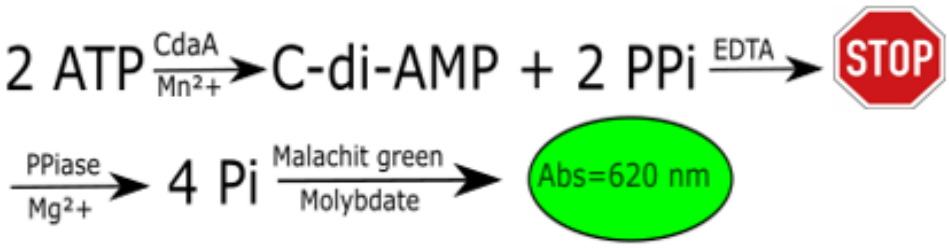

Figure 2.1: Schematic representation of the Malachite green assay. The first step is formation of the products c-di-AMP and pyrophosphate catalyzed by CdaA. This reaction is stopped by the addition of EDTA. Afterwards, $MgCl_2$ and pyrophosphatase are added, to hydrolyze the pyrophosphate into orthophosphate. By mixing the sample with the malachite green reagent, a complex consisting of orthophosphate, malachite Green and molybdate is formed. The absorbance of this complex can be measured at 620 nm.

The reaction mixture contained 40 mM Tris/HCl pH 7.4, 100 mM NaCl, 10 mM of $MnCl_2$, 100 µM ATP and 10 µM CdaA with a total volume of 100 µL. Inhibition experiments were carried out with a concentration of 100 µM potential inhibitor and in presence of 20 % DMSO. The reaction was started by addition of ATP and the sample was incubated at 37 °C for 15 minutes. Afterwards, the reaction was stopped by adding EDTA to a final concentration of 20 mM. This step is necessary as pyrophosphatase exhibits hydrolyzing activity against ATP, leading to additional orthophosphate in the sample which does not derive from pyrophosphate. Subsequently, 4.8 mU/µL PP_iase and 20 mM $MgCl_2$ were added to a final volume of 200 µL. The reaction setup was incubated at 37 °C for 15 minutes. According to the manufacturer's instructions, 80 µL reaction sample were mixed with 20 µL Malachite Green working solution in a clear plate and incubated for 30 minutes in the dark. Finally, the absorbance at 620 nm was measured using a platereader. Measurements were always performed as triplicates. This method was adapted from (Sherwood *et al*, 2013).

2.3.2 Dynamic Light Scattering

Dynamic Light Scattering (DLS) is a method used to characterize the size distribution of particles in a solution, for example proteins. Therefore, a laser beam is passed through a polarizer and then channeled on the sample, which scatters the light based on the properties of the present particles. The scattering angle of the light can be detected and gives insight on the composition of the sample. This method was adapted from (Carpenter, 1977).

Here, DLS was used for the quality control of the purified protein in terms of its homogeneity. Experiments were performed using a SpectroLightTM 600 (Xtal concepts) and a protein concentration of 1 mg/mL.

2.3.3 Binding studies of CdaA using Isothermal titration

To determine the binding affinity of *Bs*CdaA to different substrates, ITC was employed. The protein storage stock was diluted to a concentration of 1.2 mM and centrifuged to remove any insolubles at 21000x g for 30 minutes. The substrate was dissolved in buffer from the size exclusion chromatography step (10 mM Tris/HCl pH 7.5, 200 mM NaCl) to a final concentration of 12 mM if possible and the pH was readjusted to 7.5. To the buffers, 5 mM $MgCl_2$ was added. Before use, the protein and the substrate were preheated and degassed using the vacuum unit of the ITC to 25°C for 10 minutes. The protein was loaded into the cell while the substrate was kept in the syringe. The ITC which was used for these experiments was the PEAQ-ITC from Malvern. The reference power was set to 15, while the stir speed was 740rpm. The injections had a spacing of 150 seconds, with a duration of 4 seconds. In total, 20 injections were performed. Data analysis was done with the PEAQ-ITC analysis software.

2.3.4 Thermal shift assay

To gain information if the identified fragments/inhibitors change the stability of the protein, a thermal shift assay was performed. This assay is based on an interaction of the hydrophilic core of the protein a fluorescent dye. The protein of interest with a final concentration of 1 µM was mixed with 10x fold molar excess of the potential inhibitor, which was stored in DMSO. Therefore, the final DMSO concentration was 5 %. Furthermore, the fluorescent dye Sypro Orange, with a final concentration 1:10000 (v/v) was used. The sample was transferred into a 96-well plate and centrifuged (10 min, 1500x g). For the measurement of the temperature profile, the temperature was stepwise risen from 20 to 95 °C in increment steps. For data analysis, *MaxStAF* was used.

2.4 Crystallographic methods

2.4.1 High throughput screening

Initial screening for crystallization conditions were performed using a Mosquito pipet robot (SPT Labtech) in combination with MRX96-3 well plates. The protein concentration ranged between 4 to 6 mg/mL. Metal ions were added in 10x molar excess, while ATP was added in 20x molar excess. When ions or ATP was added prior pipetting, the sample was incubated on ice for 2 hrs. In a general setup, two drops were pipetted in ratios of 1:1 (0.25 µL protein and 0.25 µL reservoir) and 1:0.5 (0.25 µL protein and 0.125 µL reservoir). As negative control, reservoir was mixed with sample buffer in a ratio of 1:1 (0.25 µL to 0.25 µL) The volume of the reservoir was 39.775 µL. After pipetting, the plates were sealed and stored at 20°C. The plates were regularly checked for crystal growth using a binocular microscope.

2.4.2 Optimization of Crystals

Upon identification of initial conditions where crystal could be observed, the concentration of the single components and the protein concentration were varied in a finescreen process. DMSO was added to some crystallization conditions, to increase the solubility of fragments in later soaking experiments. Finescreening was performed using 24-well sitting drop vapor diffusion plates with a reservoir volume of 500 µL, a drop volume between 1.5 and 4 µL and varying protein:reservoir ratios. After pipetting, the plates were sealed and regularly checked for crystal growth using a binocular microscope.

2.4.3 Soaking of Crystals

Soaking experiments were carried out with crystals of *L. monocytogenes* CdaA (Heidemann *et al*., 2019) or *B. subtilis* CdaA crystals. A fragment screening campaign was carried out in collaboration with Jan Wollenhaupt (Helmholtz Zentrum Berlin, Berlin). The F2X-Entry screen was provided by Helmholtz Zentrum Berlin, a fragment screen consisting of 96 fragments, dried on a 3-lens 96 well MRC low profile crystallization plate, which covers a large chemical space and has been reported to have a high hit rate (Wollenhaupt *et al*., 2020). The reservoir of each well was filled with 40 µL crystallization buffer and the desired volume to reach a concentration of 100 mM was pipetted on the dried fragment. Afterwards, 4-5 crystals were transferred to each drop. To reduce the evaporation during the transferring process, a novel evaporation-protecting device was used (Barthel *et al*., 2021). The plate was sealed afterwards and incubated at 20 °C overnight.

Soaking of follow up compounds or single fragments were performed using a 24-well sitting drop vapor diffusion plate. Therefore, the compound was dissolved in DMSO with a final concentration of 100 mM. Subsequently, 1 µL of the fragment was pipetted in the well of the plate and dried at RT for 2 days to evaporate the DMSO. Afterwards, 500 µL crystallization buffer was transferred into the reservoir and 1 µL was used to dissolve the fragment. 3-4 crystals were transferred into the drop and the plate was sealed and stored at 20 °C overnight.

2.4.4 Crystal harvesting and cryoprotection

Single crystals were fished with a nylon loop. If the crystallization condition was not already preventing the solvent to form ice, the crystal was shortly soaked in crystallization buffer supplement with a cryoprotectant reagent (glycerol, PEG400 or PEG3350). Afterwards, the crystals were flash frozen in liquid nitrogen and stored therein.

2.4.5 X-ray diffraction experiments

Nylon loops with crystals were mounted on a goniometer head, cooled via a nitrogen gas stream to a temperature of 100 °K and exposed to X-rays. Datasets were collected in-house using a MicroMax 007 rotating anode (Rigaku), at the beamlines P13 and P14 DESY Hamburg, at the beamline 14.1 BESSY II, Berlin or at the beamline ID-23.1 ESRF, Grenoble. The established collection strategy was the collection of 360°, incremented in 0.1 ° steps. To reduce the total collection time of datasets deriving from crystals soaked with compounds from the F2X-entry screen, only 270° were collected with an oscillation range of 0.15°. If data were collected inhouse, an oscillation range between 0.5 and 1° was applied, depending on the predications of *Mosflm*. All datasets were checked for radiation damage using *XDsstat.* In none of the collected datasets radiation damage were observed.

2.4.6 Data processing and refinement

The obtained datasets from the fragment screening campaign were automatically processed and refined using *FragMAXapp*, using the apo structure of *Bs*CdaA as search model (Lima *et al*., 2021). All other datasets obtained were processed using the *XDS* program package (Kabsch, 2014). The molecular replacement was performed using CdaA as search model, if a structure was available in the PDB, or a CdaA model was modified using *Chainsaw* (Stein, 2008). For the replacement, *Dimple* or *Phaser* were used (Wojdr *et al*., 2013; Liebschner *et al*., 2019). Refinement was performed using *Phenix.refine* and manual model adjustment in *Coot*. (McCoy *et al*., 2007; Emsley*et al*., 2010). Also, a refinement pipeline established by Piotr Neumann (Department for Structural biology, Göttingen) was employed. Cif files were generated using *Acedrg* (Long *et al*., 2017). R.m.s.d. values were calculated using LSQMAN (Kleywegt, 1996).

2.4.7 Identification of fragments

To identify fragments bound to the protein *Bs*CdaA, the refined datasets deriving from *FragMAX*app were used. Quick search was performed using *Dimple* or the search for unmodeled Blobs implemented in *Coot*. For identification of weakly bound fragments, *Pandda* was employed (Pearce *et al*., 2017a; Pearce *et al*., 2017b). To further develop the fragments and identify follow-up compounds which might be used as lead compounds, *SeeSar* was employed. This program has a graphical user interface and uses mainly the HYDE scoring system to evaluate the binding of a compound (Schneider *et al*., 2013). The program was used with the database *Molport*.

3 Results

3.1 Cloning, purification, and activity tests of CdaAs from different organism

For the crystallization of a protein the design of the respective construct, which should be used for further experiments and crystallization trials, is important, as it influences the chances of successful crystallization. Therefore, the first steps of this thesis were the identification and design of constructs which were expected to crystallize in a suitable system for a fragment screening campaign. To assess if the purified CdaAs are functional, a coralyne assay to demonstrate the synthesis of c-di-AMP was carried out.

3.1.1 Cloning of suitable constructs for crystallization

The crystals obtained so far were all obtained in high salt concentrations, reducing the chances of fragment binding. One goal of this work was to establish a low-salt crystallization system for the protein CdaA in its APO state for a fragment soaking campaign and co-crystallization of inhibitory compounds. Therefore, the CdaA of the organisms *Listeria monocytogenes*, *Staphylococcus aureus*, *Streptococcus pneumonia*, *Bacillus subtilis* and *Enterococcus faecium* were cloned into the expression vector pET-28a which encodes for a N-terminal 6x histidine tag followed by a thrombin cleavage site and the multiple cloning site. The first decision was to clone an additional PreScission protease cleavage site between the multiple cloning site and the protein of interest to minimize the amount of undesired amino acids linked to the proteins N-terminus. A careful selection of the length of a crystallization construct is necessary as flexible regions tend to reduce the chance of crystallization and decrease the diffraction quality (Tang *et al*, 2021). Moreover, sites which are potential important interaction sites for fragments or ligands should not be covered by unstructured N- or C-terminal regions. This was previously observed in a crystal structure of CdaA from *L.monocytogenes* in the APO state, where parts of the N-terminal region occupy the active site of the protein (PDB-ID:6HVM). Therefore, if accessible structural data (*S.aureus*, *L.monocytogenes* and *B.subtilis*) or alternatively models predicted by *Alphafold2* (*E.faecium* and *S.pneumoniae*) were employed to identify potential minimal constructs without N-or C-terminal flexible regions (PDB-ID:6YGW, 6HVM, 6HUW). This approach is illustrated below on the example of *Bs*CdaA.

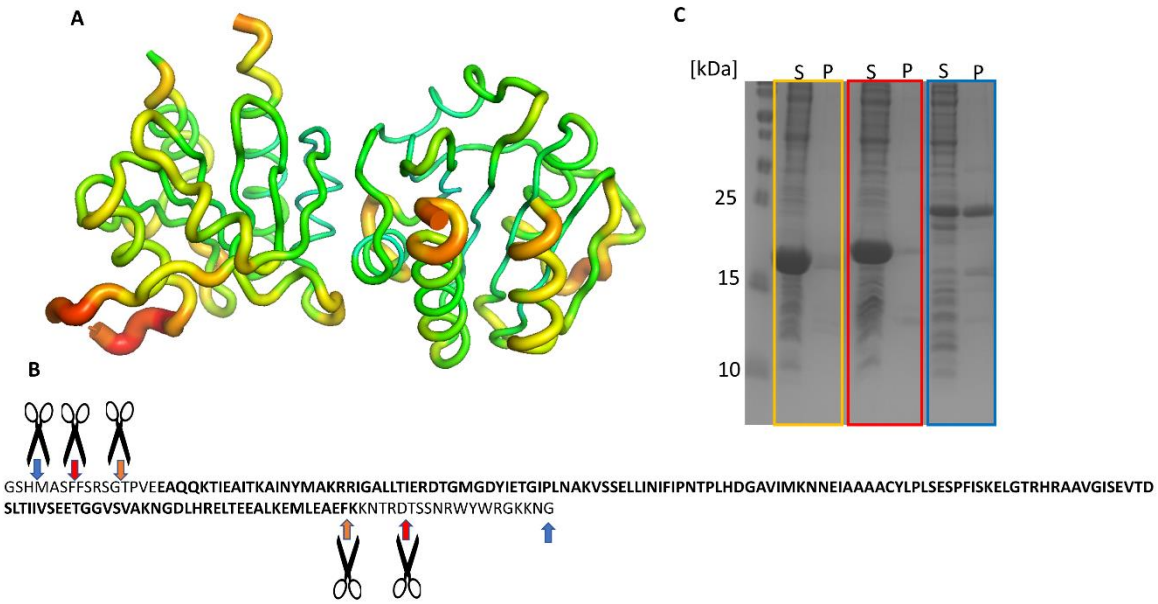

Figure 3.1: CdaA construction to identify a minimal construct. **A** Crystal structure of *B.subtilis* CdaA (PDB-ID:6HUW) in the putty representation where thicker and red colored regions correspond to high B-factors while thin and green colored regions correspond to low B-factors. **B** represents the sequence of the construct whose structure is represented in **A.** The bold letters of the amino acid sequence represent the residues which were visible in the electron density. The pairs of scissors with the identical colored arrows represent the three different truncations which were carried out. **C** shows a 15% SDS-PAGE stained with Coomassie Blue. Different constructs expressed in *E. coli* were lysed, centrifuged and the supernatant (S) and pellet (P) were applied to the SDS-PAGE. The color of the arrows below the scissors correspond to the color of the rectangles around the gel.

The structure of the *B.subtilis* CdaA (PDB-ID: 6HUW) in the putty B-factor representation reveals that the C-and the N-terminal regions have elevated B-factors (Fig. 3.1A). Interestingly, several N- and C-terminal residues show no electron density (Fig. 3.1B) which might lead to raised B-factors of the ends and to the relatively low resolution of 2.8 Å. Therefore, this structural data was used to carry out a series of truncations, depicted by the scissors in Figure 3.1 B. The truncations were cloned as described in M&M and verified by sequencing. The resulting constructs were used to perform expression and solubility tests. All three constructs could be expressed in *E.coli*, but the largest construct was not completely soluble (Fig. 3.1C, indicated in blue) in contrast to the other two shorter ones. Consequently, the smallest construct was chosen as it was expected to be the least flexible and seems most promising for crystallization experiments.

3.1.2 Expression and purification of CdaA from different organisms

In the previous section the rationale behind the truncation of CdaA to get a construct which is more susceptible for crystallization was explained. The next step was the establishment of an expression and purification protocol which delivers high amounts of pure and homogenous protein for the performance of crystallization trials. To prevent lower yields due to rare codons, all pET-28a-PP-CdaA constructs were transformed into the *E.coli* strain Rosetta (DE3). The proteins were overexpressed using autoinduction media. After harvesting, the cells were resuspended in a buffer containing 50 mM Tris/HCl pH 7.5, 500 mM NaCl and 20 mM imidazole and applied to a microfluidizer. The resulting cell lysates were ultracentrifuged, and the supernatants were applied to an Ni-NTA column. During this step, a even higher salt wash step was included to remove potential adenine-derivates bound to CdaA. The eluates were incubated with PreScission protease to remove the N-terminal additional amino acids. Moreover, EDTA was added to a final concentration of 10 mM in order to remove remaining divalent cations which can bind to CdaA and cause heterogeneity of the sample. Afterwards, the protein samples were applied to a Superdex S200 size exclusion column in a buffer containing 10 mM Tris/HCl pH 7.5 and 200 mM $MgCl_2$. Coupled to the SEC column was a GSH-Sepharose column to remove the added GST-tagged PreScission protease and uncleaved construct. Figure 3.2 A shows samples of the purified CdaA from *L.monocytogenes*, *S.aureus*, *S.pneumoniae*, *B.subtilis* and *E.faecium*. Besides the CdaA constructs, no additional bands are visible, indicating a high purity of all samples. To verify the homogeneity of the protein samples, they were subjected to a DLS experiment. Figure 3.2 B shows exemplary the DLS results of *B.subtilis* CdaA, which exhibits a high homogeneity as just one band is visible. Taken together, the purified CdaA constructs originating from five different organism could be purified to a high purity and homogeneity suitable for further crystallization trials and activity assays.

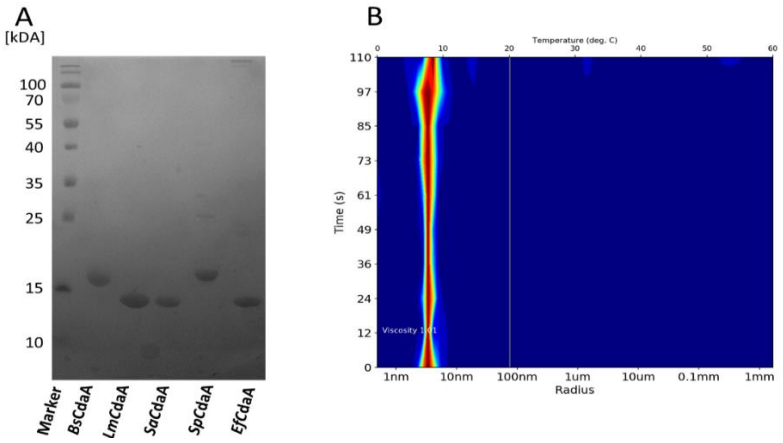

Figure 3.2: Quality control of purified CdaA constructs. **A** Coomassie-Blue stained 17.5% SDS-PAGE with samples of the purified CdaAs from different organisms. All samples display only minor impurities. **B** Result of the DLS experiment performed with *Bs*CdaA depicted as a radius distribution plot. This experiment indicates a high homogeneity of the purified protein.

3.1.3 Coralyne activity test with CdaA

To prove the enzymatic functionality of the purified proteins the coralyne activity assay was applied. In this assay, the coralyne fluorophore is protected by the c-di-AMP formed in the cyclase reaction, leading to an increase of the measured fluorescence intensity as the reaction proceeds as it cannot be quenched by halogens (Zhou *et al*., 2014). Moreover, the metal ion specificity should be determined as previous studies revealed differences between CdaAs from different organism (Heidemann *et al*., 2019; Tosi *et al*., 2019). All purified CdaAs show activity in the presence of Mn^{2+} but not in the absence of ions, proving that they are all functional diadenylate cyclases as shown in Figure 3.3. Contradictorily with the results of Gründling and co-workers, no cyclase activity could be determined for the CdaA of *S.aureus* in presence of magnesium (Tosi *et al*., 2019). In fact, the CdaAs from *S.aureus, B.subtilis* and *E.faecium* show only activity in the presence of manganese, while CdaA from *L.monocytogenes* also shows slight activity in the presence of cobalt fitting to previous findings (Heidemann *et al*., 2019). Surprisingly, CdaA from *S.pneumoniae* exhibits not only cyclase activity in the presence of manganese, but also with magnesium and cobalt. This finding is quite interesting and should be further investigated and will be discussed below as the sequences of all tested CdaAs are quite similar as shown in Figure S 1. The sequence similarity of all used constructs is between 82 and 95 %, while the sequence identity is between 65 and 79 %.

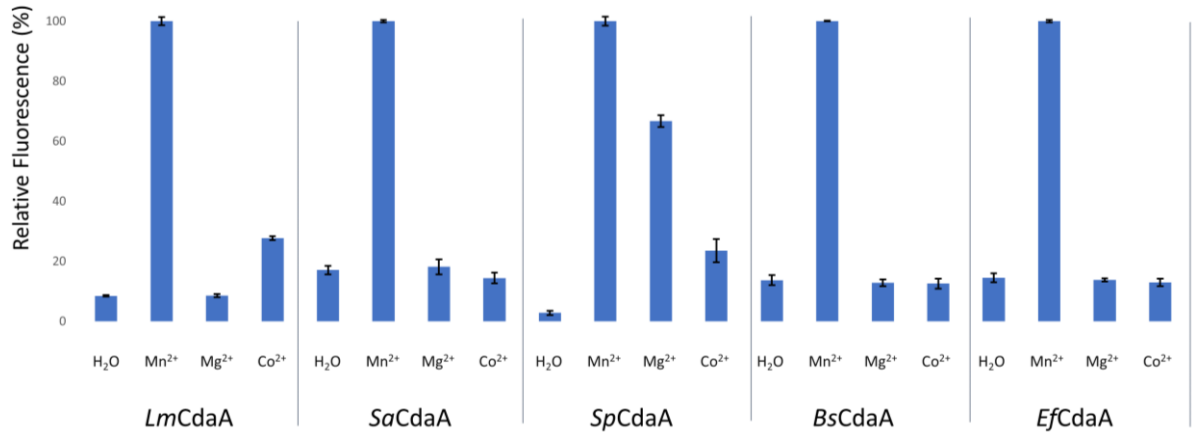

Figure 3.3: Cyclase activity of CdaA from different organisms in presence of different metal ions. The y-axis displays the measured fluorescence of the coralyne as percentage value. The data were normalized by setting the fluorescence in the presence of manganese ions to 100%. The y-axis displays the measured fluorescence as percentage value. The experiment was performed in triplicates, shown are mean values, the error bars correspond to standard deviation. All purified CdaAs exhibit activity in the presence of manganese ions while their activity in presence of magnesium- or cobalt-ions differs.

3.2 Crystallization experiments using truncated CdaA from different organisms

In the previous section, different metal ion specificity of CdaA depending on the source organism were detected. Therefore, these CdaAs were applied to crystallization trials in presence of the best suitable divalent metal ion and the substrate ATP. Moreover, also crystallization trials were performed to find a suitable crystallization system to produce crystals which fit the requirements of a fragment screening campaign.

3.2.1 Crystallization of *Streptococcus pneumoniae* CdaA in complex with c-di-AMP and magnesium

The finding that CdaA from *Streptococcus pneumonia* is the only CdaA examined in this work to exhibit cyclase activity in the presence of magnesium was highly surprising. Therefore, crystallization trials were carried out to gather structural information how the *Sp*CdaA interacts with magnesium. Before crystallization, *Sp*CdaA was mixed with a 10x molar excess of $MgCl_2$ and a 20x molar excess of pH adjusted ATP. The protein sample was incubated at 37°C for 30 minutes to allow for formation of active dimers and synthesis of c-di-AMP. Afterwards, pre-crystallization trials were carried out and identify a concentration of 4 mg/ml as most suitable concentration. A set of twelve initial crystallization screens was carried out and incubated at 20°C. First crystals could be observed after 48 hours in various conditions containing salts at concentrations between 0.5 and 4 M and pH values between 6 and 8.5. The final crystals chosen were grown in a condition consisting of 100 mM Tris/HCl and 4 M NaCl (Fig. 3.5).

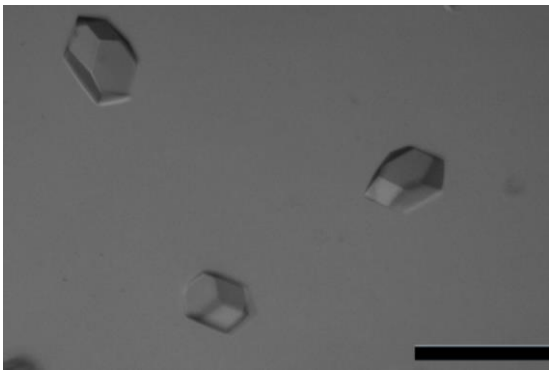

Figure 3.4: Crystals of SpCdaA in presence of c-di-AMP and magnesium. The crystals grew in a condition consisting of 100 mM Tris/HCl pH 8.0 and 4 M NaCl after 48 hrs incubation time at 20°C. The tetragonal shaped crystals grow to a size of 100 µm in length and 50 µm in diameter. The black reference bar corresponds to a length of 200 µm.

The crystals were cryoprotected with reservoir solution with additional 0.5 M NaCl and flash cooled in liquid nitrogen. The crystals were measured at the ID-23.1 beamline of the ESRF, Grenoble. Processing of the collected dataset revealed that *Sp*CdaA crystallized in the tetragonal space group $P4_12_12_1$ and diffracted up to 2.53 Å with satisfying statistics, shown in the supplemental table S.3. The phase problem was solved by means of molecular

replacement using *Phaser* utilizing the structure of *L.monocytogenes* CdaA (PDB-ID:6HVL) modified with *Chainsaw* to the last common atom as initial model. The structure was refined by iterative cycles of *Phenix* and manual model building in *Coot*. The final model exhibited R_{work}/R_{free} values of 25.5 and 29.1 %, respectively. The complete data statistics are shown in table S.3. The final model of *Sp*CdaA consists of a back-to-back homodimer in the asymmetric unit (Fig.S.4) Additional density was observed in the active site of one monomer, revealing the presence of an AMP molecule and a magnesium ion. Interestingly, the *Sp*CdaA monomer with bound AMP forms an active dimer in a post catalytic state with its corresponding symmetry mate. The two active sites face each other and sandwich the product of CdaA, namely c-di-AMP. The model of the homodimer builds up from two monomers in different asymmetric units is shown in Figure 3.6. The polder map contoured at a sigma level of 5 clearly indicates the presence of the product c-di-AMP (Fig. 3.6A).

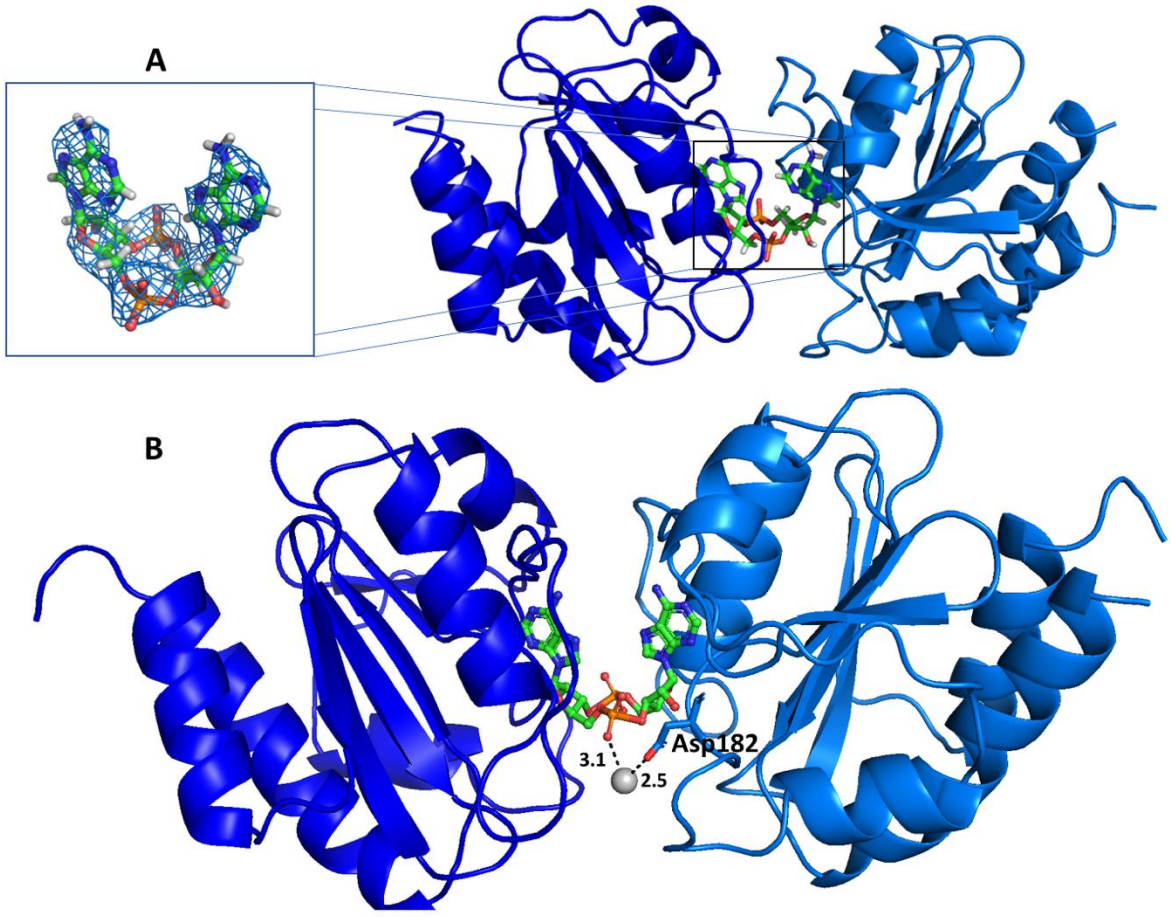

Figure 3.5: Structure of *Sp*CdaA in complex with c-di-AMP. **A** Representation of the post catalytic dimer of *Sp*CdaA as *cartoon*, which sandwiches the product c-di-AMP presented as *stick and balls*. The blue rectangle presents the polder omit map of the c-di-AMP, contoured at a sigma level of 4. **B** The black dashed lines mark the polar interactions of the magnesium ion, shown as grey sphere, with the oxygen of the phosphate moiety of the c-di-AMP molecule and the carboxylate group of Asp182. The numbers besides the dashed lines indicate distances and are in Å.

A careful inspection of the arrangement of the homodimer revealed that the catalytically necessary metal ion magnesium is only coordinated by an oxygen of the phosphate moiety of the product c-di-AMP and the carboxylate group of the Asp-182 (Fig. 3.6 B). Unfortunately, this provides no explanation why *Sp*CdaA is the only CdaA examined here, which exhibits activity in the presence of magnesium (Fig. 3.3). Investigation of the interaction between c-di-AMP and *Sp*CdaA revealed the formation of hydrogens bonds between the product and the amino acids Asp-171, Gly-152, Arg-182 and Leu-168 which are nearly identical to the interaction network of *Lm*CdaA with c-di-AMP (PDB-ID:6HVM). This finding shows that the interaction pattern of CdaA with c-di-AMP is strongly conserved.

3.2.2 Crystallization of *Enterococcus faecium* CdaA in complex with c-di-AMP and manganese

As the crystallization of *Sp*CdaA in complex with c-di-AMP and magnesium gave no further insight into the rationale of the metal ion specificity of CdaA additional experiments were carried out to crystallize the *Ef*CdaA in complex with c-di-AMP and manganese. *Ef*CdaA was chosen as it is active exclusively in the presence of manganese, in contrast to *Sp*CdaA or *Lm*CdaA which are also active in presence of cobalt (*Lm*CdaA) or cobalt and magnesium (*Sp*CdaA). Before crystallization, *Ef*CdaA was incubated with a 10x molar access of $MnCl_2$ and a 20x molar excess of pH adjusted ATP at 37°C for 30 minutes. Through pre-crystallization screening, a protein concentration of 5 mg/mL was identified as the most suitable for an initial screen. A set of fourteen different crystallization screens was carried out and stored at 20°C. First crystals were observed after four months in a condition consisting of 100 mM Tris/HCl pH 8.0, 100 mM KCl and 30% PEG400 (Fig. 3.7).

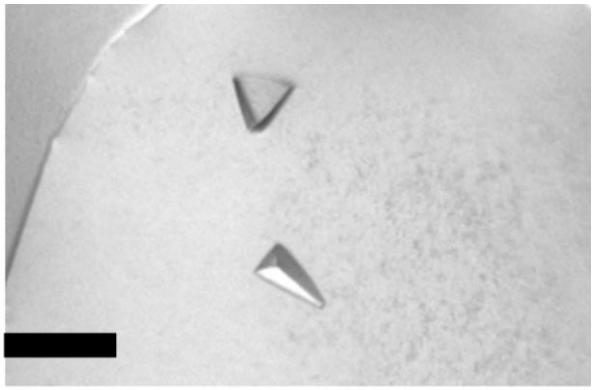

Figure 3.6: Crystals of *Ef*CdaA in presence of ATP and $MnCl_2$. The black bar corresponds to a length of 100 µm. These crystals grew to a size of approximately 80 µM in lengths and were observed in a condition consisting of 100 mM Tris/HCl pH 8.0, 100 mM KCl and 30% PEG400 and appeared after four-month incubation time at 20°C.

The crystals were fished directly from the crystallization well, as it contained 30% PEG400 which is enough to serve as cryoprotectant and flash cooled and stored in liquid nitrogen. Afterwards, the crystals were measured at the P13 PETRA III, Hamburg. Processing with *XDS* revealed that *Ef*CdaA supplemented with ATP and manganese crystallized in the monoclinic

space group P2 and diffracted up to 2.1 Å resolution with satisfying statistics as shown in the supplemental table S.3. The phase problem was solved using *Phaser* in combination with the structure of *L. monocytogenes* CdaA (PDB-ID:6HVL) modified with *Chainsaw* to the last common atom and truncated to the last common atom. The structure was refined by iterative cycles of *Phenix* and manual model building in *Coot*. Also, a script using *Phenix* written by P.Neumann was employed to improve the R values. The final model exhibited R_{work}/R_{free} values of 22.52 and 26.32 %. The complete data are shown in table S.3. The final model of *Ef*CdaA contains a total of 10 CdaA monomers in the asymmetric unit (Fig. S.3). These 10 monomers formed in total 5 active dimers. The active sites of each of the monomers face the active site of another CdaA, sandwiching a molecule c-di-AMP, Moreover, there is additional electron density in the active site, most likely for the catalytically necessary manganese ion (Fig. 3.3). Each of the active monomers is also involved in the formation of a back-to-back dimer.

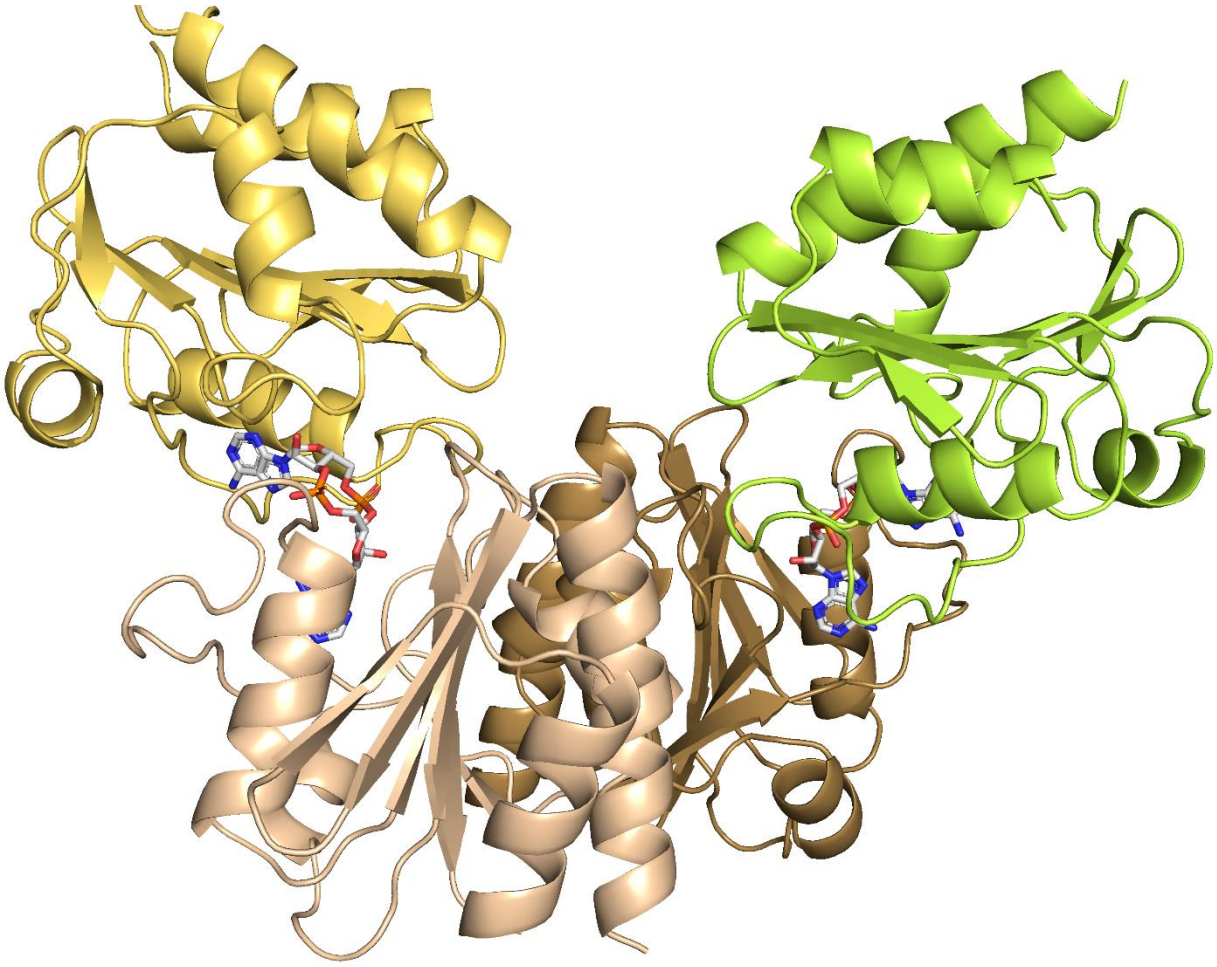

Figure 3.7: Structure of *Ef*CdaA in complex with c-di-AMP. All CdaA structures are represented as *cartoon*. The inactive back-to-back dimer is colored as wheat and sand, while the molecules forming an active dimer with the inactive one is colored yellow and lime. C-di-AMP is presented as *sticks* and is sandwiched between two CdaA molecules.

Interestingly, this is the first structure of CdaA where both monomers of the inactive back-to-back dimer are involved in the formation of the active dimer. In previous structures, like *Lm*CdaA in complex with c-di-AMP (PDB-ID: 6HVL), or *Sp*CdaA in complex with c-di-AMP just one protomer of the inactive back-to-back dimer was engaged in the formation of an active center. Here, every protomer is involved in the formation of an inactive back-to-back dimer but also in the formation of a catalytically active dimer, demonstrating that both protomers of the inactive dimer can be enzymatically active. Comparison with the structure of *Lm*CdaA with c-di-AMP reveals only minor differences (PDB-ID:6HVL). The largest difference can be found in the conformation of the Tyr224, which is required for the cyclase activity of CdaA as is it proposed to be essential for the substrate binding (Heidemann *et al*., 2019). While in the post catalytic *Lm*CdaA structure (PDB-ID:6VHL) the tyrosine is flipped out of the active site, here it is flipped back, able to build π-π interactions with the adenine moiety of the c-di-AMP (Fig. 3.8 B). This indicates that the here observed crystal structure represents a later stage of the catalytic cycle as the *Lm*CdaA structure.

Analysis of the interaction pattern of the manganese ion revealed that it is coordinated by an oxygen atom of the phosphate moiety of the c-di-AMP, the carboxylic group of Asp208 and the imidazole ring nitrogen of His207. This interaction pattern is the same as previously described for *Lm*CdaA and gives no additional insights into the metal ion specificity (Heidemann *et al*., 2019). The interaction of the product c-di-AMP with the enzyme *Ef*CdaA is stabilized, besides the previously described π-π interaction, by the formation of hydrogen bonds between the product and the residues Thr239, Gly207, Asp208 and Leu225. A nearly identical interaction pattern was previously observed for *Lm*CdaA and *Sp*CdaA, emphasizing the importance and conservation of these interactions. Moreover, these interactions could be considered as possible anchor points for an inhibitory compound, as they are highly conserved between different organisms (Fig. S.1).

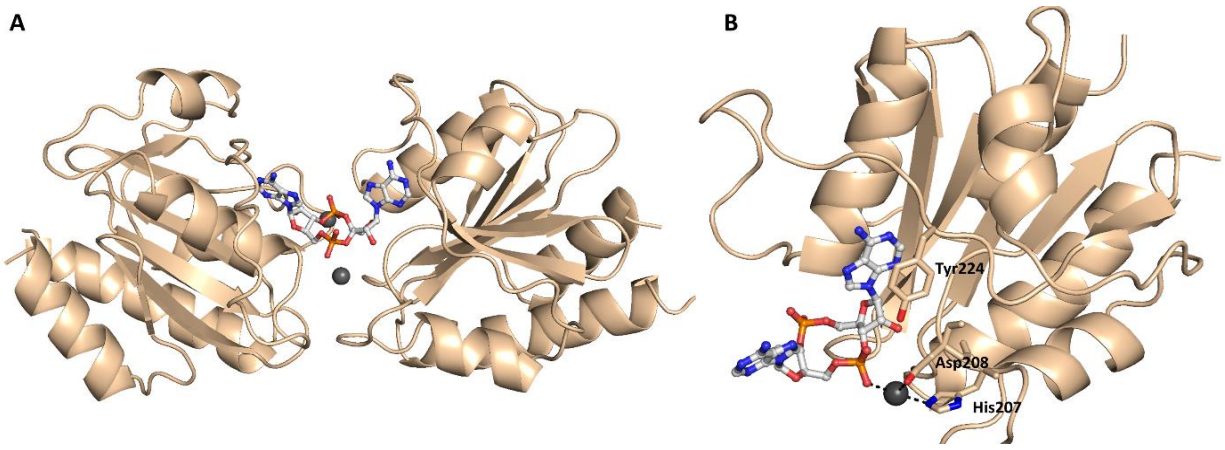

Figure 3.8: Presentation of *Ef*CdaA in complex with c-di-AMP and manganese **A** One of the five *Ef*CdaA post catalytic dimers from the asymmetric unit as *cartoon*, sandwiching the product c-di-AMP represented as *sticks.* **B** One protomer of the active dimer in complex with c-di-AMP and manganese. The black dashed lines indicate the polar interactions of the manganese ion, shown as dark grey sphere, with the oxygen of the c-di-AMP molecule and the amino acids Asp208 and His207. Furthermore, Tyr224 is flipped back and stacks with the adenine moiety of c-di-AMP.

3.2.3 Crystallization of *Enterococcus faecium* CdaA in its APO-state

One of the goals of this project was the crystallization of the protein CdaA in a low-salt condition to fulfill parts of the requirements for the performance of a fragment screening campaign. To this end, an N- and C-terminal truncated construct of CdaA from *Enterococcus faecium* (*Ef*CdaA) was isolated in the APO-state to a high degree of purity and homogeneity (Fig. 3.2). In a pre-crystallization screen, a concentration of 5.5 mg/ml was shown to be suitable for crystallization. In the initial screen campaign *Ef*CdaA was subjected to 14 different crystallization screens and were afterwards stored at 20°C. First crystals were observed after five to six months in a condition consisting of 100 mM Tris/HCl pH 8.5, 5 mM $MgCl_2$ and 30% PEG400. A picture of one of these crystals is displayed in Figure 3.9.

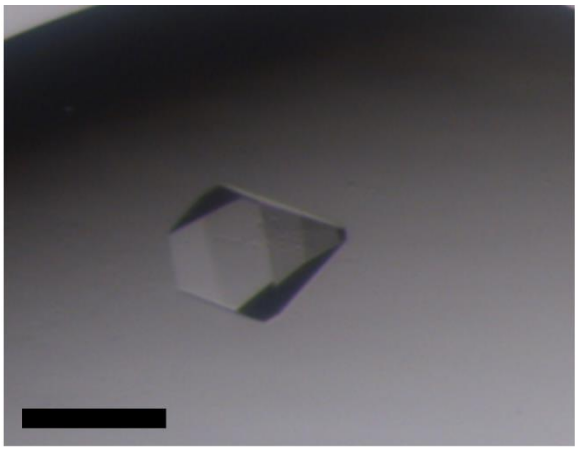

Figure 3.9: Crystal of *Ef*CdaA in the APO state. The black bar corresponds to a length of 300 µm. The first crystals of *Ef*CdaA were observed in a condition consisting of 100 mM Tris/HCl pH 8.5, 5 mM $MgCl_2$ and 30% PEG400 after five-to-six-month incubation time at 20°C.

The crystals were fished directly from the crystallization well, as it contained 30% PEG400 which is enough to cryoprotect the crystals. Consequently, they were flash cooled and stored in liquid nitrogen. Afterwards, the crystals were measured at the P13 PETRA III, Hamburg. Processing with XDS revealed that *Ef*CdaA crystallized in the hexagonal space group $P6_322$ and diffracted up to 2.45 Å with satisfying statistics, which are displayed in table S. 3. The phase problem was solved using *Phaser* in combination with the structure of *Ef*CdaA, which was previously determined as described in section 3.1.6. The structure was refined by iterative cycles of *Phenix* and manual model building in *Coot*. Also, a script using *Phenix* written by P. Neumann was employed to reduce the R values. The final model exhibited R_{work}/R_{free} values of 22.0 and 27.2 %. The complete crystallographic data are shown in the supplemental table S.3.

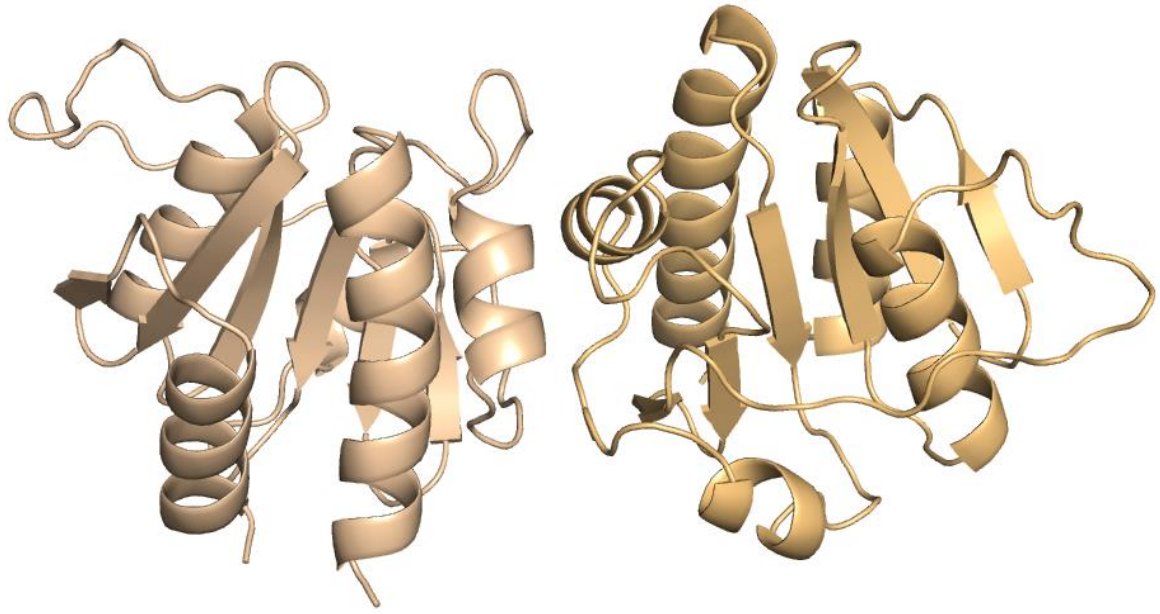

Figure 3.10: Structure of *Ef*CdaA in its APO state. The structure exhibits the typical core composition for DAC domain proteins, consisting of a slightly twisted core made up of seven β-strands surrounded by five α-helices. Both protomers which form a back-to-back dimer are represented as *cartoon*.

Analysis of the asymmetric unit show the presence of two *Ef*CdaA molecules. These two protomers build a back-to-back dimer (Fig. 3.10), which was previously observed for other CdaA in their APO state (Heidemann *et al*., 2019; Tosi *et al*., 2019). Superpositioning of the *Ef*CdaA structure with published CdaA structures in their respective APO state also revealed high structural similarity, as the respective root mean square deviation (r.m.s.d.) values were 1.01, 0.68, 0.65, 0.64 Å (PDB-ID: 6YGW, 6HVM 6HUW and 7L8N). Moreover, analysis of the back-to-back dimer with the *PDEePISA* program reveals an interaction interface of 753 $Å^2$ between the two protomers which represents just 9.6% of the solvent accessible surface. This interface exhibits in total 10 hydrogen bonds and 2 salt bridges with a ΔG of 9.4 kcal/mol indicating a strong protein-protein interaction. Moreover, the calculated CSS score, which indicates the probability for a crystallographic artefact, for the back-to-back interaction is 1, suggesting that this dimer is not a crystallographic artefact.

Nevertheless, even if the protein crystallized in a low-salt condition and the active sites as well as large parts of the surface seem accessible from the solvent channels, this crystallization system it is not very suitable for a fragment screening campaign. The time period which is required for the crystallization is too long and also the diffraction of the crystals were too weak to be suitable for a campaign. Furthermore, these crystals could not be reproduced.

3.2.4 Crystallization of *Bacillus subtilis* CdaA in its APO-state

The crystals of *Ef*CdaA in the APO state do not fulfill the requirements for a fragment screening campaign and no APO crystals for the CdaA from the human pathogens *Staphylococcus aureus, Streptococcus pneumonia* or *Listeria monocytogenes* could be observed. Therefore, an N- and C-terminal truncated CdaA construct from the non-pathogenic organism *Bacillus subtilis* (*Bs*CdaA) was also used as the sequence similarity of the DAC domains of these organisms is very high (65-79%). The respective construct was purified and applied to a pre-crystallization test. A concentration of 4 mg/mL was identified to be the most suitable for initial crystallization screens. Therefore, *Bs*CdaA was applied to 14 different crystallization screens which were consequently stored at 20°C. After two days, crystals could be observed in several conditions, consisting of variable buffer systems with different pH values, different precipitants, and varying salts. One common additive was $MgCl_2$. Crystals, which were found in a condition consisting of 100 mM HEPES pH 8.0, 200 mM $MgCl_2$ and 30% PEG40 grew up to a size of 200 µm. These crystals were chosen for further structural investigations as their crystallization condition does not require further cryoprotectant. The fished crystals were used to collect a dataset at a MicroMax007 anode. Processing with *XDS* revealed that *Bs*CdaA crystallized in the monoclinic space group C2 and diffracted up to 1.71 Å with satisfying statistics, which are displayed in table S.3.

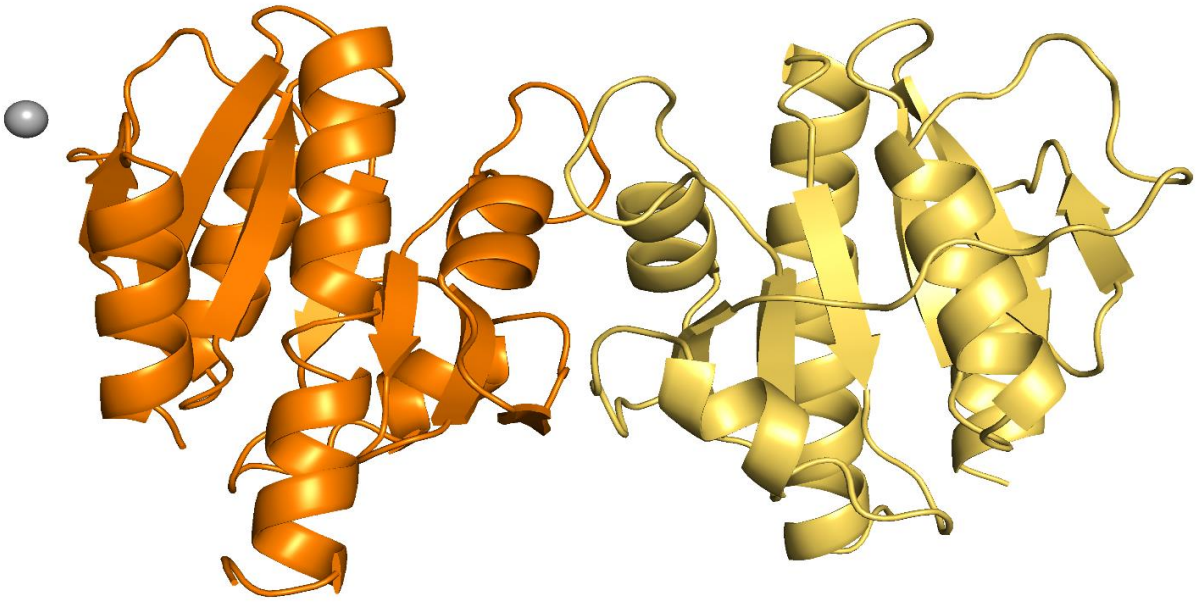

Figure 3.11: Structure of *Bs*CdaA in its APO state. Analysis of the structural composition revealed that the protein exhibits the typical DAC protein composition consisting of a slightly twisted core made up of seven β-strands surrounded by five α-helices. Both protomers which form a back-to-back dimer are represented as *cartoon*. The magnesium ion which was identified in the electron density is depicted as grey *sphere*.

The phase problem was solved using *Phaser* in combination with the structure of *B.subtilis* CdaA deposited in the protein data bank (PDB-ID:6HUW). The structure was refined by iterative cycles of *Phenix* and manual model building in *Coot*. The final model exhibited

R_{work}/R_{free} values of 16.97 and 20.64 %. Further statistics are displayed in table S.3. The asymmetric unit consists of two protomers of *Bs*CdaA (Fig. 3.11). Each monomer exhibits the typical form of CdaA, a slightly twisted core made up of seven β-strands surrounded by five α-helices. The protomers in the asymmetric unit form an inactive back-to-back dimer which was already observed for CdaA in the APO state from different organisms (PDB-ID: 6HUW, 6HVM, 6YGW and 7L8N). Additional, one magnesium ion could be identified in the electron density, likely deriving from the crystallization conditions. Superposition of the deposited *Bs*CdaA APO (PDB-ID:6HUW) structure with the structure obtained in this work using the program *LSQMAN* also showed that there are only small structural differences as the r.m.s.d. value is 0.39 Å for the Cα-atoms. Analysis of the interaction between the two *Bs*CdaA protomers showed that the interaction area is less than 10 % of the surface of the protein, leaving a large part of the protein solvent-exposed (761.4 vs 794.2 $Å^2$). Moreover, the calculated CSS score for the back-to-back interaction is 0.57, indicating that this dimer could be a crystallographic artefact due to the crystal packing. Further analysis of the crystal packing revealed that the active site is accessible from solvent channels, hence, the packing is suitable for a fragment screening campaign.

It can be concluded that *Bs*CdaA fulfills parts of the prerequisites for a fragment screening campaign as the protein crystallizes relatively fast in a low-salt condition which needs no further cryoprotectant. Moreover, the crystal packing likely allows the soaking with fragments, and the crystals diffract up to 1.71 Å resolution at a relatively weak in-house anode.

3.3 Crystallographic fragment screen using *Bs*CdaA

CdaA was previously rendered as potential target for the development of new antibiotics. Therefore, a fragment screen campaign should be performed, utilizing beforehand discovered crystallization conditions for *Bs*CdaA. In a first step, the crystallization system should be optimized to fit the requirements of a fragment screening campaign. Next, this campaign should be performed, using the FX2-Entry fragment screen, a screen developed for the purpose of identification of suitable starting point for inhibitor design. Afterwards, the influence on the activity and thermostability of the fragments towards *Bs*CdaA should be determined.

3.3.1 Adapting the *Bs*CdaA crystals to meet the prerequisites for a fragment screening campaign

In order to perform a crystallographic fragment screening campaign, several prerequisites have to be fulfilled. The Helmholtz Zentrum Berlin (HZB), which is specialized in the execution of these screens, formulated in total 3 prerequisites which need to be fulfilled. 1) Reliable and reproducible crystal conditions to produce more than 200 crystals with a size of at least 50 µM in each dimension to enable faster transferring and fishing. 2) Soaking and cryo-conditions

should be optimized. In the best case, the crystallization condition does not need further cryoprotective additive as the experiment becomes less cumbersome. Moreover, the crystals should ideally tolerate between 5-10% of DMSO during the soaking process to rise the chance that hydrophobic fragments can be soaked into the crystal. 3) Proof of principle by soaking of a known ligand. Before the high efforts of a fragment screening campaign are undertaken, a known ligand should be soaked into the crystal and furthermore the binding should be proven by solving the structure by X-ray crystallography. This approach demonstrates the permeability of the solvent channels (Wollenhaupt *et al*., 2021).

The first step to address the prerequisites was to optimize the crystallization conditions for *Bs*CdaA in its APO state with respect to crystal size and reproducibility. Optimization trials were carried out using a 96-well crystallization plate in combination with the mosquito pipette robot to enable an upscaling in order to produce at least 200 crystals for the fragment screening campaign. The original crystallization condition was already sufficient to cryoprotect the crystals as it contains 30 % PEG400. Therefore, the pH value, the salt concentration and the protein concentration were varied to identify the most suitable crystallization conditions. A crystallization condition using a concentration of 6 mg/mL *Bs*CdaA in combination with 30 % PEG400, 100 mM HEPES pH 7.5 and 100 mM $MgCl_2$ was able to reliably reproduce crystals with a size of around 200x100x50 µM. Crystals of this size are suitable to enable an easy transferring and fishing process.

Furthermore, DMSO was added in different concentrations to the crystallization conditions (5, 10, 15, 20, 25%). The size of the crystals increased slightly with rising DMSO concentration. The largest crystals could be observed at a DMSO concentration of 20% with a size up to 500x 100x50 µM (Fig. 3.12 B). Remarkably, if 25% DMSO are used in the crystallization condition, the drop forms a skin which needs to be removed prior transferring or fishing of the crystals, increasing the total workload for a fragment screen. Five crystals were fished per DMSO concentration and their diffraction properties were tested at the beamline 14.1 BESSY, Berlin. The resulting datasets were equally processed using *XDS* in combination with a script written by P. Neumann. Independently of the DMSO concentration the crystals diffract between 1.4 and 1.5 Å resolution (Fig. 3.12A). Therefore, it was decided to use a DMSO concentration of 20% as this condition yielded the largest crystals and no skin formation was observed.

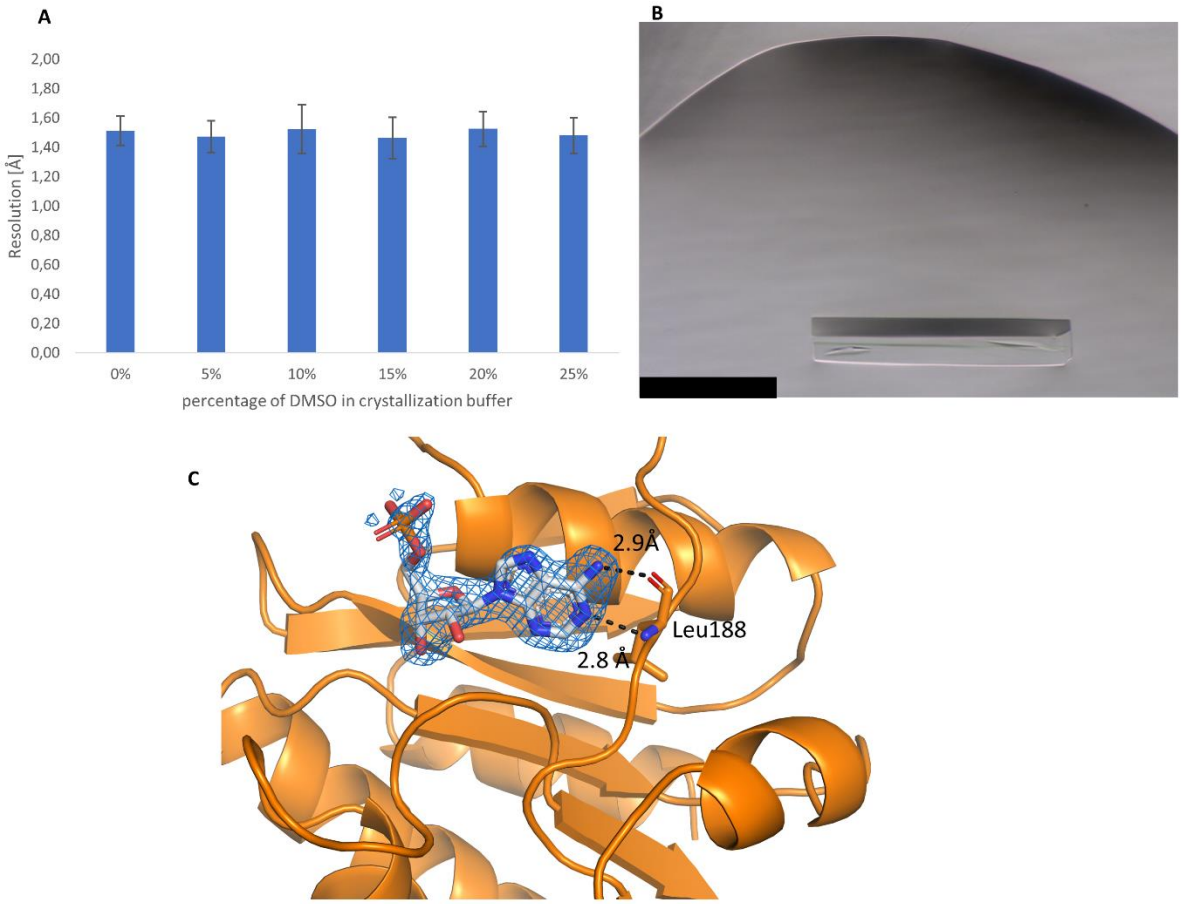

Figure 3.12: Results of the *Bs*CdaA crystal DMSO optimization and soaking trials. **A** Representation of the average resolution of *Bs*CdaA crystals if the crystallization buffer was supplemented with different amounts of DMSO. The y-axis shows the average resolution and the % DMSO used in the crystallization process is shown on the x-axis. Five crystals were tested per condition, the error bars correspond to standard deviation **B** Crystal of *Bs*CdaA in the APO state. The black bar corresponds to a length of 400 µM. The crystals grow in a condition consisting of 30 % PEG400, 100 mM HEPES pH 7.5 and 100 mM $MgCl_2$ and 20% DMSO to a size of 500x 100x50 µM. The black bar corresponds to a length of 400 µm. **C** CdaA monomer is displayed as *cartoon* in orange. In the active site, additional electron density could be observed in which an AMP molecule could be fitted. The polder omit map of the AMP molecule is displayed as blue mesh, contoured at a sigma level of 4.0. The AMP is represented as *stick* and *balls*, where the atoms are colored as phosphate: orange, oxygen: red, nitrogen: blue, carbon: grey. The polar bonds of the adenine moiety to the oxygen and nitrogen of the Leu188 backbone are depicted as black dashed lines. The binding equals the previously observed binding mode of the adenine moiety in complex with *Sa*cdaA (PDB-ID: 6GYX) or *Lm*CdaA (PDB-ID: 6HVL).

To prove that the crystal packing in combination with the solvent channels allows the soaking and binding of fragments, AMP, a known ligand of CdaA, was used. The soaking experiment was performed overnight with a concentration of 100 mM AMP. A dataset was collected at the 14.1 BESSY, Berlin. The resulting diffraction images were processed with *XDS* to a resolution of 1.79 Å with satisfying statistics (Table S.2). The phase problem was solved using the previously determined *Bs*CdaA APO structure in combination with *Dimple*. Iterative cycles of *Refmac* and manual model building in *Coot* lead to the final model with R_{work}/R_{free} values of

19.4 and 24.6%. Complete statistics are shown in Table S.2. The asymmetric unit revealed the expected back-to-back dimer of two *Bs*CdaA protomers. Careful inspection of the difference electron map revealed the presence of an AMP molecule in each of the active sites. The structure is depicted in Figure 3.12C including the polder omit map of AMP contoured at a sigma level of 4.0. This soaking experiment proves that the crystal packing of the *Bs*CdaA allows a successful soaking and binding of compounds to the active site of the protein.

Taken together, these experiments demonstrated that the crystallization system of *Bs*CdaA fulfills all prerequisites for a fragment screening campaign.

3.3.2 Fragment screening campaign of *Bs*CdaA in combination with the F2X-Entry screen

For the identification of a possible starting point for the design of inhibitory compounds against CdaA, an X-ray fragment screen was performed utilizing crystals from *Bs*CdaA in its APO state in combination with the fragment F2X-Entry screen. Further analysis was performed by *FragMAXapp*, a program which allows the combination of different processing and refinement programmes and finally the detection of fragment hits via *PanDDA* (Lima *et al*., 2021). After optimizing the crystallization system of *Bs*CdaA as previously described to allow a fast and easy handling hundreds of crystals were produced using the Swissci 3-drop plates in combination with the mosquito pipet robot. Crystals grew to their full size within 72 hours and could be overserved in 80% of the wells. In total, 203 crystals were harvested of which 192 were soaked with 96 different fragments from the F2X-Entry screen at a concentration of 100 mM overnight, while 11 *Bs*CdaA crystals were kept in the APO state. The APO crystals are necessary for the calculation of the Ground state model necessitated by *PanDDA*. Of the 203 crystals, 201 data sets could be collected at 14.1 BESY, Berlin within 36 hours. The datasets were automatically processed using *FragMAXapp*. The diffraction of the datasets ranges between 1.08 and 1.87 Å, averaging at 1.29 Å resolution. The R_{free} values range between 18.8 and 28.4 % averaging at 22.7%. (Fig3.13 A & B For additional information on the resolution, $R_{factors}$, completeness, I/sigma and $CC_{1/2}$ values for each collected dataset, see Table S.1.

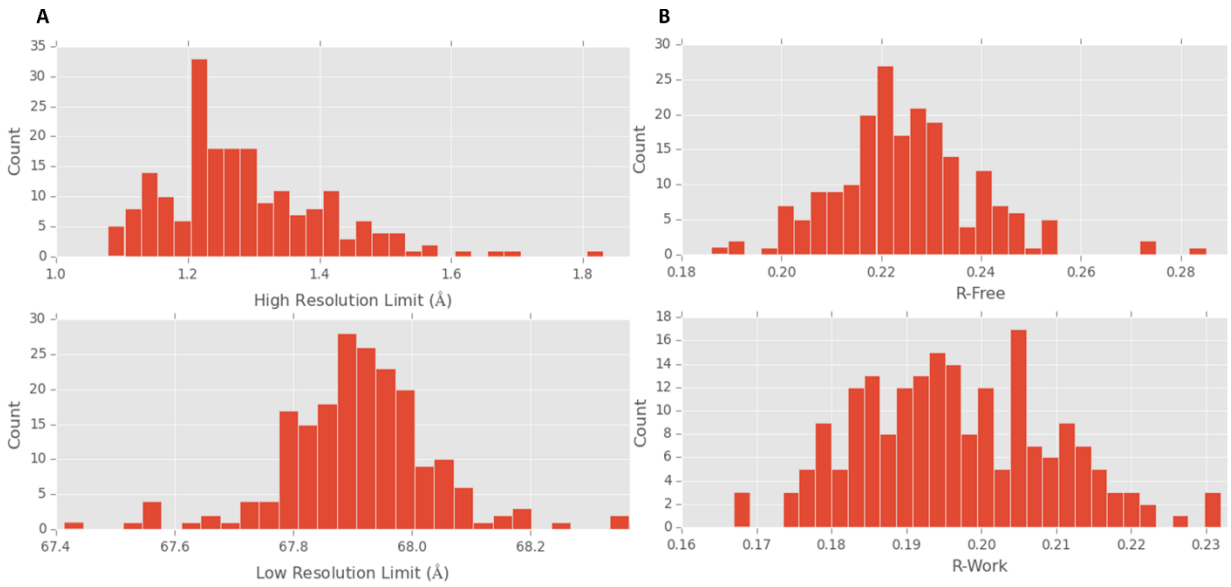

Figure 3.13: Diffraction limits and R_{work}/R_{free} value distribution of analysed datasets. **A** The bar diagrams show on the x-axis the high-resolution limit (top) and the low-resolution limit (bottom) and on the y-axis the count of the data sets. **B** The bar diagrams show on the x-axis the R_{free} value (top) and the R_{work} (bottom) and on the y-axis the count of the datasets.

All 201 datasets were processed using *panDDA.analyse* and 50 datasets were classified as interesting as the voxel approach used by PanDDa detect the possibility of the presence of a fragment. To detect datasets from *Bs*CdaA in complex with fragments, PanDDA calculates the combined ground state of all the crystal structure recorded by alignment. Afterwards, the calculated ground state is subtracted from each individual dataset. If differences between these two stats can be recognized, PanDDa declares this finding as event. In total, 72 events could be detected in 8 different sites. A PanDDA site is defined as a cluster of PanDDA events in the same region that are grouped together. In figure 3.14 the different sites are indicated in the structure of *Bs*CdaA. PanDDa events were manually examined using *panDDA.inspect* and in 64 events the respective fragment could be modelled into the PanDDA event map. The remaining events are most likely artefacts due to low quality maps, rearrangements in the crystal lattice due to soaking or unmodeled regions I n the event map which were too small to allow a rational allocation of the soaked fragment. Thus, these datasets were discarded. The fitted ligands were grouped into medium and high confidence according to their fit in the PanDDA event map and were exported using *PanDDA.export*. Afterwards, the maps containing hits were again refined using *Phenix*. In total, 32 different fragments were found to interact with *Bs*CdaA, resulting in a hit rate of 33%.

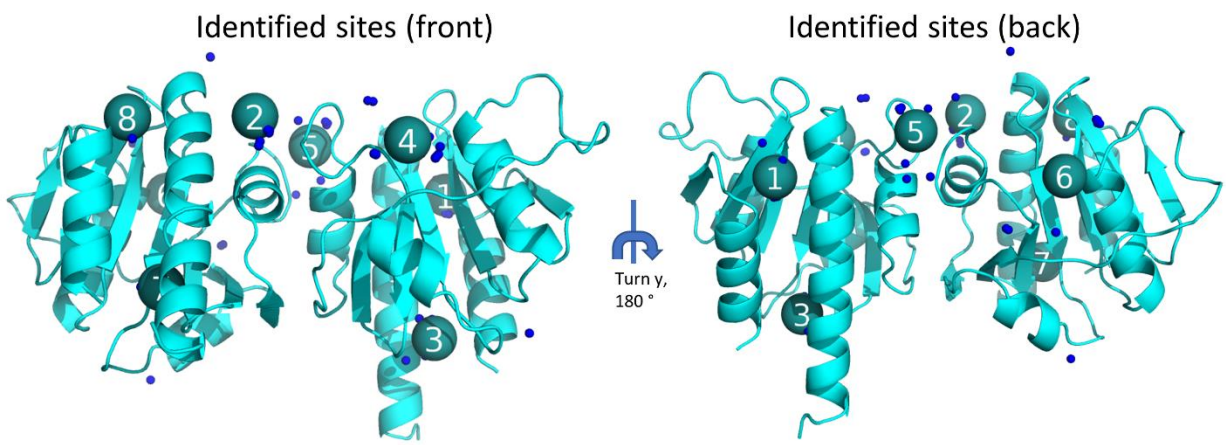

Figure 3.14: PanDDa summary of BsCdaA in combination with the F2X-Entry screen: The identified PanDDA events are shown as blue dots, clustered to a total of 8 different PanDDA sites depicted as spheres. The structure of *Bs*CdaA back-to-back dimer is shown in the *cartoon* representation (front and back side).

As the number of fragments and occupied sites is quite high, it was deemed reasonable to limit the subsequent efforts on the most promising candidates. The further development of fragments binding specifically to *Bs*CdaA would not be expedient, since *B.subtilis* is not a pathogenic organism. To identify hits which can be used for the development of an inhibitory compound against CdaA from different pathogenic organisms, the conversation score of CdaA was calculated using the *Consurf* server. To this end, the sequence of 20 different CdaAs originating from pathogenic organisms were used in combination with the BsCdaA APO structure. The used sequences are listed in Table S.4. Subsequently, all models with identified hits were superimposed on the model calculated by *ConSurf*. The resulting model showed that just six different fragments bound in a highly conserved region (Fig. 3.15 A).

There are some hits displayed twice, as two crystals were measured per fragment. Interestingly, this highly conserved region of CdaA represents the active site and dimerization interface of CdaA, rendering the six fragments bound to this site as good starting points for the further development of inhibitory compounds. A closer view regarding the exact localization of the fragments of interest and also an atomic representation is given in Figure 3.15A,B&C.

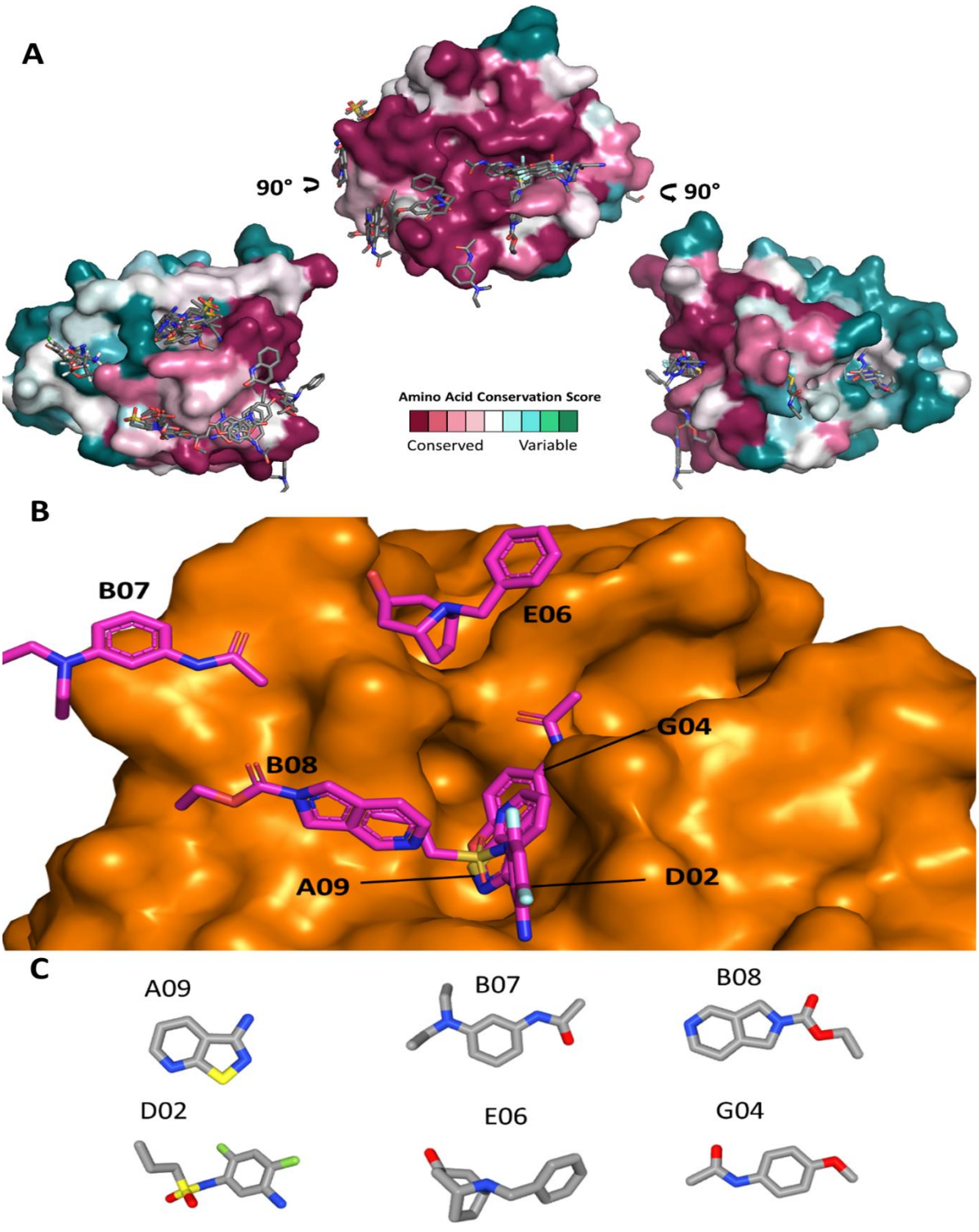

Figure 3.15: *Consurf* model of *Bs*CdaA superimposed with fragment hits. **A** The model derived from the *Consurf* surfer using the *Bs*CdaA structure as template is represented as *surface* where the single amino acids are colored according to the individual conservation score from conserved (violet) to variable (green). The fragment hits are depicted as sticks (carbon: grey, nitrogen: blue, oxygen: red, phosphate: yellow, fluoride: cyan). Some hits are displaced twice, as two crystals were measured per fragment. B: Close-up view of the fragments of interest Surface representation of *Bs*CdaA in orange. The six fragments which were previously determined to bind in the highly conserved region of CdaA are represented as *sticks.* **C** The six fragments in their skeletal structure, whereas carbon is colored in grey, sulfur in yellow, nitrogen in blue, oxygen in red and fluoride in green.

Fragment A09 is a heterocyclic, aromatic compound which binds in the active site and forms two polar contacts with the oxygen and nitrogen of Leu188 (Fig. 3.16). While this interaction pattern can also be observed for the adenine moiety of c-di-AMP, the fragment forms no stacking interactions with Tyr187. *Phenix* calculated an occupancy of about 55% for this fragment. The polder omit map and the *Pandda* event map are shown in Figure 3.16. Both maps are contoured at a sigma level of 2.

Fragment B07 consist of a phenyl ring with two extensions. No formation of polar contacts for this fragment could be observed, but the Pro168 adapts a new conformation if the fragment is present, allowing π-π interaction at a distance of 4 Å (Fig. 3.16). *Phenix* calculated an occupancy of 58% for this fragment, which was the highest occupancy observed for any of the six fragments bound to the conserved region of CdaA.

Fragment B08 consists of pyridine ring with an attached pyrrole ring which is further extended with an ester moiety. This fragment forms no polar contacts with the protein, but the Tyr187 is flipped and a π-π interaction at a distance of 3.9 Å could be observed (Fig. 3.16). *Phenix* calculated an occupancy of 38% for this fragment.

Fragment D02 consists of phenyl ring with two attached fluoride groups, one amine group and one sulfonamide-propane group. It binds near the active center of the protein, flipping the Tyr187 and building up a T-shaped π-π interaction at 4.0 Å with this residue (Fig. 3.16). Furthermore, this fragment forms polar contacts with the backbone oxygen and nitrogen atoms of Leu188 and also one polar contact with the oxygen atom of Thr202. *Phenix* calculated the occupancy of this fragment with 26 %.

Fragment E06 consists of a aza-bicyclic[3.2.1]octane ring with attached hydroxy and phenyl groups. The hydroxy group forms a polar interaction with nitrogen atom of Asn166 (Fig. 3.16). Furthermore, the His170 repositions below the fragment at a distance of 3 Å forming CH-π-interactions. *Phenix* calculated an occupancy of 38% for this fragment.

Fragment G04 consists of a central phenyl ring with an attached acetamide group and an ether group. No formation of polar bonds nor other kinds of interaction could be observed for this fragment (Fig. 3.16). *Phenix* calculated an occupancy of 24% for this fragment.

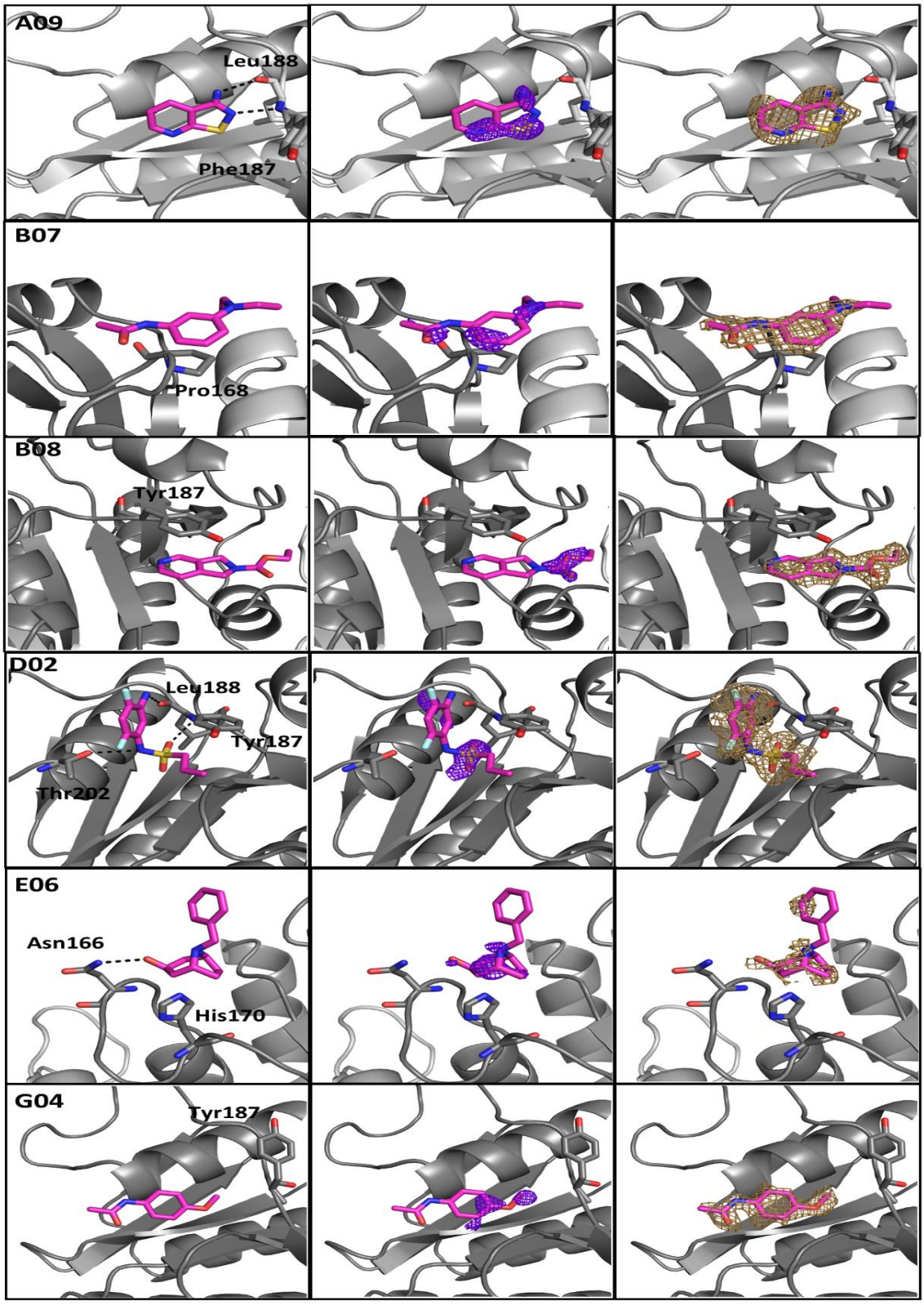

Figure 3.16: Representation of fragments and the corresponding polder omit maps and Pandda event maps. The *Bs*CdaA structure is displayed as *cartoon* in grey, and the fragments are displayed as *sticks*. The fragments and all amino acids involved in their coordination as well as the Tyr187 are shown in the first column. Polar interactions with a distance up to 3.1 Å are displayed as black dashed lines. The second column shows the polder omit maps contoured at a sigma level of 2 as purple mesh. The third column show the *Pandda* event maps contoured at a sigma level of 2 as yellow mesh.

Taken together, by combining the established crystallization system for *Bs*CdaA with the F2X-Entry screen and automated processing using *FragMAXapp*, six different fragments bound to the active and dimerization site of *Bs*CdaA could be identified. As this site is highly conserved, those fragments can serve as starting points for the development of inhibitory compounds against CdaA from pathogenic organisms.

3.3.3 Influence of the fragments on the cyclase activity of *Bs*CdaA

To investigate if any of the six identified fragments have an inhibitory effect on the cyclase activity of *Bs*CdaA, the coralyne assay was carried out. As the fragments are expected to be hardly soluble in the original buffer conditions, the assay was performed in presence of 20% DMSO. The fragment was added in a 10x fold molar excess (1mM) over the protein concentration. Using higher fragment concentration led to the precipitation of some of the fragments (A09, B07, E06 and G04).

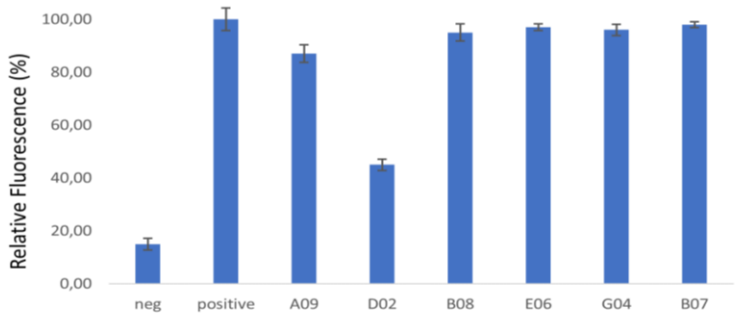

Figure 3.17: Cyclase activity of *Bs*CdaA in absence and presence of the six identified fragments tested in the coralyne assay. The y-axis displays the measured fluorescence The data were normalized by setting the fluorescence of the positive control to 100%. All measurements were performed as triplicates, shown are mean values, the error bars correspond to standard deviation.

Only fragments A09 and D02 lead to a reduction of the observed fluorescence, while the remaining ones (B07, B08, E06 and G04) had no conceivable effect (Fig. 3.18). The influence of D02 was the most prominent, as it reduced the measured fluorescence by about 50%. To confirm these results, several control experiments were carried out to prove that the reduction in the measured fluorescence can be correlated to a reduced cyclase activity (Fig. S.5). Unfortunately, these experiments showed that fragment D02 is able to reduce the fluorescence of coralyne by itself, most likely due to its fluoride groups. These findings leave the fragment A09 as only fragment which can reduce the cyclase activity of CdaA slightly.

As the performance of control experiments for the coralyne assay is rather highly resource consuming, a second assay should be established to monitor the cyclase activity of CdaA. Therefore, the Malachite Green assay was used. This assay detects the presence of free orthophosphate at a wavelength of 620 nm, but the product of the enzymatic activity of CdaA besides c-di-AMP is pyrophosphate. Therefore, pyrophosphatase was added to convert pyrophosphate to the detectable orthophosphate. A scheme of the adapted assay is shown in

Figure 2.1. Analogue to the coralyne assay, this assay was performed in presence of 20% DMSO due to the low solubility of the fragments.

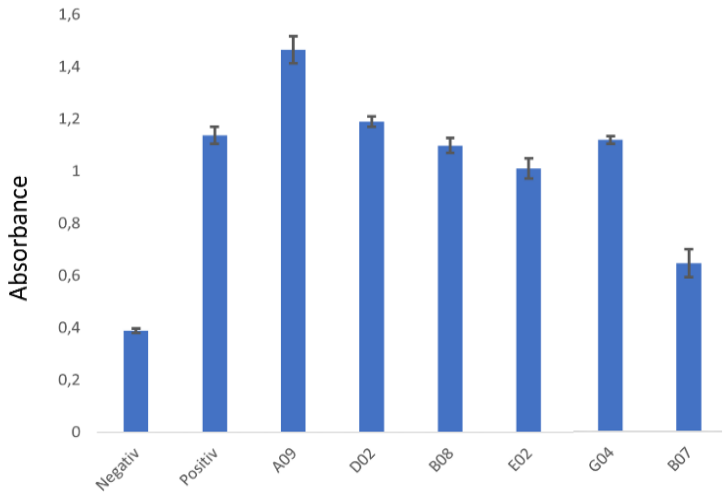

Figure 3.18: Cyclase activity of *Bs*CdaA in absence and presence of the six identified fragments tested in the Malachite Green assay. The y-axis shows the measured absorbance at a wavelength of 620 nm. The higher the measured absorbance, the more ATP was consumed All measurements were performed as triplicates. The error between the measurements is displayed by the error bars.

The activity assay performed in the presence of the fragments B02, B08, E02 and G04 showed the same absorbance as the positive control. Remarkably, the fragment B07 reduced the detected pyrophosphate to a rate of 50% (Fig. 3.19). Nevertheless, as this fragment showed no inhibition of the cyclase activity in the coralyne assay (Fig. 3.18) and the calculated occupancy of this fragment in the structure is very low (26%), it can be concluded that this fragment is not able to reduce the activity of *Bs*CdaA. Surprisingly, the measured absorption in the presence of the fragment A09 was about 25% higher than in the absence of any fragment. This is most likely as this aromatic ring system absorbs light with this specific wavelength.

In summary, both activity assays for CdaA applied here were prone for interactions with the tested fragments that altered the readout. A more stable assay to determine the effects of fragments on the cyclase activity would greatly facilitate the development of inhibitory compounds but remains to be established. Moreover, from the six tested fragments only A09 was able to reduce the cyclase activity of *Bs*CdaA slightly at the tested concentration. This highlights this fragment as promising starting point for the further development of an inhibitory compound.

3.3.4 Differential scanning fluorimetry

A thermal shift assay (TSA) was carried out to investigate the influence of the six identified fragments from the screen on the thermostability of the *Bs*CdaA. Binding of a fragment can lead to a change in the melting temperature which can be observed. To ensure the solubility of the fragments, the assay was performed in the presence of 20% DMSO. Compared to other methods, this method is performed with a larger excess (1000-fold) of fragment, as the estimated temperature shifts are rather small (Kranz & Schalk-Hihi, 2011).

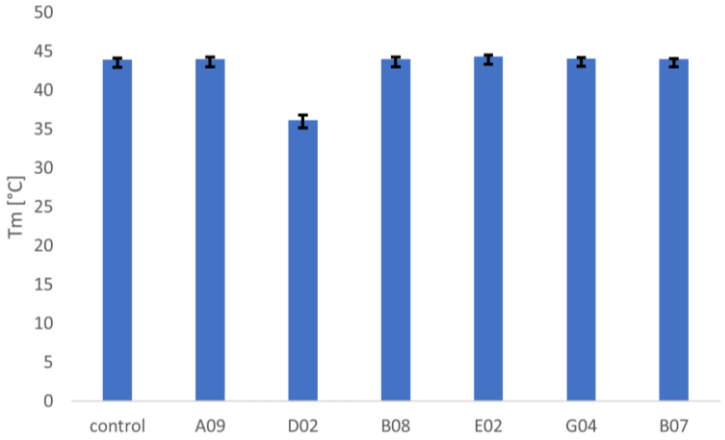

Figure 3.19: Differential scanning fluorimetry using *Bs*CdaA in combination with different fragments. The y-axis shows the melting temperature in [°C]. The measurements were performed as triplicates; therefore, the error bars indicate the difference between the single measurements.

Five of the six tested fragments did not change the melting temperature of *Bs*CdaA, while fragment D02 caused a decrease of about 9°C (Fig. 3.20). This large difference in the melting temperature was unexpected, as none of the previous experiments showed an alteration of the cyclase activity by fragment D02. These finding suggest a strong alteration of the protein upon binding of the fragment D02. Nevertheless, its calculated occupancy in the active site of the protein is 26%, indicating a rather weak interaction. Moreover, a second binding event for this fragment could be observed. The binding spot is located between the N- and C-terminal located α-helices, which might be responsible for the change in the melting temperature (Fig. S. 2).

To sum up all prerequisites for a fragment screen campaign could be fulfilled, using an improved crystallization system of *Bs*CdaA. The fragment screen was performed using this system in combination with the fragment screen F2X-Entry screen. In total, 32 different fragments bound the *Bs*CdaA could be identified. By identifications of highly conserved regions in CdaA, six different fragments were found as potential starting point for inhibitor design. The interaction between the fragments and *Bs*CdaA were further investigated by two different activity assays and a thermal shift assay. None of these fragments revealed and strong interaction with *Bs*CdaA which can be related to the binding in a conserved region. Therefore, a second line of drug finding was employed, starting from the structure of *Bs*CdaA bound to AMP (Fig. 3.12C)

3.4 Rational drug design from a natural ligand

To develop a potential inhibitory compound for the enzyme CdaA, this approach uses the structure of *Bs*CdaA in complex with AMP (Fig. 3.12C). As AMP should share nearly the equivalent interaction with *Bs*CdaA as its natural substrate ATP, mimicking of these interactions could potentially lead to an inhibitory compound which blocks the ATP-binding site. Therefore, a computer aided drug design (CADD) approach, utilizing the program *SeeSar* in combination with structural information was employed. Identified compounds were further investigated by biochemical and *in vivo* assays to determine the binding and inhibitory effects.

3.4.1 Proof of docking experiments performed with *SeeSar*

SeeSar is a program for the development of inhibitors and utilizes the so-called *HYDE-score* (HYdrogen bond and DEsalvation energy) in a highly visual way, as it displays every atom of a ligand in an intuitive color scheme. Moreover, an estimation of the binding affinity is given. In a first step, a potential binding site for ligands was defined by *SeeSar*, using the *Bs*CdaA APO-structure. The predicted binding site matches the known ATP binding site characterized in several crystal structures of CdaA (PDB-ID: 6GYX, 4RV7). Employing the docking mode of *SeeSar*, the molecules ATP and AMP were docked into the binding site (Fig 3.20). The predicted binding position of AMP matches the position in the available crystal structure (Fig. 12C).

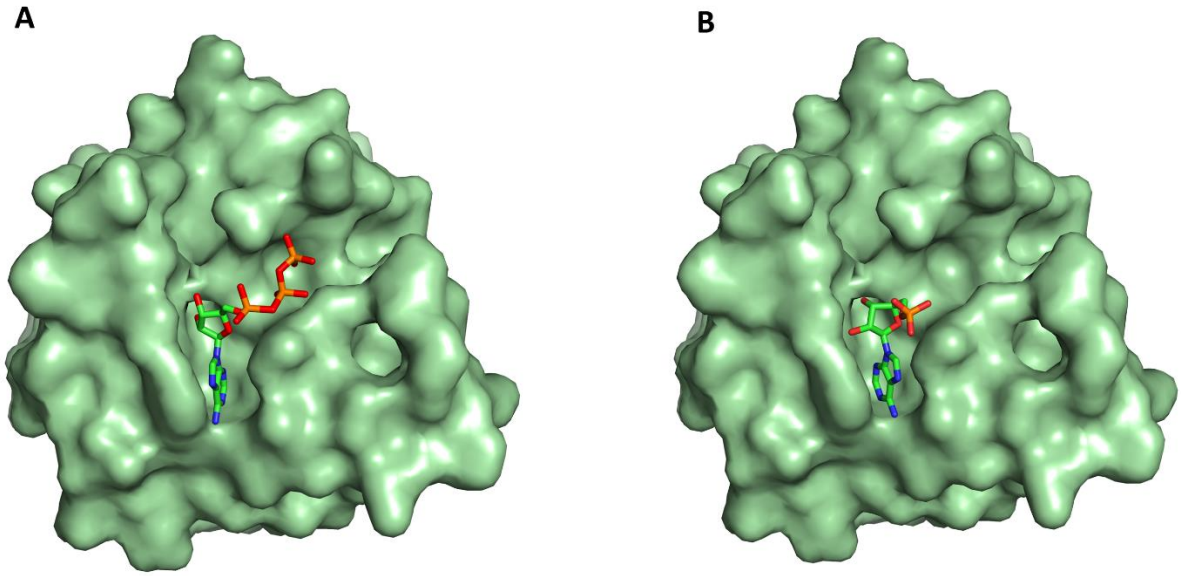

Figure 3.20: Predicted binding sites of ATP and AMP to *Bs*CdaA. The program *SeeSar* was employed to dock the compounds ATP (**A**) and AMP (**B**) to the active site of the protein. The structure of *Bs*CdaA is represented as surface in pale green. The AMP and ATP molecules are represented as *sticks*, colored by atom type (phosphate: orange, oxygen: red, nitrogen: blue, carbon: green).

Surprisingly, the estimated binding affinities for both ATP (mid µM range) and AMP (low mM range) are rather low, considering that ATP is the natural substrate for CdaA.

To confirm the predicted binding affinities of ATP and AMP to *Bs*CdaA *in vitro,* ITC experiments were carried out. As the binding affinities are rather low calculated, *Bs*CdaA was used with a

concentration of 1.2 mM and the ligands with a concentration of 12 mM, so the usual 10-fold excess.

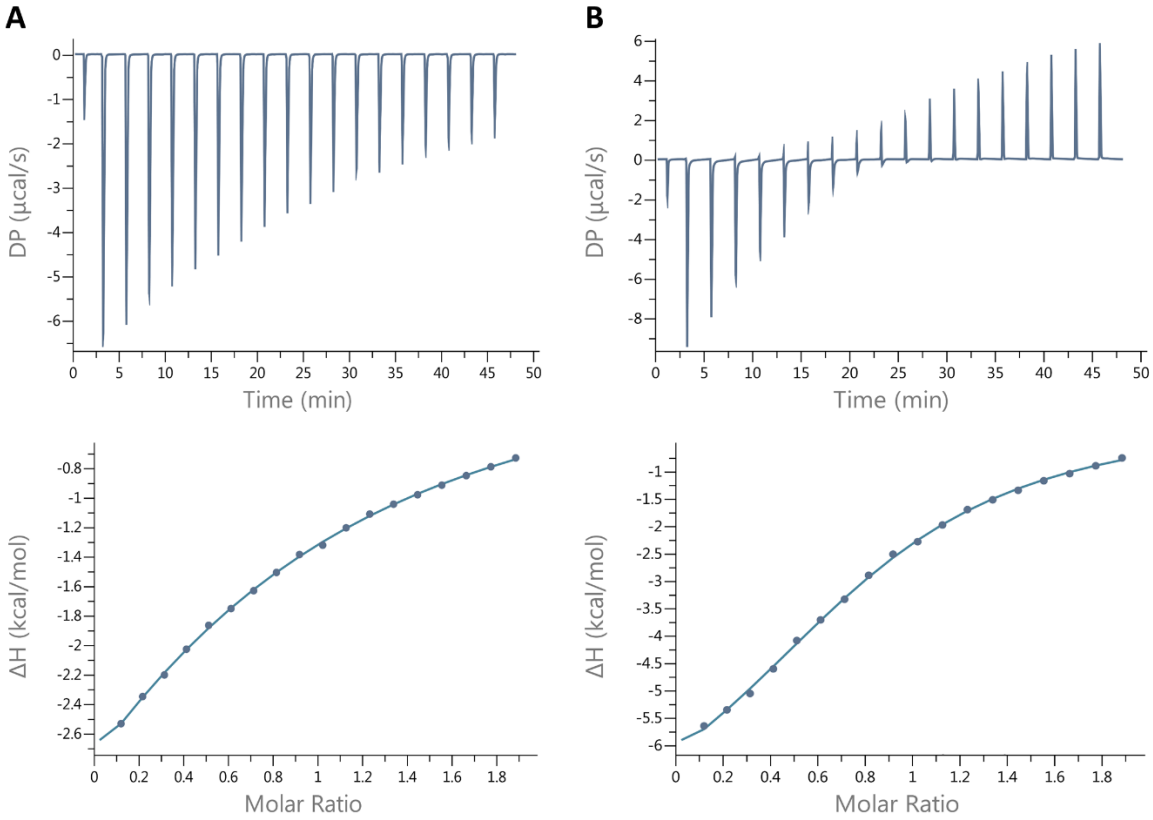

Figure 3.21: Binding titration of *Bs*CdaA with AMP and ATP monitored by isothermal titration calorimetry (ITC). **A** Cell and syringe contained 1.2 mM BsCdaA and 12 mM AMP, respectively. The calculated binding affinity of AMP to *Bs*CdaA is 1.77±0.09 mM. The calculated stoichiometry is 0.87. **B** Cell and syringe contained 1.2 mM BsCdaA and 12 mM ATP, respectively. The calculated binding affinity of ATP to *Bs*CdaA is 393±17 µM. The calculated stoichiometry is 0.92. For the experiments, the respective ligand to buffer and buffer to protein controls were performed and subtracted. The fitting mode "One set of sites" were utilized

The ITC experiments showed that *Bs*CdaA binds ATP and AMP with only weak affinity (K_D=393±17 µM and 1.77±0.09 mM, respectively; Fig. 3.21), both with a stoichiometry near 1.

As the binding affinities determined by ITC match the predicted affinities by *SeeSar*, the programs estimates can be considered as sufficiently reliable to be used for the development of inhibitory compounds.

3.4.2 Inhibitor detection using the structure of BsCdaA in complex with AMP

Fragmentation of known binding partners is a common approach for the development of inhibitors (León *et al*., 2021). To apply it here, the contributions of the single components of AMP to the overall binding were investigated using *SeeSar* in combination with the structure of *Bs*CdaA bound to AMP. AMP was split in three different compounds, namely

orthophosphate, ribose, and adenine. While orthophosphate and ribose exhibited calculated binding affinities in the high mM range, adenine is expected to bind in a low mM range. This value is highly similar to the previously determined and estimated binding affinity of AMP to CdaA. Moreover, the calculated LE score, which describes the binding energy per atom of a ligand, is calculated higher for adenine compared to AMP. These findings implicate that the major binding energy of AMP derives from the adenine moiety. Interestingly, *SeeSar* docked adenine in a 180° rotated fashion compared to the adenine moiety in the crystal structure of *Bs*CdaA in complex with AMP (Fig 3.22A). In the *Bs*CdaA structure the adenine moiety interacts via the amine group with the oxygen group of Leu188 and the nitrogen at position 6 interacts with the nitrogen auf Leu188 by the formation of hydrogen bounds. In contrast, SeeSar predicts the adenine to interact with the protein via hydrogen bond formation between the nitrogen at position 9 and the oxygen of Leu188 and the nitrogen at position 9 and the nitrogen atom of Leu188 (Fig. 3.22B). To address this unexpected finding, structural experiments were conducted by soaking *Bs*CdaA APO crystals with adenine. All datasets described in the following part of the thesis were equally processed and refined using *XDS* for data processing and a combination of *Phenix/Refmac5* and manual model building in *Coot* for refinement. The corresponding tables are listed in the appendix, table S.2.

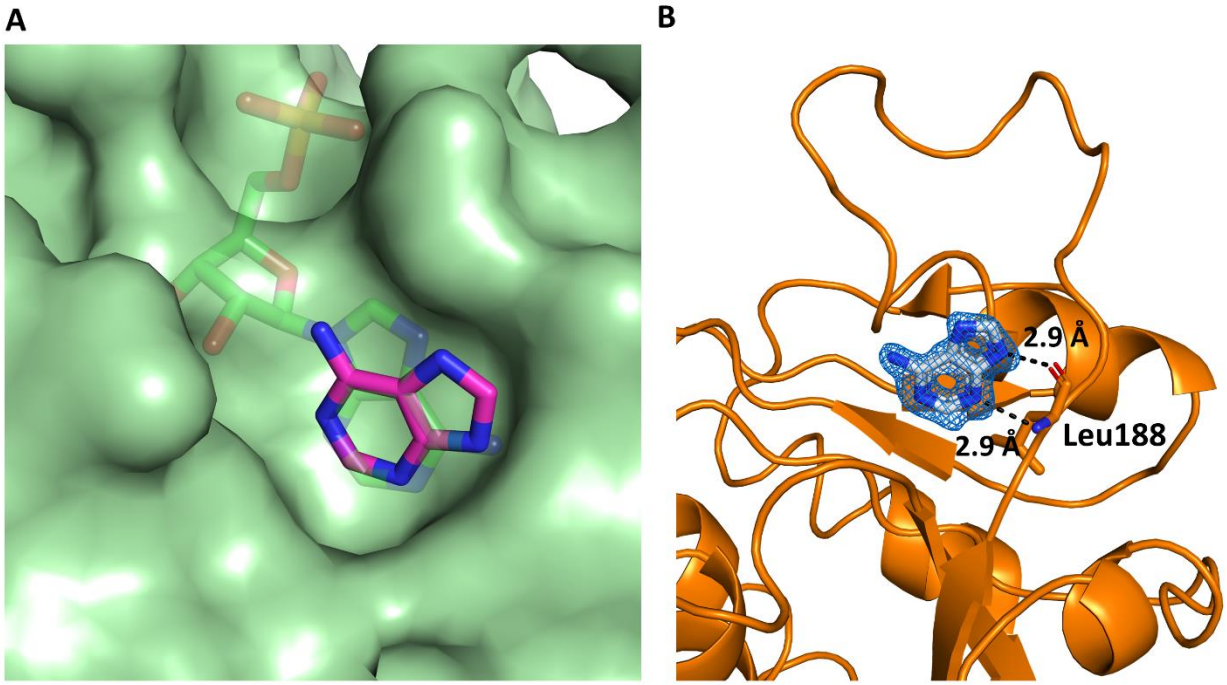

Figure 3.22: Binding mode of adenine to *Bs*CdaA. **A** Binding of adenine and AMP to *Bs*CdaA as predicted by SeeSar. The protein is presented as *surface* in pale green, while the AMP and adenine are depicted as *sticks*. For adeneine: C atoms in purple, N atoms in blue. For AMP: C atoms in green, O atoms in red, N atoms in blue, P atoms in orange. **B** Crystal structure of adenine binding to *Bs*CdaA represented as *cartoon* in orange. The adenine is displayed as *sticks* and the polder omit map contoured at a sigma level of 4.5 as blue mesh. The polar bonds of the adenine to the oxygen and nitrogen of the Leu188 backbone are depicted as black dashed lines. The C atoms of the adenine are colored in grey, the N atoms in blue.

The structure of *Bs*CdaA in complex with adenine showed that the adenine binds in the interaction pattern which was predicated by *SeeSar* (Fig. 23A). It can be observed that the prediction and the structure obtained by X-ray crystallography do not only share the interaction pattern but also exhibit an overall well matching localization of adenine.

As adenine is an essential molecule in every cell, it cannot be used as inhibitor for CdaA. Consequently, the atomic composition of adenine should be altered in a way that the resulting compound still can build up the same interactions as adenine but is less prone to bind to other proteins which interact with an adenine moiety. To this end, the *ReCore* subprogram of *SeeSar* was employed in combination with a specified database (*Molport)*. This approach should lead to the identification of compounds with a similar scaffold and same interaction pattern. 7H-pyrrolo[2,3-d]pyrimidin was identified as possible follow-up compound with the same interaction pattern as adenine. The polar bonds formed between the adenine and the backbone of Leu188 are equal to the predicted of 7H-pyrrolo[2,3-d]pyrimidin to *Bs*CdaA. Also, *SeeSar* predicts the binding affinity in a low milli-molar range, equal to the predicted values of adenine. Therefore, this compound was applied to soaking experiments with *Bs*CdaA. The resulting structure is shown at a resolution of 1.75 Å in Figure 3.23. The corresponding crystallographic and refinement statistics are shown in table S.2.

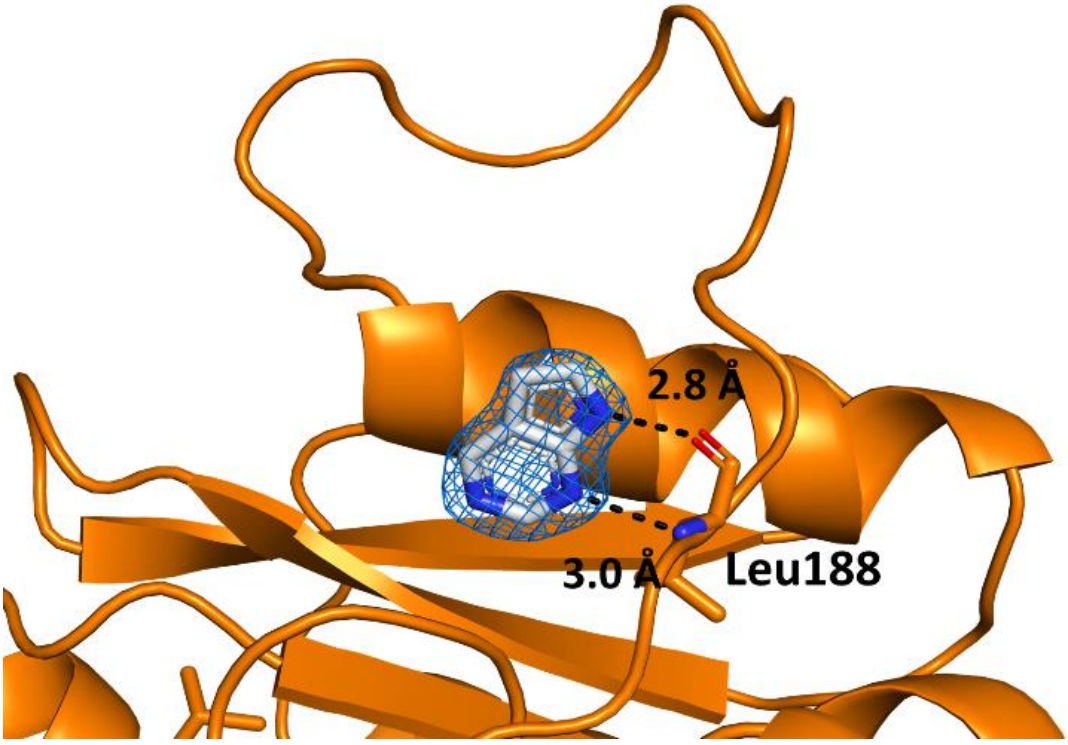

Figure 3.23: X-ray structure of *Bs*CdaA bound to 7H-pyrrolo[2,3-d]pyrimidin. *Bs*CdaA is represented as *cartoon* in orange, the 7H-pyrrolo[2,3-d]pyrimidin is depicted as *sticks* and the polder omit map contoured at a sigma level of 4.5 as blue mesh. The polar bonds of the adenine to the oxygen and nitrogen of the Leu188 backbone are depicted as black dashed lines.

The polder omit map contoured at a sigma level of 4.5 confirms the presence of the soaked compound, 7H-pyrrolo[2,3-d]pyrimidin in the active center of the protein. Moreover, it forms

the same polar interactions as observed for adenine with the oxygen and nitrogen of the Leu188 backbone.

To identify compounds exhibiting inhibitory effects towards *Bs*CdaA and partially consist of 7H-pyrrolo[2,3-d]pyrimidin a substructure search was employed using the database of *Molport*. In total, 9775 compound were identified. The compounds which were elongated uses the N3 or N6 atom of the 7H-pyrrolo[2,3-d]pyrimidin were rejected, as these atoms are required for the interaction with the Leu188 backbone. This reduces the number to 130 compounds. Furthermore, all compounds which possess an elongation at the C8 or C7 atom were also rejected, reducing the number to 8 compounds. The identified compounds were docked into the structure of *Bs*CdaA using *SeeSar*. Two of the compounds were predicted to bind in the mid-micromolar range, namely Ruxolitinib and Barcitinib (Fig. 3.25A&B).

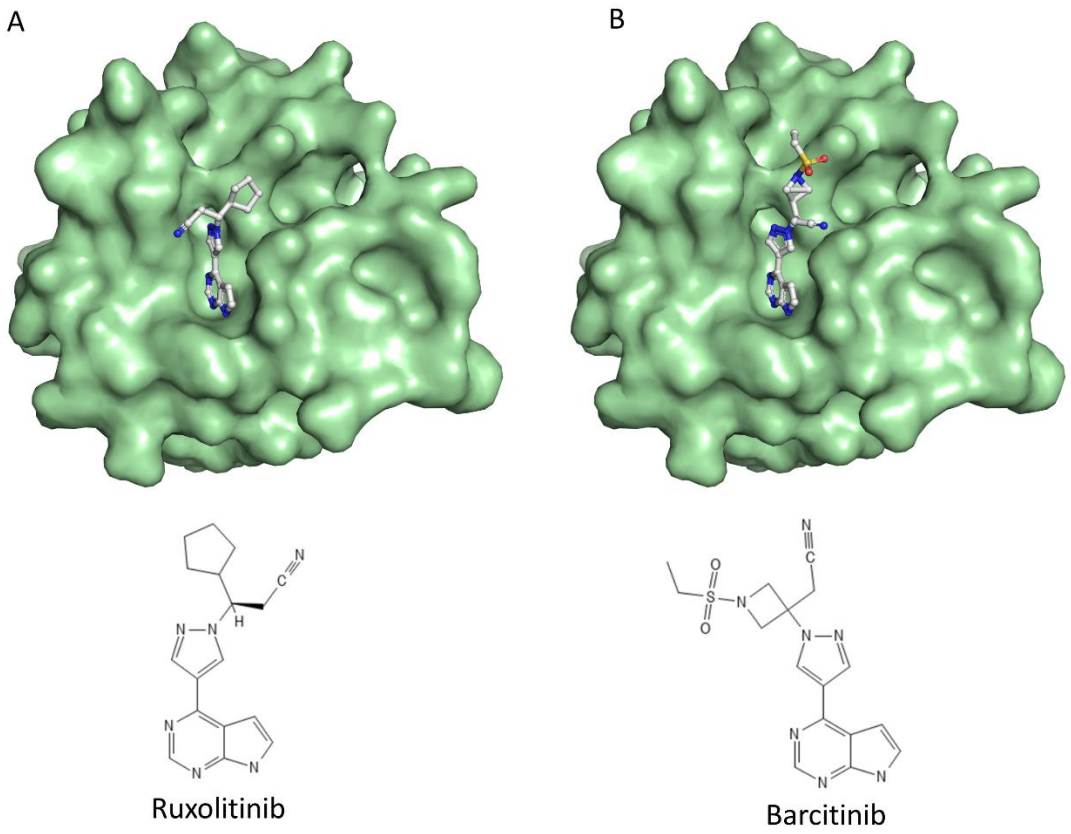

Figure 3.24: Presentation of Ruxolitinib and Barcitinib docked to *Bs*CdaA via *SeeSar*. Both FDA/EMA approved drugs were identified *via* an substructure search using 7H-pyrrolo[2,3-d]pyrimidin in the molport database and were docked with mid-micromolar affinities to the structure of *Bs*CdaA. **A** presents the results of the docking experiments of *Bs*CdaA with Ruxolitinib, B the results of *Bs*CdaA with Barcitinib. *Bs*CdaA is presented I the *surface* mode, Ruxolitinib and Barcitinib are depicted as *sticks* and *spheres*. The atoms of both compounds are equally colored (C atoms in grey, N atoms in blue, O atoms in red and S atoms in yellow).

Both identified compounds are FDA/EMA approved drugs and function as tyrosine kinase inhibitors. They share both the pyrollopyrimidin moiety connected to a pyrazol-ring and further to a cyanid group. While Ruxolitinib has a cyclopentane group, Barcitinib instead consists of an aziridine ring followed by a sulfone group. Both compounds were tried to soak into *Bs*CdaA APO crystals. Unfortunately, crystals soaked with Barcitinib exhibit no additional density for this compound. The resulting structure of *Bs*CdaA in complex with Ruxolitinib was solved with a resolution of 1.25 Å (Fig. 3.26A). The corresponding crystallographic and refinement table are shown in table S.2.

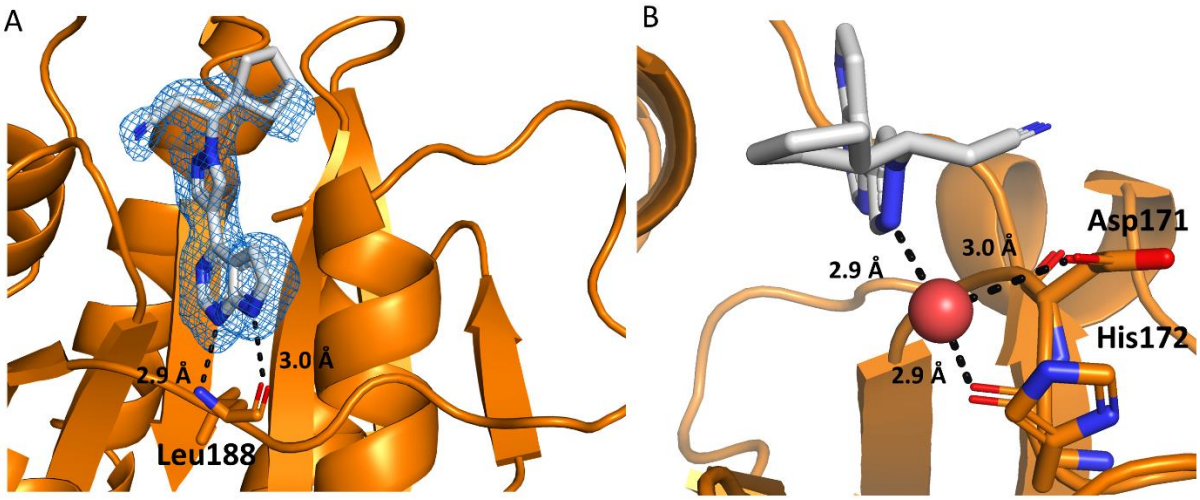

Figure 3.25: Presentation of the X-ray structure of *Bs*CdaA in complex with Ruxolitinib. The protein is shown as *cartoon* in orange. Ruxolitinib is depicted as *sticks* **A** The polder omit map contoured at a sigma level of 4.5 as blue mesh. The polar interactions of the pyrollopyrimidin to the oxygen and nitrogen of the Leu188 backbone are depicted as black dashed lines. **B** The water which coordinated by the N2 atom of the pyrazol ring of Ruxolitinib is depicted as red sphere. Further amino acid residues which are involved in polar interaction with the water molecule are depicted as *sticks*. The polar interactions are indicated as black dashed lines.

The compound is localized in the active site of the protein, verified by the depicted polder omit map, contoured at a sigma level of 4.5. Analysis with *Coot* revealed the pyrollopyrimidin ring interacts with the oxygen and nitrogen of the Leu188 backbone as it was previously observed for adenine. Furthermore, the interaction of the N2 atom of the pyrazol-ring with a water molecule could be observed (Fig. 3.26B). This water molecule additionally forms polar bonds with the amino acid residue Asp171 with 2.9 Å and to the oxygen backbone of His172 with 3.0 Å. The same interaction pattern was observed in the other monomer in the asymmetric unit.

Taken together, the FDA/EMA approved drug Ruxolitinib was identified via defragmentation of AMP and subsequent substructure search as potential inhibitor for *Bs*CdaA and confirmed to bind to the active site of the protein CdaA *Bacillus subtilis.*

3.4.3 Soaking experiments with *Lm*CdaA

To investigate if the binding mode of Ruxolitinib to *Bs*CdaA is conserved among other organisms, soaking experiments with crystals of *Lm*CdaA in the APO form were performed. Therefore, the protein was overexpressed, purified, and crystallized as published (Heidemann *et al*., 2019). The soaking experiment was performed analogous to the soaking of *Bs*CdaA and a dataset was collected. The resulting structure was determined at a resolution of 2.85 Å. Further statistics for the dataset and refinement are listed in table S.2.

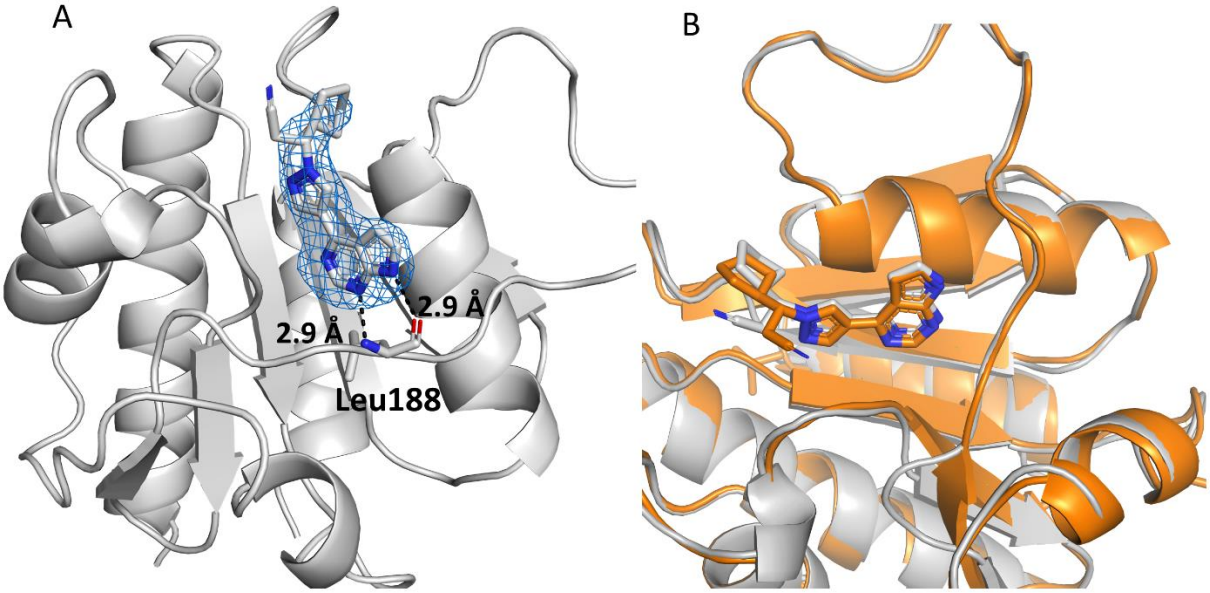

Figure 26: X-ray structure of *Lm*CdaA bound to Ruxolitinib. **A** *Lm*CdaA is represented as *cartoon* in grey, Ruxolitinib is depicted as *sticks,* and the polder omit map contoured at a sigma level of 3.0 as blue mesh. The polar bonds of the pyrollopyrimidin to the oxygen and nitrogen of the Leu188 backbone are depicted as black dashed lines. **B** Alignment of the x-ray structures of *Lm*CdaA (grey) and *Bs*CdaA (orange) both depicted as *cartoon*. Ruxolitinib is depicted as *sticks* and the colored in the teint of the respective. The overall r.m.s.d. value was calculated with 0.78 Å for alle Cα-atoms.

Careful inspection of the electron density in the active center of *Lm*CdaA reveals the presence of parts of Ruxolitintib (Fig. 26 A). The polder omit map contoured at a sigma level of 3 shows that indeed the pyrazol and the pyrollopyrimidin moiety are clearly present, while the cyanide group and parts of the cyclopentane are missing. Alignment with the structure of *Bs*CdaA in complex with Ruxolitinib shows that the localization of the ligand within the active center of the proteins is identical (Fig. 26B). These findings suggest that the binding mode is conserved between CdaA enzymes. This renders the crystallization system of *Bs*CdaA as suitable system for the development of potential inhibiting compounds based on structural knowledge of Ruxolitinib and its interaction with *Lm*CdaA and *Bs*CdaA.

3.4.4 Coralyne activity test of CdaA with Ruxolitinib

To examine the influence of Ruxolitinib on the activity of BsCdaA *in vitro* the coralyne assay was employed. Different concentrations of Ruxolitinib were added to enable the determination of an IC_{50} value, employing the coralyne assay (Fig. 27A&B).

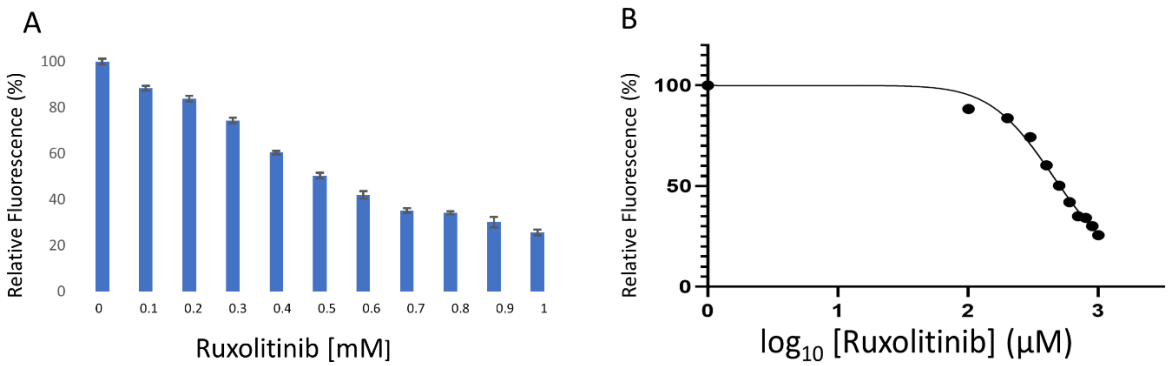

Figure 3.27: Fluoresence of the product of *Bs*CdaA determined using the coralyne assay in presence of increasing concentrations of Ruxolitinib. **A** The x-axis shows the applied concentrations of Ruxolitinib. The y-axis shows the normalized fluorescence. The experiment was performed in triplicates, shown are mean values, the error bars correspond to standard deviation. The sample without Ruxolitinib was set to 100%. **B** This plot shows the fit of the results from the A. Therefore, the program *Graphprism* was employed, and the data were fitted using variable-slope-4-parameter model. The calculated IC_{50} value was 2.7±0.1 µM.

The increase of Ruxolitinib concentration led to a decrease of cyclase activity, indicating an inhibitory effect of the compound. As the activity decreases with increasing inhibitor concentration, it can be concluded that Ruxolitinib functions as competitive inhibitor for ATP, which is in line with the structural findings as Ruxolitinib binds in the active center of the protein. The IC_{50} value for Ruxolitinib was determined as 2.7±0.1 µM in this set-up.

To investigate if Ruxolitinib is also able to reduce cyclase activity of CdaA from the pathogenic organisms *S.pneumoniae, S.aureus, E.faecium or L.monocytogenes,* the coralyne assay was carried out with the respective CdaAs and a concentration of 500 µM Ruxolitinib, which equals the previously concentration of Ruxolitinib to reduce the activity of *B.subtilis* CdaA at around 50%.

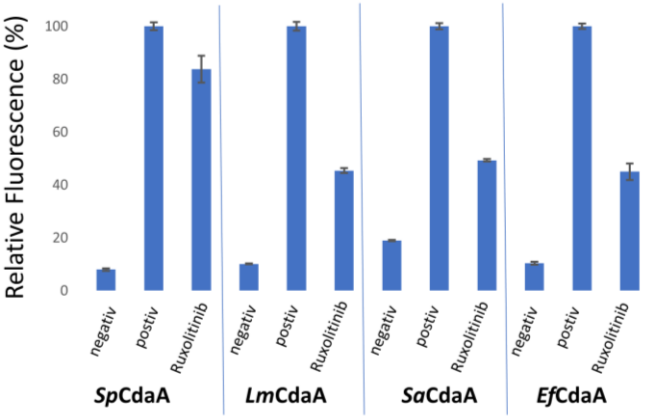

Figure 3.28: Cyclase activity of CdaA from different organism in the absence and presence of Ruxolitinib, determined using the coralyne assay. The y-axis shows the relative measured and normalized fluorescence in %. Ruxolitinib were added at a concentration of 500 µM. The experiment was performed in triplicates, shown are mean values, the error bars correspond to standard deviation. The positive control was set to 100%.

It can be observed that the cyclase activity in presence of Ruxolitinib is equally reduced for the CdaAs of *E.faecium, L.monocytogenes, B.subtilis* and *S.aureus* by around 50% (Fig. 28). The activity of the CdaA from *S.pneumoniae* was less reduced with an observed decrease of 20%.

3.4.5 ITC experiments with *Bs*CdaA and Ruxolitinib

To investigate the binding of Ruxolitinib to *Bs*CdaA, ITC experiments were carried out. The protein was used with the previously established of 1.2 mM while the ligand was used with a maximum concentration of 1.2 mM due to solubility issues. The results are depicted in Figure 29.

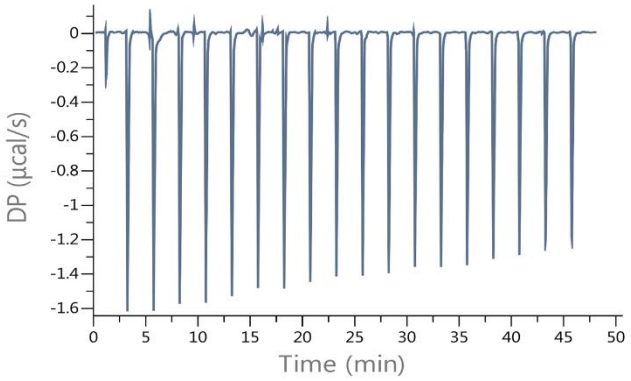

Figure 3.29: ITC experiment using *Bs*CdaA and Ruxolitinib. No binding constants could be determined from this experiment. For the experiments, the respective ligand to buffer and buffer to protein controls were performed and subtracted.

Unfortunately, the result cannot be used to determine the binding affinity of Ruxolintib towards *Bs*CdaA. On the other hand, as the DP area of each injection decreases it can be concluded that Ruxolitinib indeed binds to *Bs*CdaA in this experimental setup. However, this assay needs to be further optimized to give raise to interpretable data which can be useful in future for optimization of an inhibitor of CdaA deriving from Ruxolitinib. Possible optimization could include different ligand/receptor concentrations, usage of DMSO, or switching the ITC device to reach higher sensibility with lower concentrations of ligand and receptor.

3.4.6 Antimicrobial activity of Ruxolitinib

After having established Ruxolitinib as a functional inhibitor for CdaA from different pathogenic organisms *in vitro*, its suitability as an antimicrobial drug was examined next. As diadenylate cyclases are essential proteins in bacteria possessing the second messenger c-di-AMP, the treatment with Ruxolitinib should have an observable effect on their growth. The experiments presented in this section were conducted by Robert Warnecke, Department of General Microbiology, AG Stülke, Goettingen.

Three different *B.subtilis* strains were used in growth experiments in the presence of different concentrations of Ruxolitinib, ranging von 0-200 µM.

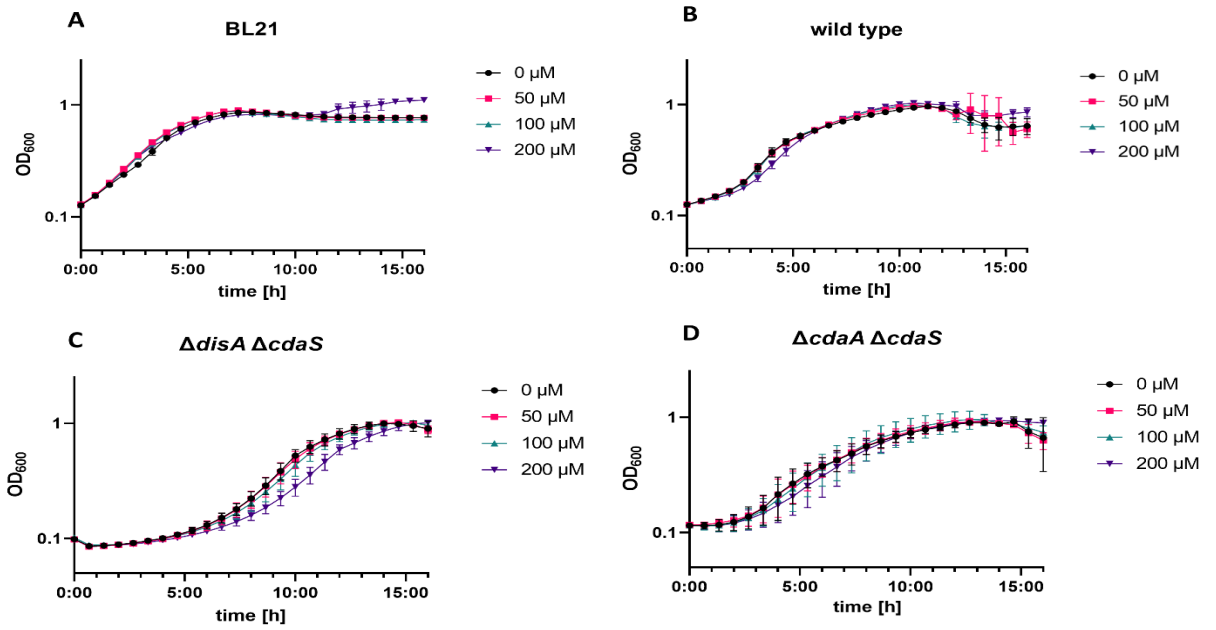

Figure 3.30: Growth curves of bacterial strains in presence of different Ruxolitinib concentrations. For all diagrams, the y-axis displays the OD600 value, while the x-axis displays the time in hours. The experiments were performed in MSSM media supplied with 5 mM KCl. **A** presents the growth of the *E.coli* BL21 strain. **B** presents the growth of wild type *B.subtilis.* **C** presents the growth of an *B.subtilis* strain, where the sequences encoding for the DAC domain containing proteins DisA and CdaS are removed; CdaA is the only remaining protein with a DAC domain. **D** presents the growth rate of a *B.subtilis* which only harbors one protein with a DAC domain, DisA.

To prove the inhibitory effect of Ruxolitinib against diadenylate-cyclase proteins, *E.coli* (BL21) cells were used as control, as the genome of this gram-negative bacteria does not encode for any diadenylate cyclases. The growth rate of E. coli BL21 was not influenced by the presence of Ruxolitinib, indicating that none of its essential proteins was affected by the compound (Fig. 31A). The same result could be observed for the *B.subtilis* strain missing the diadeylate cyclases CdaA and CdaS (Fig. 31D). This result suggests that no essential protein for the growth rate is affected by Ruxolitinib in this strain. The *B.subtilis wild-type* strain which harbors the three diadenylate cyclases CdaA, CdaS and DisA shows a slight delay in the growth rate, if Ruxolitinib is added with a concentration of 200µM (Fig. 31B). The *B.subtilis* strain which only encodes for the diadenylate cyclase CdaA (Fig. 31C) exhibits a decrease in the growth rate if Ruxolitinib is added with a concentration of 100µM. This effect is even more pronounced, when Ruxolitinib is added with a concentration of 200 µM. These results are further debated in the discussion part.

In summary, it could be shown that a *B.subtilis* strain, which does not possess a CdaA does not show any alterations in its growth rate, independently of the Ruxolitinib concentration, while the strains which possess CdaA exhibit a reduced growth rate. It can be concluded that Ruxolitinib is able to reduce the activity of the *Bs*CdaA *in vivo* due to specific inhibition of the enzyme CdaA. Nevertheless, this compound cannot be used directly as antibiotics it is already used as cancer drug. This is further debated in the discussion part of this thesis.

4 Discussion

Organism from all kingdoms of life need to be able to rapidly adapt to changing environmental influences to survive. For this reason, they possess numerous signaling pathways, and, regardless of their kingdom, the signal molecules involved are often nucleotide-based (Braun *et al*, 2021; Rhoads, 1999; Gottesman, 2019). For the bacterial kingdom, the second messenger metabolites cAMP, (p)ppGpp, c-di-GMP and c-di-AMP have been most extensively studied, which brought to light a plethora of different pathways in which these signal molecules are involved (Hengge *et al*, 2019).

The first evidence of the natural occurrence of the bacterial second messenger c-di-AMP was discovered in 2008 (Witte *et al*, 2008). This discovery marked the starting point of a new research field revolving around this metabolite, giving insights into its biosynthesis, degradation, and its role in regulatory pathways (Corrigan & Gründling, 2013; Commichau *et al*, 2015; Stülke & Krüger, 2020). The first protein discovered to synthesize c-di-AMP was the DNA integrity scanning protein A (DisA) from the bacterium *Thermotoga maritima* (Witte *et al*, 2008). By evaluating structural information, it was clarified that the enzyme synthesizes its main product c-di-AMP in a metal ion-dependent fashion from two substrate ATP molecules (Müller *et al*, 2015). Therefore, eight DisA monomers, each consisting of an N-terminally located diadenylate cyclase (DAC) domain and a C-terminally located signaling domain, assemble as two tetrameric rings which further oligomerize as an octamer (Müller *et al*, 2015; Witte *et al*, 2008). It has been shown that this octamer is stable *in vitro* as well as *in vivo*, proofing that this assembly is not just an artefact of crystallization. The two tetrameric rings face each other in a “face to face” manner, forming four head-to-head dimeric assemblies in total which are referred to as the catalytic units (Müller *et al*, 2015; Witte *et al*, 2008).

Today, five different classes of proteins are known to feature a DAC domain (Corrigan & Gründling, 2013; Blötz *et al*, 2017; Commichau *et al*, 2019). Nevertheless, the genome of most bacteria, like the human pathogenic organisms *Streptococcus aureus*, *Staphylococcus pneumoniae* or *Enterococcus faecium,* encodes for just a single diadenylate cyclase named CdaA. Several studies have shown that c-di-AMP is essential under standard growing conditions for some bacteria. However, it also has been shown that high excess of this messenger nucleotide is harmful to cells, earning it the nickname “essential poison” (Gundlach *et al*, 2017a, 2015; Woodward *et al*, 2010; Mehne *et al*, 2013; Commichau *et al*, 2019a). Because c-di-AMP synthesizing proteins are essential in bacteria, while having no known occurrence in eukaryotes, these proteins, and in particular CdaA, are potential targets for the development of a new antibiotics (Rosenberg *et al*, 2015; Commichau *et al*, 2019).

The development of antibiotics with a new mode of action against multi resistant bacteria is an urgent necessity to be able to fight one of the biggest threats to global health, development and food security (WHO, 2015). Currently, around 700.000 deaths annually are caused by

infections with bacteria, and according to the WHO, this number is expected to rise to up to 10 million in 2050 (WHO, 2019a). Therefore, this work focusses on the protein CdaA of various, and among them human pathogenic, bacteria in which CdaA is the sole c-di-AMP synthesizing enzyme. In this chapter the function, metal ion-dependence and oligomerization of the protein CdaA are discussed. Moreover, the usage of kinase inhibitors as starting points for the development of new antibiotics will be discussed with a special focus on the inhibitory effect of Ruxolitinib on CdaA. Furthermore, inhibition by Ruxolitinib will be compared to known DAC inhibitors IPA-3 and Br-TH (Chen *et al*., 2018; Li *et al*., 2022). Finally, the success of a fragment screen campaign based on CdaA from *Bacillus subtilis* is discussed, with an outlook as to which methods could be applied to develop the identified compounds into a possible lead compound.

4.1 CdaA structure, function and metal-ion specificity

The first structure of the DAC domain of CdaA was published in 2015 in the form of its complex with ATP (Rosenberg *et al*, 2015). Comparison of the DAC domain of CdaA and DisA had let to the assumption that CdaA likely needs to dimerize to fulfill its catalytic function, but this first crystal structure only represented an inactive back-to-back dimer. However, using constructs of different length, it could be shown that CdaA from *Listeria monocytogenes* forms a dimer *in vitro* as well as *in vivo* (Rosenberg *et al*, 2015). In the same study, it was also reported that CdaA requires the divalent cations Mn^{2+} or Co^{2+} for its activity, based on HPLC/MS results. These findings are in line with the experiments from Heidemann and co-workers who utilized a coralyne-based assay to determine the metal-ion specificity of *Lm*CdaA (Heidemann *et al*, 2019). Contrary to this, cyclase activity of DisA was only detected in the presence of Mg^{2+} ions (Witte *et al*, 2008). Furthermore, the protein DacM from *Mycoplasma ovipneumoniae*, which belongs to the family of CdaM diadenylate cyclases, was reported to exhibit activity in presence of Mg^{2+} using a LC-MS based assay (Hao *et al*., 2022). Unfortunately, no further experiments were carried out to determine if DacM also shows activity in presence of other divalent cations. It should also be mentioned that DacM can use both ATP and ADP as substrate (Hao *et al*, 2022b). The protein CdaM from *Mycoplasma pneumonia* showed activity in presence of either Mn^{2+}, Mg^{2+} or Co^{2+} metal ions in a coralyne based assay. Notably, the measured activity was highest in presence of Mg^{2+}. The same behavior could be observed for CdaM from *Mycobacterium tuberculosis* (Bai *et al*, 2012).

These differences in the metal ion specificity of different proteins within the family of DAC domain-containing proteins are astonishing, as the amino acid sequence of the DAC domains of DisA, CdaA, and CdaM is very similar (Blötz *et al*., 2017). Heidemann and co-workers further showed that even the specific amino acids, which are involved in the coordination of both the product c-di-AMP and the vital divalent metal ion in the active center, are nearly identical between DisA and CdaA (Heidemann *et al*, 2019). These findings underline that even if the

DAC domains from different diadenylate cyclase families are quite similar, the exact mechanism might differ. This behavior can even be observed within a single class of diadenylate cyclases: While CdaA from *Listeria monocytogenes* was reported to be active in presence of Mn^{2+}, less so in presence of Co^{2+}, and not at all in presence of Mg^{2+}, CdaA from *Staphylococcus aureus* exhibits activity with all three divalent cations (Heidemann *et al*, 2019; Tosi *et al*, 2019). CdaAs from *Streptococcus suis* and *Streptococcus mitis* were also reported to be active with either Mn^{2+}, Co^{2+} or Mg^{2+} (Du & Sun, 2015; Rørvik *et al*, 2020). On the contrary, CdaA from *Bacillus subtilis* was reported to only use Mn^{2+} as cofactor (Pathania *et al*, 2021). Notably, the metal ion preference in each organism was determined using different assays. While a coralyne-based assay was used for *Listeria monocytogenes* CdaA, an MS-based approach was used for *Streptococcus suis* and *Streptococcus mitis* CdaAs. The activity for *Bacillus subtilis* CdaA and *Staphylococcus aureus* CdaA was determined using a TLC-based approach in combination with radioactively labelled ATP. Therefore, it cannot be precluded that the specific methods used to measure activity might have influenced the differential results obtained for various metal ions.

As these differences among organisms could possibly influence the broader efficiency of a possible inhibitor, truncated constructs of CdaA from *Listeria monocytogenes*, *Staphylococcus aureus*, *Enterococcus faecium*, *Bacillus subtilis* and *Streptococcus pneumoniae* were purified and treated with EDTA to ensure that all divalent cations were removed. Each purified protein was then applied to the coralyne assay. The activities of *Listeria monocytogenes* CdaA and *Bacillus substilis* CdaA were consistent with the metal ion specificity reported previously (Fig 3.3) (Heidemann *et al*, 2019; Pathania *et al*, 2021). *Enterococcus faecium* CdaA only showed activity in the presence of Mn^{2+} (Fig. 3.3). The *Streptococcus pneumoniae* CdaA exhibited activity in the presence of either Mn^{2+}, Co^{2+} or Mg^{2+}, which is in line with previous experiments performed with *Streptococcus pneumonia* CdaA (Fig. 3.3) (Rørvik *et al*, 2020; Du & Sun, 2015). Astonishingly, *Staphylococcus aureus* CdaA only exhibited activity in the presence of Mn^{2+} (Fig. 3.3). This is in clear discrepancy to the findings of Tosi and co-workers, who reported activity in the presence of other divalent metal ions (Tosi *et al*, 2019). These unexpected findings might origin from differences in the purification protocols, length of the used constructs and assays used to determine the cyclase activity. It might be worthwhile to repeat the TLC-based assay which was carried out by Tosi and co-workers with protein prepared according to the protocol of this work to clarify the metal ion specificity of *Staphylococcus aureus* CdaA. Another strategy would be to purify the CdaA from a different member of the *Staphylococcus* genus, as previous results from *Streptococcus* suggest that the metal-ion specificity might be conserved within a genus.

To gain more insights into the metal ion specificity, all five CdaAs purified in this work were used to carry out crystallization experiments. Therefore, each protein was mixed with ATP and its favored metal-ion and incubated at 37°C for 1 h before the sample was applied to the crystallization screen. For CdaA from *Streptococcus pneumoniae* and *Enterococcus faecium,* these crystallization trials were successful, and the respective CdaAs were crystallized in their

post-catalytic state, bound to the product c-di-AMP and the added metal-ion (section 3.2.1 and 3.2.2). Interestingly, *Streptococcus pneumoniae* CdaA crystallized as an inactive back-to-back dimer in the asymmetric unit. While one of the protomers did not have any nucleotide bound, the other protomer featured bound AMP (Fig. S.4). Careful inspection of the crystal packing revealed that the protomer forms an active dimer with a symmetry mate, sandwiching the product c-di-AMP in their interface. The same packing was already observed for the *Listeria monocytogenes* CdaA in complex with c-di-AMP (Heidemann *et al*, 2019). However, *Sp*CdaA crystallized in the tetragonal space group $P4_12_12$, while *Listeria monocytogenes* CdaA reportedly crystalized in the triagonal space group H32. It seems that this specific kind of forming the active center with a symmetry mate is favored by CdaA, which might be influenced by the inactive back-to-back dimer, which is also stable in solution (Tosi *et al*, 2019). Unfortunately, the post catalytic state of *Streptococcus pneumoniae* CdaA gave no further insights regarding the metal ion preference of this protein, as the metal ion itself is no longer coordinated strong enough to ensure catalytical activity (Fig. 3.6).

The CdaA from *Enterococcus faecium* crystalized in the monoclinic space group P2. The asymmetric unit consists of 10 CdaA protomers, which form 5 active dimers in total. Interestingly, every protomer is involved in the formation of an active dimer as well as in the formation of a back-to-back dimer. Nevertheless, the formation of *Enterococcus faecium* CdaA in a post catalytic state gave no further insights into its metal ion specificity, as the metal ion (Mn^{2+}) is not properly coordinated. The post catalytic state represented in this crystal structure can be identified by the re-established π-π interaction between the catalytic tyrosine at position 224 and the adenine moiety of the product c-di-AMP. This interaction does not occur during the reaction, as stated by Heidemann and co-workers (Heidemann *et al*, 2019). To gain more insights into the exact reaction mechanism, it would be necessary to trap the enzyme in its active state. A suitable strategy for this would be co-crystallization with the non-hydrolysable ATP derivates AMPCPP or Cordycepin triphosphate, however, previous crystallization experiments lead to only *Staphylococcus aureus* CdaA monomers bound to AMPCPP and Mn^{2+}, where the metal ion is only coordinated by the AMPCPP (PDB-ID: 6GYW) (Tosi *et al*, 2019). Furthermore, crystallization experiments with a mixture of ATP and a non-hydrolysable derivate could also be performed as it might lead to a trapped intermediate state. This could give insights into the exact reaction mechanism which is still being discussed for CdaA (Manikandan *et al*, 2014; Müller *et al*, 2015).

4.2 Oligomerization state of CdaA and its relevance

The first structure of a protein with a DAC domain was published by Witte and co-workers in 2008 (Witte *et al*, 2008). Structural analysis and *in vitro* experiments revealed that DisA forms stable octamers, where the protomers orient their active sites in a face-to-face manner. Comparisons of the active site carried out by Heidemann and co-workers revealed that the active site of CdaA is more crowded compared to DisA., As it needs to disassemble in order to

release the product c-di-AMP the active complex of CdaA is formed just transiently (Heidemann *et al*, 2019).

In 2015, Rosenberg and co-workers carried out *in vitro* SEC-MALS and crosslinking experiments with CdaA from *Listeria monocytogenes* (Rosenberg *et al*, 2015). The data suggested that CdaA forms a dimer in solution, but it was not confirmed if the dimer consists of the active head-to-head or the inactive back-to-back form. Furthermore, the dimeric state of an N-terminal truncated CdaA from *Staphylococcus aureus* was proven by SAXS (Tosi *et al*, 2019). Similarly, the radii of all the CdaA proteins purified for this work suggest and determined by DLS the assembly of a dimer in solution (Fig. 3.2). Nevertheless, the question remains whether the observed dimer in solution is the head-to-head or the inactive back-to-back conformer.

The CdaA dimer of *Staphylococcus aureus* appears particularly stable in solution as the introduction of disruptive mutations hardly affected oligomerization (Tosi *et al*, 2019). This observation is in contrast to the observed transient post catalytic state of *Listeria monocytogenes* CdaA (PDB-ID:6HVL), *Enterococcus faecium* CdaA and *Streptococcus pneumoniae* CdaA (section 3.2.1 and 3.2.2)). An alternative, non-head-to-head dimer assembly could also be observed in another class of DAC proteins, CdaS. Experiments with CdaS from *Bacillus subtilis* and *Bacillus thuringiensis* confirmed the formation of a hexamer in solution, which is in line with the crystal structure of CdaS from *Bacillus cereus* (PDB-ID:2FB5)(Mehne *et al*, 2014; Zheng *et al*, 2015). Unfortunately, it has never been shown if this hexameric state is the active state of CdaS or if further oligomerization is required. In contrast, biochemical and crystallographic data on the protein DisA prove that it forms a stable octamer in solution, which is also its active form (Müller *et al*, 2015; Witte *et al*, 2008). Hence, it was suggested by Tosi and co-workers that CdaA forms an inactive back-to-back dimer in solution, which needs to further oligomerize in order to fulfill its catalytic activity.

The various crystal structures of CdaA from different organisms, both those previously deposited in the PDB as well as those obtained in this work (section 3.2.1, 3.2.3 and 3.2.4), suggest the formation of an inactive back-to-back dimer. Analysis of the inactive dimers identified in the asymmetric units showed that each active site faces outwards and that the protomers are rotated by 45°. The interaction interface is also conserved in all structures as it is formed by the α-helix 2, the β-strand 2 and their corresponding partners from the other protomer (Fig. 1.4B). Moreover, this formation can be observed in both different crystallographic space groups and also for CdaA from different organism like *Staphylococcus aureus, Listeria monocytogenes*, *Streptococcus mutans, Streptococcus pneumoniae*, *Bacillus subtilis* and *Enterococcus faecium*. Analysis of the complexes of various organisms using *PDBePisa* revealed that a minimum of 9 hydrogen bonds is formed between the two protomers. Moreover, the calculated CSS scores, which indicate stability of the dimer, extend from 0.57 to 1, suggesting that this complex type is not a crystallographic artefact. Interestingly, the interaction area of both protomers is of similar size in each organism

(739-755Å^2), which can be interpreted as a further sign for the conservation of this interaction. The exact values are listed below in table 4.1.

Table 4.1: Results of *PDBePISA* analysis of the CdaA back-to-back dimer interaction. Structures without PDB-ID were structurally characterized in this work (section 3.2.1, 3.2.3, 3.2.4)

	*Lm*CdaA	*Sa*CdaA	*Sm*CdaA	*Bsu*CdaA	*Sp*CdaA	*Ef*CdaA
PDB-ID	6HVM	6GYW	7L8N	-	-	-
CSS-Score	0.61	1	1	0.57	0.75	1
Interface area [Å^2]	739.6	735.2	745.2	745.2	754.3	753.3
% from total area	9.3	9.5	10.0	9.3	9.6	9.9
Salvation energy [kcal/mol]	-6.0	-4.3	-4.2	-6.1	-5.0	-4.8
Hydrogen bonds	10	12	10	9	14	10
Salt bridges	0	2	2	0	3	2

In summary, the inactive back-to-back dimer of CdaA has been observed in several different crystallization systems and organisms. Consequently, Tosi and co-workers have speculated that CdaA might also form higher oligomerization states in order to form a functional diadenylate cyclase. Such higher oligomerization states upon enzymatic activity could be observed in the structure of *Listeria monocytogenes* CdaA (PDB-ID:6HVM) as well as the structures of *Enterococcus faecium* CdaA and *Streptococcus pneumoniae* in complex with c-di-AMP described in this work (section 3.2.1 and 3.2.2). All of this *in vitro* and crystallographic data suggests that the inactive back-to-back dimer formation is not an artefact, but appears to be conserved.

This raises the question whether the full length CdaA also forms these kinds of dimers *in vivo*. Tosi and co-workers had previously introduced mutations into *Staphylococcus aureus* CdaA which prohibit the formation of the back-to-back dimer, proven by SEC experiments. Moreover, they performed activity tests with this mutated CdaA, determining that the cyclase activity is nearly abolished (Tosi *et al*, 2019). However, although the mutant protein eluted at the same volume in SEC experiments as in the wild type, TSA experiments indicated that the protein was largely unfolded. Therefore, it cannot be stated with certainty whether the reduction of the cyclase activity of the mutated CdaA derives from the improper folding or the inability to form stable back-to-back dimers. To survey the folding state of the mutated protein, it would thus be useful to carry out further experiments like circular dichroism (CD). In 2021, the structure of GlmM from *Bacillus subtilis* was published (PDB-ID: 7OLM) (Pathania *et al*, 2021). This protein is known to inhibit the cyclase activity of CdaA by direct interaction and to occur in a shared gene cluster with CdaA and CdaR (Gibhardt *et al*, 2020; Gundlach *et al*, 2015). Furthermore, Pathania and co-workers were able to crystallize a GlmM dimer in complex with a CdaA dimer (PDB-ID: 7OLH). Analysis of the CdaA dimer showed that it also exhibits the inactive back-to-back conformation. The GlmM dimers revealed a U-shaped

arrangement with the CdaA dimer placed in the middle as depicted in Figure 4.1. This packing does not allow for any of the CdaA protomers to form a catalytically active dimer. Further analysis with PDBePisa suggests that both CdaA protomers are involved in interactions with GlmM indicating that the interaction of the back-to-back dimer is inevitable to from a stable quaternary complex (Pathania *et al*, 2021). These findings add to the ample evidence that that the previously observed back-to-back CdaA dimer is not an artefact but necessary for its regulation *in vivo*.

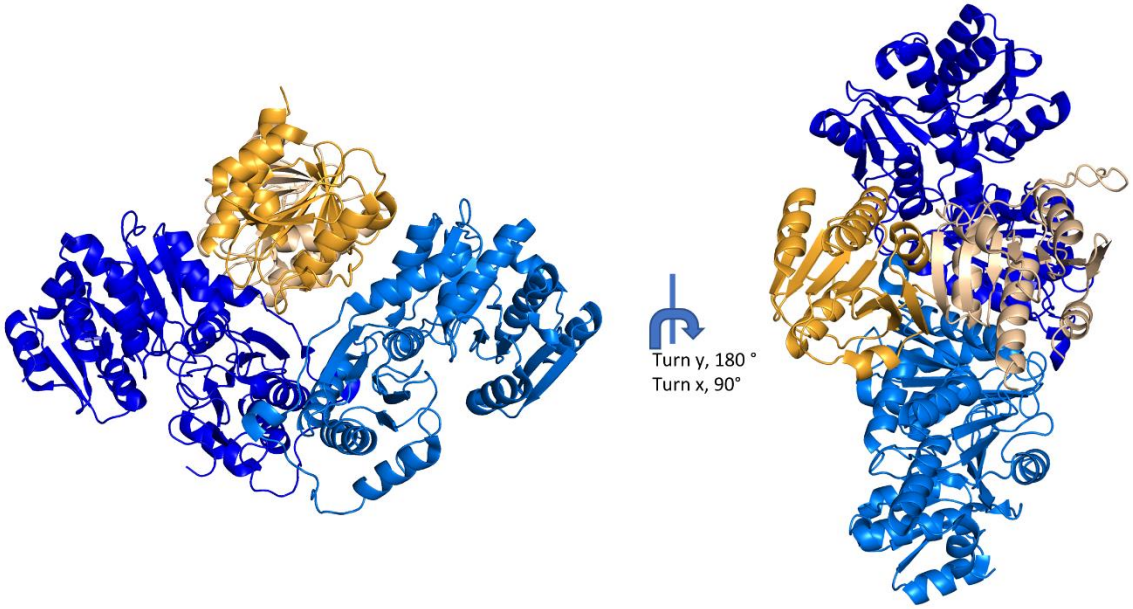

Figure 4.1: Presentation of the structure of *Bacillus subtilis* GlmM in complex with *Bacillus subtilis* CdaA. All molecules are depicted in the *cartoon* mode. The GlmM molecules are depicted in marine and blue, the CdaA protomers, which form a back-to-back dimer are colored in orange and wheat.

The next question which needs to be considered is if both protomers of a back-to-back dimer could be involved in the constitution of an active dimer. For *Listeria monocytogenes* CdaA, the engagement of one of the two protomers in an active complex could be observed, while the other protomer bound AMP (Heidemann *et al*, 2019). This finding already suggests that the second protomer is likely able to also bind the substrate ATP, as the molecular interactions with ATP and AMP are nearly identical. Additionally, the *Enterococcus faecium* CdaA was crystallized in in complex with c-di-AMP in this work (section 3.2.2). Here it can be observed that each protomer is involved in the formation of an active head-to-head as well as an inactive back-to-back dimer (Fig. S.3). Hence, it can be concluded that both protomers of the inactive dimer can be simultaneously engaged in an active dimer. Nevertheless, taking into account that CdaA is a membrane-bound protein with a linker of only approximately 20 amino acids located in between the DAC domain and the transmembrane helices, the formation of an oligomer consisting of more than four CdaA molecules is not very likely. As depicted in Figure S3, the CdaA molecules in the crystal structure arrange in a helical-like structure, in which each winding is comprised of three back-to-back dimers. The Figure 4.2A displays a

back-to-back dimer (blue and marine), which are both involved in the formation of an active dimer. Therefore, the N- and C-terminal ends of one of the molecules will not point towards the membrane of the cell, which contradicts its membrane bound form found *in vivo*.

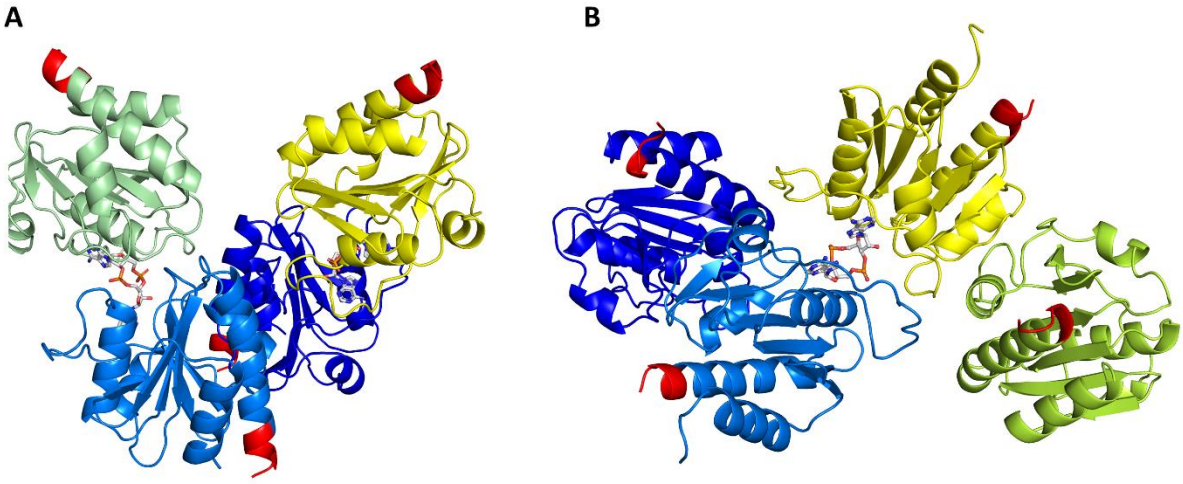

Figure 4.2: Presentation of CdaA in its active form bound to c-di-AMP. The first five N-terminally located amino acids of each molecule are colored in red. C-di-AMP is depicted as *sticks* (C-atoms in grey, phosphate in orange, oxygen in red and nitrogen in blue.) **A** represents the structure of four *Enterococcus faecium* CdaA molecules, presented as *cartoon*. The protomers engaged in a back-to-dimer are colored in blue and marine, the two monomers each forming an active center with one of the back-to-back dimers are colored in pale green and yellow. **B** represents the structure of four *Streptococcus pneumoniae* CdaA molecules, presented as *cartoon*. The protomers colored in blue and marine, as well as lime and yellow each form a back-to-back dimer. The CdaA molecules in marine and yellow also form an active dimer, sandwiching between them a c-di-AMP molecule.

Recapitulatory, it is most likely that the inactive back-to-back formation found in several crystal structures of CdaA from different organisms is the dimerization state in solution. Furthermore, the finding indicates that this dimer form could also occur *in vivo*. Nevertheless, higher oligomerization forms like hexa- or octamers which were observed for CdaS or DisA are not likely for CdaA, as this conflicts with its membrane bound state. Hence, the active form of CdaA is most likely a tetrameric state, which forms the transient active center, as indicated in Figure 4.2B.

4.3 A rational structural-based approach for the identification of an inhibitor for CdaA

Today, rising antibiotic resistance is one of the major health issues, causing around 700.000 deaths annually. This number is expected to rise to 10 million in 2050 if there will be no major paradigm shift in the usage and development of new strategies to reduce or prohibit the development of antimicrobial resistance (WHO, 2019). Unfortunately, since the beginning of the Covid-19 pandemic in early 2020, efforts gained to push back rising antibiotic resistance were nullified by improper and self-dosage of antibiotics (Khoshbakht *et al*, 2022). Hence,

there is an urgent need in the development of new antibiotics to gain the upper hand in the fight against multi-resistant bacteria. One possible target are enzymes which can produce c-di-AMP. This second messenger nucleotide is essential in bacteria in which this metabolite is found due to its regulatory role in osmolyte homeostasis (Bai *et al*, 2012; Gundlach *et al*, 2017a). It also plays a major role in modulating the virulence in several bacteria (Zarrella *et al*, 2020; Kundra *et al*, 2021) . Moreover, human pathogenic firmicutes often possess only a single protein which is capable to produce c-di-AMP, rendering this enzyme an ideal new target for the development of new antibiotics (Commichau *et al*, 2019).

A commonly used strategy to identify a new inhibitor of a specific protein is rational drug design starting from a structure of the protein bound to its substrate or product. This approach is frequently used in the development of inhibitors for proteases (Wang *et al*, 2019; Chan *et al*, 2022). Moreover, it was also successfully used for designing inhibitors of other enzymes like homoisocitrate dehydrogenase or hydroxysteroid dehydrogenase (Qiu *et al*, 2007; Wang *et al*, 2019). The examples for potent inhibitors deriving from ATP are less prominent, but there are a few examples (Toledo *et al*, 1999; Olivieri *et al*, 2022; Alexandrova *et al*, 2022). Unsurprisingly, the majority of these inhibitors are designed for protein kinases and are commonly used in cancer therapy (Bhullar *et al*, 2018; Gagic *et al*, 2020; Le *et al*, 2020). Recently, there have been several approaches to screen kinase inhibitors for possible antimicrobial effects (Schaenzer *et al*, 2017; Miller *et al*, 2009; Walsh & Fischbach, 2009). These experiments were carried out mostly in cell cultures, so while an antimicrobial effect was detected for some substances, the underlying mechanisms remain unclear (Johnston *et al*, 2016; King & Blackledge, 2021). Furthermore, kinase inhibitors often showed cooperative effects with other antibiotics, which in practice could make resistant bacteria more susceptible to commonly used antibiotics like Gentamycin or Methicillin (Vornhagen *et al*, 2015; Johnston *et al*, 2016). A recent success story is the antimicrobial compound PK150 from the company Merck. Here, a library of kinase inhibitors was used to screen for compounds with an antimicrobial effect and the anticancer drug sorafenib was identified as a hit able to efficiently kill MRSA strains. Thereafter, Merck synthesized 70 different compounds based on the structure of sorafenib and identified the compound PK150 as an antimicrobial compound with a 10-fold higher efficiency than the origin compound, equally powerful as the antibiotic Vancomycin (Le *et al*, 2020). In general, using a kinase inhibitor as starting point for drug repurposing is becoming a common strategy (Pereira Moreira *et al*, 2022; Gelmedin *et al*, 2015)

In this thesis, rational drug design using the structure of a protein-substrate complex led to the identification of a kinase inhibitor as suitable lead compound. The structure of *Bacillus subtilis* CdaA in complex with AMP was used to investigate the active-site interaction of AMP with the enzyme. Furthermore, the program *SeeSar* was employed to perform docking experiments and to assess the importance of single atoms of the ligand with respect to the interaction. This approach led to the identification of 7H-pyrrolo-[2,3-d]-

pyrimidine, which should bind within the same affinity range as AMP. The predicted binding mode was then confirmed experimentally by X-ray crystallography. Using the substructure search of two databanks in combination with *SeeSar* led to the identification of the two FDA/EMA approved tyrosine kinase inhibitors Ruxolitinib and Barcitinib as potential inhibitors for CdaA, which both exhibited a predicted binding affinity in the micromolar range (Fig. 3.25). Analysis of *Bacillus subtilis* CdaA crystals soaked with Barcitinib or Ruxolitinib revealed that only the latter one was successfully soaked into the crystal while no additional electron density was observed in crystals soaked with Barcitinib. The reason for this could be that Baricitinib does not actually bind to the *Bacillus subtilis* CdaA. However, other factors like unfavorable charges or the size of the solvent channels within the crystal system might have prevented soaking with Barcitinib to be successful. Therefore, while it cannot be stated with certainty that Barcitinib does not interact with CdaA, further experiments were carried out using Ruxolitinib, as the structural evidence suggested more strongly that it could inhibit CdaA. Indeed, *in vitro* assays utilizing the coralyne assays in combination with *Bacillus subtilis* CdaA showed that Ruxolitinib reduces the cyclase activity with an IC_{50} value of 2.7 µM (Fig. 28). To investigate if these findings are unique to *Bacillus subtilis* CdaA or can also be observed with other CdaAs from pathogenic organisms, Ruxolitinib was soaked into APO crystals of *Lm*CdaA (section 3.4.3). Moreover, the coralyne assay was used to investigate inhibitory effects of Ruxolitinib against the CdaAs from *Enterococcus faecium, Listeria monocytogenes, Streptococcus pneumoniae* and *Staphylococcus aureus* (Fig. 29). The results of these experiments indicate that binding, and also the reduction of the cyclase activity of CdaA by Ruxolitinib, is indeed conserved among different organisms.

To put this into context, it would be insightful to carry out similar experiments with the published CdaA inhibitors Bromophenol-Thiohydantoin (Br-TH) and IPA-3 (Chen *et al*., 2018; Li *et al*., 2022). While IPA-3 was identified using a kinase inhibitor library, bromophenol derivatives are also known for their inhibitory effects on kinases (Wang *et al*, 2015). Br-TH's function as an inhibitor of diadenylate cyclases was discovered by Sintim and collegues (Zheng *et al*, 2014). The inhibitory effect of Br-TH towards CdaA was determined using a coralyne *in vitro* and an *in vivo* assay with *Enterococcus faecalis* and its respective CdaA. The *in vitro* experiments showed that Br-TH can completely abolish the cyclase activity of *Enterococcus faecalis* CdaA at a concentration of 90 µM. Unfortunately, no IC_{50} value was determined. It should also be kept in mind that no control experiments were carried out and therefore it cannot be ruled out that coralyne is directly quenched by the halogen group of Br-TH, as it was also shown to be the case in this thesis for the fragment D02. Nevertheless, they also showed that Br-TH has antimicrobial effects against *Enterococcus faecalis,* as this compound, applied with a concentration of 180 µM, is able to reduce the biofilm formation of this bacteria by approximately 80% (Chen *et al*., 2018).

The compound 2,2´dihydroxy-1,1´dinapthyldisulfide (IPA-3) was identified as an inhibitory compound by combining an assay based on the reagent Kinase Glo with a kinase inhibitory library and an N-terminally truncated CdaA construct from *Streptococcus suis*. The suppressing

activity of IPA-3 against the *Streptococcus suis* CdaA was further verified by HPLC experiments. Furthermore, an IC_{50} value of 33.22 µM was determined. To also investigate the inhibitory effect of IPA-3 *in vivo*, bacterial growth experiments were performed. *Escherichia coli* cells were used as a negative control, as this organism possesses no enzyme harboring a DAC domain. In addition, the effect of IPA-3 on the bacteria strains *Streptococcus suis, Bacillus subtilis, Staphylococcus aureus, Streptococcus mutans* and *Enterococcus rhusiopahiae* were tested. Notably, *Escherichia coli* and *Streptococcus mutans* growth was not or just slightly reduced by the compound IPA-3, which is in line with *E. coli* not possessing any diadenylate cyclase activity and with c-di-AMP shown to not being essential in *Streptococcus mutans* (Cheng *et al*, 2016). Surprisingly, IPA-3 was able to abolish the growth of *Bacillus subtilis* cells, which possess three different proteins harboring a DAC domain. This indicates that IPA-3 is not only active against CdaA, but also against other diadenylate cylases like DisA or CdaS. To test if Ruxolitinib is similar or whether it specifically inhibits CdaA, *in vivo* growth experiments with *Escherichia coli* and different deletion strains of *Bacillus subtilis* were carried out (Fig. 31). These experiments showed that Ruxolitinib is able to reduce the growth rate of the ΔdisA ΔcdaS and WT strain, but not the growth of the ΔcdaA ΔcdaS or *Escherichia coli* strain, suggesting that Ruxolitinib is indeed a specific inhibitor of CdaA *in vivo* (section 3.4.6). Therefore, Ruxolitinib is the first compound whose inhibitory effect and specificity against CdaA has been proven *in vivo*.

Besides the inhibitory effect, important aspects that determine whether or not an inhibitory compound can be further developed into a drug candidate are potential permeability issues, easy metabolization, low bioavaibility or tolerance (McMartin, 1991). For the compound Br-TH and the diadenylate cyclase DisA, experiments using the structure-activity-relationship (SAR) approach were carried out. Nineteen different compounds deriving from Br-TH were synthesized and tested in the coralyne assay. Nevertheless, no compound with an increased inhibitory effect compared to Br-TH could be identified (Zheng *et al*, 2016). These efforts show that the improvement of a compound without any structural information is a herculean task. IPA-3 is regarded as a drug-like compound and its inhibitory effect as a kinase inhibitor against p21-activated kinase 1 has been proven *in vitro* and *in vivo*, rendering this compound as potential drug for the treatment of prostate cancer (Al-Azayzih *et al*, 2016; Ji *et al*, 2016). Unfortunately, experiments with human cells in combination with IPA-3 showed that this compound is toxic for human peripheral blood cells and is also poorly soluble in water (Kuželová *et al*, 2014). Taken the facts together, IPA-3 could serve as good starting point for the development of a potential inhibitor for CdaA. Nevertheless, the specificity against this protein must be ensured. Therefore, structural knowledge of the complex of IPA-3 and CdaA will be helpful to carry out SAR-analysis and to develop a more potent and specific inhibitor. The findings in this thesis on the kinase inhibitor Ruxolitinib render this compound an inhibitor for CdaA both *in vivo* and *in vitro* (section 3.4.4 and 3.4.6). Moreover, this compound is already approved by the FDA/EMA for the treatment of myelofibrosis and in a low-dosage treatment also for atopic dermatitis and vitiligo as it inhibits the janus kinases JAK1 and JAK2 (Sheikh *et*

al, 2022; Kim *et al*, 2020; Harrison *et al*, 2012). It must be considered that there is the need to change the structure of this compound in a way that it loses its inhibitory effect against targets in humans, but not towards CdaA. The structural information provided by the complex of *L. monocytogenes* and *Bacillus subtilis* CdaA with Ruxolitinib can be used as starting point for the development of a more powerful and specific inhibitor against CdaA (section 3.4.2 and 3.4.3).

4.4 Fragment Screen using *Bacillus subtilis* CdaA

Crystallographic fragment screening has become a powerful tool for the efficient development of new drugs (Patel *et al*, 2014). Although historically considered a slow method as every crystal needs to be measured individually and no parallelization is possible, recent developments regarding the synchrotron storage rings and beamline automatization enable the collection of thousands of datasets per week (Lima *et al*, 2020). The advantage of this method is that smaller and less complex chemical compounds (fragments) can be used compared to other methods (Hajduk & Greer, 2007). Due to their simpler structure, these fragments have a higher chance to bind to the target protein, resulting in more hits (Erlanson *et al*, 2004). To complement this approach, as these small fragments bind less strongly to the target protein than larger compounds, methods like PanDDA were development to also identify weakly bound hits (Pearce *et al*., 2017a). Moreover, these fragments need no further deconstruction and can be used directly as starting points for the development of potent and highly specific inhibitors (Foloppe, 2011).

The first step for the execution of a crystallographic fragment screen campaign (CFS) is the identification of a suitable target. The second step of a CFS campaign is establishing a suitable crystallization system of the target protein in its APO state, as the success of the campaign heavily depends on the average resolution and robustness of the crystals (Collins *et al*, 2018). In this thesis, the CdaA of five different organisms were truncated in a rational manner and applied to crystallization trials. N- and C-terminally truncated constructs from *Enterococcus faecium* and *Bacillus subtilis* could be crystallized in their respective APO state. Unfortunately, as the *Ef*CdaA crystals only appeared after 5 months and diffracted to only 2.8 Å resolution, they were not suitable for a CFS campaign (Wollenhaupt *et al*, 2021b). The crystals harvested from the *Bs*CdaA construct could be reliably reproduced and diffracted to between 1.1 and 1.5 Å. Regrettably, this means that solely the CdaA from the non-pathogenic organism *Bacillus subtilis* crystallized in a system satisfying the requirements for a CFS campaign, despite the similar truncations and final size of all constructs. Small differences could have led to the other constructs not crystallizing, like slightly different lengths of their N-and C-terminal helices (Fig. S.1).

For *Bacillus subtilis* CdaA, one magnesium ion is sandwiched between one protomer and a symmetry mate, coordinated by non-conserved amino acids (Fig. 3.11). If the crystallization conditions are set up without any magnesium, no crystals could be observed, indicating that

this coordination is essential for crystal packing. Moreover, the crystallization system was further optimized for a CFS campaign regarding its buffer composition as well as DMSO and salt concentrations (Collins *et al*, 2018). The DMSO concentration is of particularly high interest, as fragments are only soluble up to a concentration of 1 mM in a water-based solvent (Baybekov *et al*, 2021). Therefore, different crystallization and diffraction experiments were carried out, identifying 20% as ideal DMSO concentration for the crystallization condition (section 3.3.1). This high percentage of DMSO should lead to a higher solubility of the fragments and finally to a higher hit identification (Douangamath *et al*, 2021).

The CFS campaign was performed using the F2X-Entry fragment screen (Wollenhaupt *et al*, 2020). The hit-rate of the first FBDD derived drug Vemurafenib was drastically increased by pre-screening with an activity assay, leading to a hit rate of about 42% (Tsai *et al*, 2008). This rate is way higher than the normally expected hit rate of 0.5-10% in CFS campaigns (Verlinde *et al*, 2009). This rate is confirmed by the latest published CFS campaigns against targets from SARS-COV-2. Campaigns using NSP13 as their target reported a hit rate of 8%, those on NSP1 a hit rate of 5.8% and those on SARS-COV-2 main protease a hit rate of 0.6% (Günther *et al*, 2021; Newman *et al*, 2021; Ma *et al*, 2022). Here, we reported a hit rate of 33% of the F2X-Entry library against the protein *Bacillus subtilis* CdaA (section 3.3.2). This performance is above average, but in line with the previously published hit rate of about 20% (Wollenhaupt *et al*., 2021).

Analysis of these hits reduced the number to a total of 6 different fragments which can be used as starting points for the development of inhibitory lead compounds as they bind to a highly conserved region of CdaA (section 3.3.2). Unfortunately, none of the fragments show a strong inhibitory effect on the cyclase active of *Bacillus subtilis* CdaA in the employed assays (section 3.3.3). Three of the fragments are allocated in the same site where the adenine moiety of the substrate ATP is bound (A09, G04 and D02) (Fig. 3.15B). Therefore, it could be worth to grow these fragments in the direction where the other parts of the ATP are bound to further block the interaction of the enzyme with its substrate, or they can be merged by identifying a shared scaffold. Moreover, the fragments A09, G04 and D02 could be linked to the other 3 identified fragments (B07, B08, E04) to prohibit the formation of the active center of CdaA (Fig 3.15B). The fragment B07 seems to be the most promising fragment for this approach as is exhibits the highest occupancy in the respective X-ray structure (section 3.3.2)

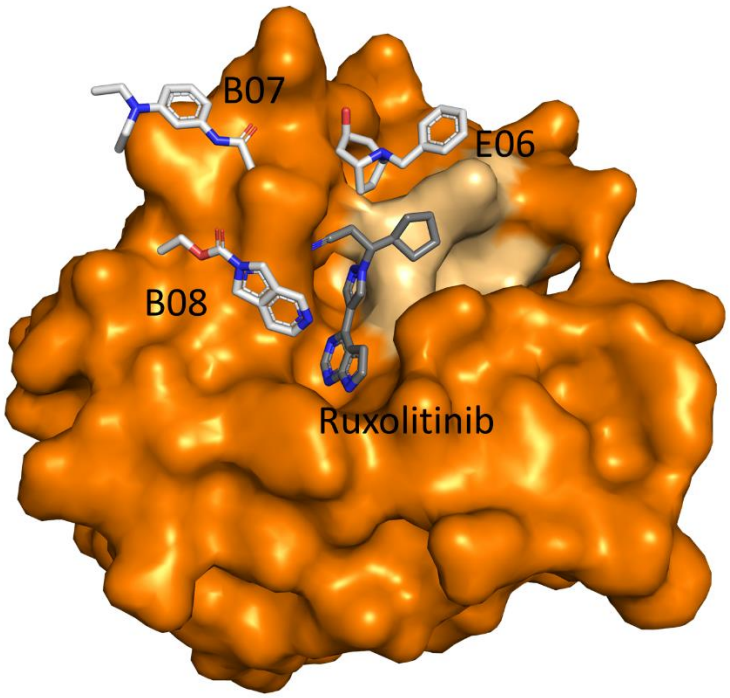

Figure 4.3: Presentation of *Bacillus subtilis* CdaA in complex with the fragments B07, B08, G04 and the compound Ruxolitinib. The structure of *Bacillus subtilis* CdaA is depicted as *surface* and colored in orange. The cleft which indicates a possible growth direction of Ruxolitinib is colored in wheat. The fragments and Ruxolitinib are depicted as *sticks* (carbon in grey or dark grey, oxygen in red and nitrogen in blue).

Similarly, Ruxolitinib, which was identified by rational drug design (section 3.4.2), could also be used as starting point for the development of a potential antibiotic drug as is able to reduce the activity of CdaA (section 3.4.4). One possibility to modify Ruxolitinib might be the introduction of a hydroxy group at the pyrazole-ring of this compound, as the structure showed that the nitrogen of the pyrazole ring coordinates a water molecule which is further coordinated by aspartate 171 and histidine 172, two heavily conserved residues (Fig. 3.26 B). This introduction of a hydroxy group based on the observed coordination of a water molecule was previously successfully performed for the development of an HIV protease inhibitor (Yue *et al*, 1987; Fischer & Riedl, 2013). The structure of *Bs*CdaA with Ruxolitinib aligned with the identified fragments shows that Ruxolitinib covers the space where the fragments A09, G04 and D02 are located, as they all bind in the active center, unlike B07, E06 and B08 (Fig. 3.15B). Therefore, it is also possible to link Ruxolitinib with one of the latter fragments via a suitable linker to achieve a more potent and specific inhibitor for CdaA. Moreover, the cycloheptane moiety of Ruxolitinib could be used as a starting point to grow this compound further in the direction of the conserved cleft of CdaA to raise the specificity towards CdaA as depicted in Figure 4.3.

5 Summary

One of the major threats for the global health system is the increasing number of antibiotic resistant bacterial strains. The misuse of antibiotics during the Covid pandemic aggravates these problems. Therefore, the development of new antibiotics is mandatory to fight the rising threat of multi-resistant bacteria.

The essential second messenger c-di-AMP was discovered in 2008 and is mainly found in gram positive bacteria. It has been identified in several human pathogens like *Listeria monocytogenes*, *Staphylococcus aureus* or *Enterococcus faecalis.* It is a key player in the regulation of several pathways like DNA integrity scanning, cell wall metabolism or osmolyte homeostasis. Five different protein classes are able to synthesize c-di-AMP They all have the diadenylate cyclase domain (DAC) in common and need to dimerize to produce c-di-AMP in a metal-ion dependent manner from two ATP molecules. The protein class CdaA consists of three N-terminal transmembrane helices followed by the DAC domain and is often the sole diadenylate cyclase in several human pathogenic bacteria like *Staphylococcus aureus, Streptococcus pneumoniae* or *Enterococcus faecium.* The essentiality of c-di-AMP renders CdaA as potential target for the development novel antibiotic substances.

The major goal of this thesis was the establishment of a crystallization system of CdaA suitable for a fragment screening campaign in order to identify starting points for the development of inhibitors of CdaA. Therefore, the first part of this work is focused on the crystallization of CdaA from the soil bacterium *Bacillus subtilis* and the human pathogens *Listeria monocytogenes, Staphylococcus aureus, Streptococcus pneumoniae* and *Enterococcus faecium*. To obtain constructs well suited for crystallography, the CdaAs of these organisms were N- and C-terminal truncated to solely consist of the DAC domain. The purity and homogeneity of every purified CdaA were verified via SDS-PAGE and DLS. To prove the enzymatic functionality of the purified proteins, the coralyne activity assay was applied with varying divalent cations. All purified CdaAs exhibit activity in the presence of manganese ions while their activity in presence of magnesium- or cobalt-ions differs. To explore these variations, crystallization trials of the different CdaAs in presence of their favorable metal-ion and ATP were carried out.

As a result, the crystal structure of *Enterococcus faecium* CdaA in complex with c-di-AMP and manganese as well as the crystal structure of *Streptococcus pneumoniae* CdaA in complex with c-di-AMP and magnesium were solved at a resolution of 2.1 Å (*Ef*CdaA) and 2.2 Å (*Sp*CdaA). Unfortunately, both models represent a post catalytic state where the metal ion is not coordinated in a catalytically active way, giving no further insights into the structural basis for the differing metal ion specificity. Nevertheless, if both obtained structures are compared to the *Listeria monocytogenes* CdaA structure in complex with c-di-AMPa conserved interaction pattern with c-di-AMP could be observed, rendering the interacting amino acids as possible targets for inhibitor design.

In order to identify potential fragments which can reduce the activity of CdaA, the CdaAs from all previously mentioned organisms were applied to crystallization trials in their APO state. For the CdaA of *Enterococcus faecium* and *Bacillus subtilis* these trials were successful. However, the crystallization system for *Enterococcus faecium* CdaA does not matches the requirements for a crystallographic fragment screening campaign as the crystals diffracted just to 2.4 Å and required several months to grow. In contrast, the *Bacillus subtilis* APO crystals diffracted up to 1.6 Å and were highly reproduceable. Further optimization of the crystallization condition led to a crystallization system which is greatly suitable for a fragment screening campaign. Through the following fragment campaign using the F2X-Entry screen, 32 unique fragments were identified to interact with *Bs*CdaA. Mapping these fragments on a *Consurf* model of CdaA reduced the number to six different fragments which bound in the highly conserved active/dimerization site. These fragments were also biochemically characterized using the coralyne and malachite green assay. As none of the fragments reduced the cyclase activity of *Bs*CdaA, an alternative approach was carried out to identify an inhibitory compound.

Here, the structure of *Bs*CdaA in complex with AMP, which were determined in this work served as starting point for the identification of an inhibitory compound. By a computational defragmentation approach employing *SeeSar,* adenine was identified as fragment of AMP which is largely responsible for the biding capability of AMP. Combing the methods of computer aided drug design and structural information gained by X-ray crystallography, the Janus kinase inhibitor Ruxolitinib was identified as potential inhibitory compound for CdaA. The conserved binding mode of Ruxolitinib towards CdaA was proven as Ruxolitinib exhibits the same interaction pattern for CdaA from *Bacillus subtilis* and *Listeria monocytogenes* as it can be concluded by the X-ray structures obtained in this work as Ruxolitinib binds in the active site of the protein, it most likely acts as competitive inhibitor for CdaA. Moreover, the IC_{50} value of Ruxolitinib was determined as 2.7 µM for *Bs*CdaA. Determining the cyclase activity of CdaA from *Listeria monocytogenes, Staphylococcus aureus, Streptococcus pneumoniae* or *Enterococcus faecium* in presence of Ruxolitinib also show a reduced activity, underlining the conservation of the protein-ligand interaction. Besides the *in vitro* studies, also *in vivo* experiments utilizing different *Bacillus subtilis* strains were carried out. The results from these experiments suggest a high specificity of Ruxolitinib towards *Bacillus subtilis* CdaA *in vivo*.

6 Appendix

Table S.1: Overview of collected datasets for the crystallographic fragment screen.

Name	High resolution [Å]	Low res[Å]	R_{work}[%]	R_{free}[%]	comp_ overall	comp_high	overall I/σ (I)	high I/σ (I)	overall CC1/2	high CC1/2	fragment
A01a	1,32	33,93	0,20	0,24	95,0%	91,9%	10,5	0,6	99.9*	37.9*	
A01b	1,29	46,87	0,19	0,22	95,8%	94,1%	9,1	0,5	99.9*	31.9*	
A02a	1,27	42,68	0,21	0,23	92,3%	90,2%	11,2	0,7	99.9*	42.4*	
A02b	1,29	33,98	0,18	0,22	92,7%	90,2%	11,9	0,6	99.9*	38.1*	
A03a	1,24	46,81	0,19	0,20	97,1%	94,3%	12,5	0,7	99.9*	47.6*	
A03b	1,14	46,86	0,19	0,21	92,3%	66,0%	13,0	0,5	99.9*	30.7*	
A04a	1,24	46,84	0,19	0,22	95,8%	92,7%	11,8	0,8	99.9*	65.4*	
A04b	1,3	37,27	0,21	0,23	98,6%	97,1%	9,3	0,5	99.8*	31.4*	
A05a	1,35	42,65	0,18	0,23	96,9%	94,8%	11,1	0,8	99.9*	40.0*	
A05b	1,29	46,78	0,20	0,23	97,4%	94,6%	10,3	0,6	99.9*	38.8*	
A06a	1,5	33,81	0,20	0,22	95,8%	90,7%	10,6	1,0	99.8*	46.3*	
A06b	1,42	42,63	0,21	0,24	92,9%	92,5%	9,9	0,7	99.9*	42.8*	
A07a	1,48	32,96	0,21	0,24	95,7%	92,4%	10,1	0,9	99.8*	44.9*	
A07b	1,21	46,9	0,20	0,23	98,5%	96,7%	11,6	0,7	99.9*	44.2*	
A08a	1,17	46,77	0,19	0,21	92,7%	74,0%	10,8	0,6	99.9*	38.5*	
A08b	1,3	46,98	0,20	0,23	96,4%	92,8%	10,0	0,7	99.9*	39.9*	
A09a	1,22	46,78	0,19	0,22	96,2%	93,8%	11,0	0,6	99.9*	41.2*	X
A09b	1,29	42,67	0,19	0,23	96,8%	91,8%	10,2	0,7	99.9*	39.2*	X
A10a	1,22	42,69	0,19	0,22	97,9%	95,5%	11,8	0,7	99.9*	44.9*	
A10b	1,35	33,9	0,18	0,22	94,6%	91,5%	12,3	0,8	99.9*	44.4*	
A11a	1,25	42,72	0,21	0,22	99,1%	98,3%	11,7	0,7	99.9*	46.2*	
A11b	1,17	46,9	0,20	0,22	89,8%	67,0%	10,9	0,6	99.9*	39.3*	
A12a	1,22	32,1	0,22	0,24	97,8%	94,6%	11,3	0,6	99.9*	40.3*	X
A12b	1,21	33,93	0,19	0,22	93,0%	87,2%	9,8	0,5	99.9*	39.5*	X
Apo01	1,28	42,68	0,20	0,22	97,1%	94,6%	11,2	0,6	99.9*	44.7*	
Apo02	1,21	33,98	0,22	0,24	97,2%	92,7%	10,2	0,6	99.9*	40.2*	
Apo03	1,27	46,9	0,22	0,24	93,8%	90,5%	10,1	0,5	99.9*	44.1*	
Apo04	1,48	42,64	0,23	0,25	96,8%	94,1%	9,6	0,8	99.9*	42.4*	
Apo06	1,61	46,83	0,21	0,25	98,6%	96,7%	9,2	0,7	99.8*	34.7*	
Apo07	1,68	32,05	0,21	0,25	98,1%	93,5%	7,2	0,7	99.7*	34.6*	
Apo08	1,46	37,28	0,18	0,22	98,0%	94,0%	11,2	1,2	99.8*	59.3*	
Apo09	1,23	31,85	0,19	0,22	93,3%	86,5%	10,1	0,6	99.9*	44.1*	
Apo10	1,3	34,04	0,22	0,24	94,6%	91,2%	9,9	0,5	99.9*	44.3*	
B01a	1,14	46,84	0,18	0,21	98,3%	95,6%	11,0	1,1	99.9*	61.6*	
B01b	1,56	46,83	0,21	0,23	83,6%	41,1%	13,3	0,6	99.9*	44.1*	
B02a	1,11	33,93	0,21	0,22	96,7%	94,5%	12,2	0,8	99.9*	45.7*	
B02b	1,36	46,77	0,20	0,22	86,3%	53,6%	13,0	0,6	99.9*	40.8*	
B03a	1,15	42,72	0,20	0,23	93,4%	88,2%	12,1	0,7	99.9*	47.9*	X
B03b	1,22	46,73	0,19	0,22	96,8%	92,7%	8,4	0,5	99.8*	37.7*	X
B04a	1,38	46,87	0,20	0,25	97,6%	94,6%	9,1	0,9	99.8*	50.2*	
B04b	1,55	46,83	0,22	0,24	98,5%	94,6%	8,1	0,7	99.8*	41.4*	
B05a	1,66	46,68	0,22	0,28	97,5%	93,7%	13,2	0,7	99.9*	42.0*	
B05b	1,35	46,81	0,21	0,23	98,0%	94,6%	8,8	0,9	99.7*	46.0*	

B06a	1,42	32,88	0,19	0,23	96,4%	95,0%	13,2	1,0	99.9*	56.1*	
B06b	1,41	46,79	0,18	0,22	97,8%	92,6%	10,7	0,6	99.9*	46.6*	X
B07a	1,35	46,96	0,22	0,24	97,6%	95,6%	11,1	0,9	99.9*	43.3*	X
B07b	1,5	42,73	0,21	0,25	94,9%	92,2%	9,0	0,6	99.9*	33.2*	
B08a	1,3	34	0,21	0,25	97,3%	93,6%	9,1	0,7	99.8*	36.4*	X
B08b	1,25	46,8	0,19	0,22	92,8%	87,9%	10,1	0,5	99.9*	46.7*	X
B09a	1,3	42,7	0,23	0,25	95,1%	91,8%	10,4	0,6	99.9*	46.6*	
B09b	1,22	42,63	0,22	0,22	98,6%	96,4%	10,1	0,8	99.8*	45.2*	
B10a	1,27	46,89	0,21	0,26	97,6%	90,9%	11,4	0,6	99.9*	40.0*	
B10b	1,42	47	0,20	0,23	98,9%	98,4%	11,2	0,9	99.9*	48.1*	
B11a	1,19	33,04	0,20	0,22	96,1%	92,1%	11,1	0,7	99.9*	49.4*	
B11b	1,4	46,9	0,18	0,23	94,3%	89,8%	11,6	0,6	100.0*	45.6*	
B12a	1,22	33,98	0,20	0,22	89,3%	59,3%	11,4	0,6	99.9*	38.1*	
B12b	1,22	46,85	0,19	0,22	98,5%	95,8%	9,7	0,7	99.9*	44.8*	
C01a	1,15	46,9	0,20	0,22	95,2%	90,8%	10,4	0,7	99.9*	46.3*	
C01b	1,4	42,62	0,20	0,24	93,0%	91,0%	9,7	0,6	99.9*	45.8*	
C02a	1,35	33,95	0,19	0,22	91,9%	65,4%	15,0	0,6	100.0*	34.5*	
C02b	1,46	46,68	0,21	0,25	96,1%	93,3%	12,8	0,7	99.9*	36.2*	
C03a	1,14	37,08	0,18	0,20	98,5%	96,6%	11,2	0,9	99.9*	43.8*	
C03b	1,32	46,85	0,19	0,22	95,6%	88,8%	9,3	0,6	99.9*	40.4*	
C04a	1,5	42,72	0,20	0,23	96,7%	95,2%	9,6	0,7	99.9*	44.9*	X
C04b	1,21	33,96	0,20	0,22	97,9%	95,2%	12,7	0,7	99.9*	43.4*	X
C05a	1,39	46,87	0,19	0,24	97,5%	93,8%	9,4	0,5	99.9*	35.8*	
C05b	1,25	46,96	0,19	0,22	84,1%	47,5%	13,3	0,6	100.0*	41.2*	
C06a	1,28	32,88	0,19	0,21	98,5%	97,2%	11,6	0,7	99.9*	40.9*	X
C06b	1,83	46,74	0,21	0,27	98,5%	96,2%	11,0	0,6	99.9*	42.6*	
C07a	1,41	42,68	0,19	0,22	92,0%	86,0%	12,6	0,6	100.0*	41.9*	X
C07b	1,28	33,91	0,21	0,24	97,4%	93,7%	10,3	0,8	99.8*	49.8*	X
C08a	1,25	42,67	0,20	0,22	96,7%	94,1%	13,1	1,0	99.9*	55.7*	X
C08b	1,35	47,04	0,21	0,23	96,7%	92,4%	10,0	0,6	99.9*	43.3*	X
C09a	1,25	42,68	0,18	0,21	88,1%	46,4%	14,3	0,5	99.9*	39.0*	
C09b	1,39	46,78	0,21	0,23	95,2%	93,1%	11,2	1,0	99.8*	47.1*	
C10a	1,32	30,81	0,21	0,24	97,0%	93,9%	9,8	0,8	99.9*	41.9*	
C10b	1,22	46,85	0,21	0,23	96,7%	93,6%	7,0	0,9	99.5*	39.2*	
C11a	1,32	42,71	0,21	0,23	97,7%	94,2%	9,3	1,0	99.8*	47.3*	X
C11b	1,42	46,85	0,22	0,24	98,1%	95,9%	9,1	0,6	99.9*	39.4*	X
C12a	1,22	33,05	0,20	0,23	98,2%	95,8%	11,1	0,7	99.9*	46.9*	
C12b	1,32	30,76	0,22	0,24	98,2%	95,9%	9,7	0,7	99.9*	39.9*	
D01a	1,23	46,76	0,21	0,23	95,1%	91,8%	9,9	0,7	99.9*	43.9*	
D01b	1,45	42,76	0,18	0,21	98,8%	98,1%	13,9	0,8	99.9*	42.3*	
D02a	1,15	42,69	0,19	0,21	93,5%	88,2%	9,6	0,5	99.9*	38.5*	X
D02b	1,21	46,82	0,19	0,22	94,4%	88,8%	10,2	0,5	99.9*	43.6*	X
D03a	1,31	33,95	0,19	0,21	97,7%	94,8%	9,6	0,6	99.9*	40.3*	
D03b	1,17	30,71	0,20	0,22	98,3%	96,4%	9,1	0,7	99.8*	33.4*	
D04a	1,23	42,68	0,19	0,23	96,3%	92,2%	11,0	0,6	99.9*	39.9*	X
D04b	1,25	46,82	0,20	0,24	94,7%	91,2%	9,9	0,6	99.9*	34.6*	X
D05a	1,29	46,91	0,20	0,23	97,1%	94,6%	15,7	1,3	99.9*	73.9*	
D05b	1,11	46,91	0,20	0,21	95,2%	92,2%	12,8	1,0	99.9*	45.2*	
D06a	1,14	42,73	0,20	0,22	91,9%	66,9%	13,9	0,6	100.0*	36.8*	X

D06b	1,18	46,83	0,22	0,25	95,5%	92,8%	12,8	0,7	99.9*	36.3*	X
D07a	1,27	37,25	0,19	0,22	90,8%	68,7%	13,3	0,6	100.0*	39.9*	
D07b	1,25	42,66	0,18	0,21	94,8%	90,8%	11,9	0,7	99.9*	46.8*	
D08a	1,22	46,91	0,19	0,23	94,4%	92,2%	11,1	0,6	99.9*	36.3*	X
D08b	1,27	42,74	0,19	0,22	95,7%	93,4%	10,4	0,6	99.9*	42.2*	X
D09a	1,14	42,66	0,19	0,21	91,2%	59,9%	10,9	0,4	99.9*	26.4*	
D09b	1,21	46,92	0,19	0,22	94,9%	75,6%	12,1	0,5	100.0*	32.4*	
D10a	1,28	33,9	0,19	0,22	89,7%	71,9%	9,6	0,6	99.9*	37.9*	
D10b	1,38	33,04	0,18	0,21	98,8%	97,8%	8,1	0,6	99.8*	32.9*	
D11a	1,21	46,81	0,18	0,21	95,6%	93,3%	9,8	0,8	99.9*	43.3*	
D11b	1,22	31,98	0,22	0,25	97,8%	95,6%	9,7	0,7	99.9*	46.0*	
D12a	1,08	46,88	0,17	0,19	98,0%	94,0%	10,8	0,6	99.9*	38.4*	
D12b	1,35	46,96	0,19	0,23	92,2%	66,5%	9,8	0,5	99.9*	33.9*	
E01a	1,08	33,96	0,20	0,22	94,8%	89,2%	12,3	0,7	99.9*	47.5*	
E01b	1,15	33,94	0,21	0,23	98,7%	96,5%	11,9	0,6	99.9*	35.5*	
E02a	1,52	46,65	0,21	0,23	96,6%	90,1%	11,8	0,7	99.9*	36.2*	
E02b	1,48	33,78	0,21	0,22	95,0%	90,2%	12,2	0,6	100.0*	46.3*	
E03a	1,19	30,67	0,21	0,23	87,3%	45,1%	13,7	0,7	99.9*	46.2*	
E03b	1,35	34,04	0,18	0,21	94,7%	91,4%	10,8	0,6	99.9*	36.1*	
E04a	1,22	46,88	0,20	0,23	79,5%	31,1%	11,0	0,7	99.9*	44.7*	X
E04b	1,14	33,97	0,21	0,22	89,0%	58,0%	12,7	0,6	99.9*	39.6*	
E05a	1,21	33,99	0,19	0,23	95,0%	92,4%	12,6	0,8	99.9*	36.5*	
E05b	1,18	46,9	0,19	0,20	98,0%	96,2%	13,8	0,8	99.9*	41.5*	
E06a	1,35	33,91	0,21	0,24	91,4%	77,1%	13,0	0,6	100.0*	45.8*	X
E06b	1,26	37,1	0,17	0,20	98,0%	92,4%	12,0	0,8	99.9*	38.0*	
E07a	1,27	46,92	0,19	0,23	95,5%	91,0%	10,2	0,7	99.9*	45.8*	
E07b	1,28	46,88	0,18	0,20	87,6%	53,1%	14,0	0,5	100.0*	31.5*	
E08a	1,11	46,88	0,22	0,22	96,7%	92,3%	11,2	0,7	99.9*	42.6*	X
E08b	1,11	42,69	0,19	0,20	98,0%	92,1%	9,6	0,7	99.9*	38.8*	X
E09a	1,22	33,96	0,21	0,24	94,4%	91,5%	9,7	0,6	99.9*	38.2*	
E09b	1,35	46,91	0,18	0,22	93,7%	91,2%	13,7	0,8	100.0*	45.0*	
E10a	1,21	34,03	0,19	0,22	96,2%	93,8%	9,2	0,6	99.9*	33.0*	
E10b	1,42	46,91	0,18	0,21	82,3%	38,9%	10,3	0,6	99.9*	40.7*	
E11a	1,27	46,92	0,21	0,25	90,2%	57,9%	9,4	0,5	99.8*	28.7*	
E11b	1,39	46,81	0,20	0,22	97,0%	93,3%	11,0	0,5	99.9*	41.4*	
E12a	1,17	33,11	0,18	0,21	97,6%	95,4%	12,4	0,8	99.9*	41.7*	X
E12b	1,18	34,04	0,17	0,19	92,1%	85,8%	12,0	0,7	99.9*	44.0*	X
F01a	1,11	46,87	0,20	0,22	97,2%	95,0%	13,0	1,1	99.9*	44.0*	
F01b	1,19	46,93	0,21	0,22	95,6%	93,0%	10,8	0,5	99.9*	40.4*	
F02a	1,19	46,91	0,17	0,19	97,4%	93,8%	11,2	0,8	99.9*	41.9*	
F02b	1,11	42,7	0,19	0,20	92,8%	74,0%	12,8	0,7	99.9*	37.5*	
F03a	1,15	42,7	0,18	0,20	95,2%	74,9%	12,8	0,5	99.9*	31.0*	X
F03b	1,42	33,92	0,19	0,23	81,8%	38,1%	14,1	0,6	100.0*	40.0*	X
F04a	1,22	33,94	0,20	0,23	93,3%	81,5%	12,0	0,6	100.0*	38.8*	X
F04b	1,42	42,68	0,20	0,23	96,2%	88,0%	16,6	1,2	100.0*	66.2*	X
F05a	1,52	32,93	0,20	0,23	85,8%	45,6%	13,4	0,5	100.0*	31.8*	
F05b	1,41	46,97	0,18	0,23	95,1%	77,1%	12,7	0,6	99.9*	38.9*	
F06a	1,25	34,03	0,19	0,21	97,0%	95,3%	10,5	0,9	99.9*	44.2*	
F06b	1,22	46,87	0,19	0,21	95,9%	92,7%	10,9	0,8	99.9*	45.1*	

F07a	1,32	33,98	0,19	0,23	98,0%	94,1%	8,5	1,0	99.7*	48.7*	
F07b	1,27	34,02	0,22	0,23	97,1%	93,5%	11,9	0,9	99.9*	44.9*	
F08a	1,32	34,18	0,20	0,24	98,7%	97,1%	11,3	0,7	99.9*	39.7*	
F08b	1,46	46,9	0,18	0,23	99,0%	98,2%	10,8	0,6	99.9*	42.8*	
F09a	1,25	32,23	0,18	0,21	97,8%	96,0%	10,2	0,6	99.9*	39.7*	X
F09b	1,35	37,39	0,20	0,22	96,2%	93,8%	10,6	0,7	99.9*	45.4*	
F10a	1,17	46,91	0,20	0,23	98,7%	96,5%	9,6	0,5	99.9*	34.4*	
F10b	1,27	46,85	0,21	0,24	98,4%	96,8%	13,1	0,9	99.9*	44.1*	
F11a	1,14	46,97	0,20	0,24	95,6%	93,0%	12,3	0,8	99.9*	42.4*	X
F11b	1,14	31,9	0,23	0,24	98,4%	94,3%	11,6	0,6	99.9*	34.6*	
F12a	1,22	46,85	0,20	0,22	94,0%	77,1%	10,1	0,6	99.9*	33.8*	
F12b	1,08	42,73	0,19	0,21	93,5%	89,0%	9,1	0,6	99.9*	41.3*	
G01a	1,17	42,72	0,19	0,21	90,2%	59,6%	11,9	0,6	99.9*	37.3*	
G01b	1,19	46,83	0,21	0,23	86,3%	50,8%	11,1	0,6	99.9*	37.7*	
G02a	1,21	46,87	0,19	0,22	99,0%	98,4%	11,4	0,6	99.9*	39.0*	
G02b	1,36	33,92	0,19	0,22	89,9%	66,7%	14,0	0,7	100.0*	47.5*	
G03a	1,21	46,77	0,19	0,22	92,8%	79,8%	13,3	0,8	99.9*	48.2*	X
G03b	1,14	46,9	0,20	0,22	93,4%	86,2%	13,1	0,7	99.9*	42.2*	X
G04a	1,25	42,62	0,19	0,21	95,5%	92,0%	11,2	0,8	99.9*	37.3*	X
G04b	1,29	46,76	0,20	0,23	93,7%	86,9%	11,6	0,7	99.9*	44.8*	
G05a	1,3	46,88	0,18	0,23	93,5%	69,9%	12,9	0,5	99.9*	32.6*	
G05b	1,21	42,7	0,18	0,22	98,8%	97,3%	11,0	0,7	99.9*	42.8*	X
G06a	1,17	42,61	0,19	0,21	97,1%	93,6%	8,9	0,5	99.9*	33.0*	
G06b	1,21	30,74	0,21	0,23	95,3%	90,5%	11,4	0,6	99.9*	35.8*	
G07a	1,25	42,7	0,18	0,22	97,0%	92,8%	11,7	0,7	99.9*	38.3*	
G07b	1,37	46,92	0,20	0,23	97,5%	89,1%	12,9	0,6	99.9*	33.9*	
G08a	1,23	37,19	0,20	0,22	91,7%	86,0%	12,8	0,7	100.0*	46.0*	
G08b	1,22	46,96	0,20	0,23	98,5%	96,6%	13,5	0,7	100.0*	36.1*	X
G09a	1,39	46,9	0,18	0,22	96,5%	91,7%	11,1	0,7	99.9*	47.0*	
G09b	1,26	46,79	0,20	0,22	96,9%	92,7%	10,1	0,6	99.9*	39.2*	
G10a	1,27	46,91	0,23	0,25	96,6%	92,4%	10,6	0,6	99.9*	39.4*	
G10b	1,3	33,98	0,21	0,24	96,6%	94,5%	11,6	0,7	99.9*	39.0*	
G11a	1,08	46,86	0,20	0,22	94,7%	91,5%	9,4	0,5	99.9*	43.9*	
G11b	1,21	46,89	0,21	0,23	98,4%	96,9%	11,0	0,6	99.9*	34.3*	
G12a	1,11	46,86	0,19	0,21	83,7%	40,3%	12,0	0,5	99.9*	36.2*	
H01a	1,49	42,79	0,18	0,22	93,9%	86,5%	10,5	0,5	99.9*	43.4*	X
H01b	1,26	42,81	0,18	0,20	82,6%	39,3%	15,0	0,8	100.0*	51.4*	X
H02a	1,4	32,31	0,20	0,21	98,8%	97,1%	12,3	0,6	99.9*	42.3*	
H02b	1,23	33,86	0,19	0,21	98,6%	97,3%	12,1	0,9	99.9*	44.6*	
H03a	1,53	42,76	0,21	0,24	98,1%	96,1%	13,8	0,8	100.0*	46.8*	
H03b	1,45	42,67	0,21	0,23	97,9%	95,7%	11,6	0,8	99.9*	44.2*	
H04a	1,37	46,69	0,22	0,25	97,0%	92,4%	11,3	0,6	99.9*	44.7*	
H04b	1,11	33,9	0,21	0,23	95,0%	91,1%	10,8	0,8	99.9*	37.8*	X
H05a	1,35	42,72	0,19	0,22	97,4%	96,0%	11,1	0,9	99.9*	50.4*	
H05b	1,45	46,77	0,21	0,26	95,2%	91,4%	9,4	0,5	99.9*	44.0*	
H06a	1,53	46,85	0,22	0,25	85,4%	45,0%	11,1	0,5	99.9*	34.0*	
H06b	1,27	46,84	0,21	0,22	96,4%	93,0%	11,8	0,9	99.9*	45.8*	
H07a	1,16	42,7	0,19	0,23	97,1%	94,8%	9,1	0,7	99.8*	40.2*	
H07b	1,25	32,88	0,19	0,23	96,4%	94,3%	10,6	0,6	99.9*	42.5*	

H08a	1,42	42,84	0,19	0,22	84,0%	48,5%	13,9	0,7	100.0*	43.0*	
H08b	1,3	33,96	0,21	0,23	93,3%	88,4%	11,6	0,7	99.9*	44.8*	
H09a	1,29	46,85	0,19	0,23	96,3%	94,4%	11,9	0,9	99.9*	44.6*	X
H09b	1,27	42,75	0,19	0,21	96,7%	93,4%	11,9	0,6	99.9*	41.4*	X
H10a	1,57	33,91	0,23	0,28	96,0%	93,8%	8,5	0,5	99.8*	41.3*	
H10b	1,24	42,64	0,20	0,22	93,8%	91,6%	11,2	0,6	99.9*	39.3*	
H11a	1,36	33,98	0,21	0,23	97,9%	95,4%	7,7	0,7	99.7*	44.8*	X
H11b	1,32	33,1	0,20	0,23	98,9%	97,9%	8,9	0,7	99.8*	41.9*	X
H12a	1,29	37	0,21	0,25	93,3%	91,1%	11,1	0,8	99.9*	47.2*	X
H12b	1,08	33,89	0,19	0,22	98,9%	97,1%	11,0	0,7	99.9*	35.4*	X

Table S.2: Overview of the crystallographic data and refinement statistics of *Bacillus subtilis* CdaA in complex with different ligands and *Listeria monocytogenes* CdaA in complex with Ruxolitinib.

Crystallographic data	**Δ100 *Lm*CdaA+ Ruxolitinib**	**Δ102 *Bs*CdaA+ Ruxolitinib**	**Δ102 *Bs*CdaA+ AMP**	**Δ102 *Bs*CdaA+ 7H-Pyrrolo[2,3-d]pyrimidine**	**Δ102 *Bs*CdaA+ adenine**
Beamline	Micromax 007	PetraIII, P14	BESSY II	Micromax 007	PetraIII, P14
Wavelenght (Å)	1.54179	0.97620	0.91840	1.54179	0.82656
Resolution range (Å)	65.06-2.85 (2.95-2.85)	46.32-1.25 (1.37-1.25)	46.76-1.8 (1.9-1.8)	42.92-1.75 (1.80-1.75)	67.77-1.12 (1.15-1.12)
Unique reflections	8968	80315	28355	34032	121471
Redundancy	6.9 (7.1)	6.8 (6.9)	3.7 (3.9)	18.5 (18.2)	5.7 (5.3)
Completeness (%)	98.5 (98.0)	97.3 (95.9)	97.8 (97.3)	99.8 (96.8)	99.4 (98.8)
Space group	$P2_12_12_1$	C2	C2	C2	C2
a, b, c (Å)	43.28, 64.90, 130.13	119.00, 39.10, 67.46	119.04, 38.22, 68.11	118.53, 39.17, 67.49	118.91, 39.59, 68.05
α, β, γ (°)	90.00, 90.00, 90.00	90.00, 94.49, 90.00	90.00, 95.13, 90.00	90.00, 94.09, 90.00	90.00, 95.13, 90,00
R_{merge} (%)	16.8 (135.0)	8.4 (108.4)	10.6 (81.6)	10.1 (149.6)	7.8 (89.3)
I/σ (I)	10.51 (1.55)	12.05 (1.87)	10.35 (1.62)	19.97 (1.90)	11.00 (1.36)
$CC_{1/2}$	99.8 (65.7)	99.4 (91.9)	99.8 (78.1)	100 (68.7)	99.4 (90.7)
Wilson B ($Å^2$)	59.9	19.3	21.1	23.8	16.1
Refinement statistics					
R_{work}/R_{free} (%)	0. 249/0.305	0.162/0.189	0.199/0.241	0.195/0.232	0.159/0.181
No. of atoms	5876	5032	5010	4996	5695
B-factors ($Å^2$)					
Protein	54	31	27	32	24
Ligand	59	45	37	29	39
R.m.s deviations					
Bond lengths (Å)	0.007	0.0093	0.0041	0.0102	0.015
Bond angles (°)	1.000	0.975	0.640	1.620	1.390
Molprobity analysis					
Ramachandran. favoured (%)	98.68	99.01	98.33	98.03	98.68
Ramachandran. outliers (%)	0.00	0.00	0.00	0.00	0.00
Rotamer outliers (%)	2.28	1.96	0.40	2.76	1.03
Clashscore	13.5	6.82	4.02	7.36	6.80

Table S.3: Overview of the crystallographic data and refinement statistics of *Bacillus subtilis* CdaA, S*treptococcus pneumoniae* CdaA in complex with c-di-AMP, *Enterococcus feacium* CdaA APO and bound to c-di-AMP.

Crystallographic data	**Δ84 *Sp*CdaA+ c-di-AMP**	**Δ121 *Ef*CdaA**	**Δ121 *Ef*CdaA+ c-di-AMP**	**Δ102 *Bs*CdaA**
Beamline	ESRF,ID-23.1	PetraIII, P14	PetraIII, P14	Micromax 007
Wavelenght (Å)	0.96770	0.97626	0.97626	1.54179
Resolution range (Å)	43.28-2.4 (2.46-2.40)	49.58-2.45 (2.52-2.45)	41.06-2.2 (2.26-2.2)	29.58-1.71 (1.76-1.71)
Unique reflections	17025	11890	106067	33652
Redundancy	6.9 (7.1)	37.1 (39.1)	6.9 (7.1)	12.47(11.03)
Completeness (%)	99.9 (100.0)	100.0 (100.0)	98.7 (99.0)	97.8 (95.6)
Space group	$P2_12_12_1$	$P6_32_2$	P2	C2
a, b, c (Å)	86.57, 86.57, 110.62	99.16, 99.16, 112.18	68.74 , 213.76, 68.87	118.72, 39.82, 67.61
α, β, γ (°)	90.00, 90.00, 90.00	90.00, 90.00, 120.00	90.00, 111.34, 90.00	90.00, 94.09, 90.00
R_{merge} (%)	27.1 (163.4)	38.5 (347.3)	5.2 (163.7)	10.1 (149.6)
I/σ (I)	8.07 (1.82)	17.4 (3.78)	18.03 (1.21)	18.86 (1.5)
$CC_{1/2}$	99.9 (81.6)	99.9 (79.2)	100 (47.5)	99.9 (68.3)
Wilson B ($Å^2$)	57.4	59.4	54.9	26.8
Refinement statistics				
R_{work}/R_{free} (%)	0. 224/0.252	0.220/0.272	0.225/0.263	0.169/0.206
No. of atoms	2462	2296	11340	2448
B-factors ($Å^2$)				
Protein	65	67	70	34
Ligand	72	57	62	43
R.m.s deviations				
Bond lengths (Å)	0.009	0.015	0.008	0.003
Bond angles (°)	1.065	1.780	1.044	0.534
Molprobity analysis				
Ramachandran favoured (%)	91.75	96.25	94.09	99.01
Ramachandran. outliers (%)	0.33	0.00	0.62	0.00
Rotamer outliers (%)	3.80	5.18	2.33	0.39
Clashscore	7.10	8.34	11.52	1.08

Table S.4: Overview of organism and CdaA UniProt ID which were used to calculate the *Consurf* model.

Organism name	uniprot ID
Listeria monocytogenes serovar 1/2a (strain ATCC BAA-679 / EGD)	Q8Y5E4
Staphylococcus sp. SB1-57	A0A897ITF9
Streptococcus canis	A0A3P5XSP2
Borreliella burgdorferi	A0A8F9U449
Staphylococcus argenteus	A0A7U7JQN7
Borrelia miyamotoi	A0A8D5SKZ9
Chlamydiae bacterium	A0A6M1YNL9
Staphylococcus hominis	A0A2A1M6F3
Enterococcus faecalis	A0A1B4XQ13
Enterococcus lactis	A0A8F7ZHD2
Enterococcus durans	A0A377KN92
Enterococcus faecium	A0A2V2LDT6
Streptococcus pneumoniae	A0A6G2IPG2
Streptococcus suis	A0A0N0DPT7
Streptococcus mutans	A0A2J9QDI4
Streptococcus sanguinis	A0A5A7ZFS8
Streptococcus pyogenes	A0A2W5CLA8
Staphylococcus aureus	A0A8G1LN88
Staphylococcus epidermidis	A0A854CVL7
Staphylococcus saprophyticus	A0A380HLP3

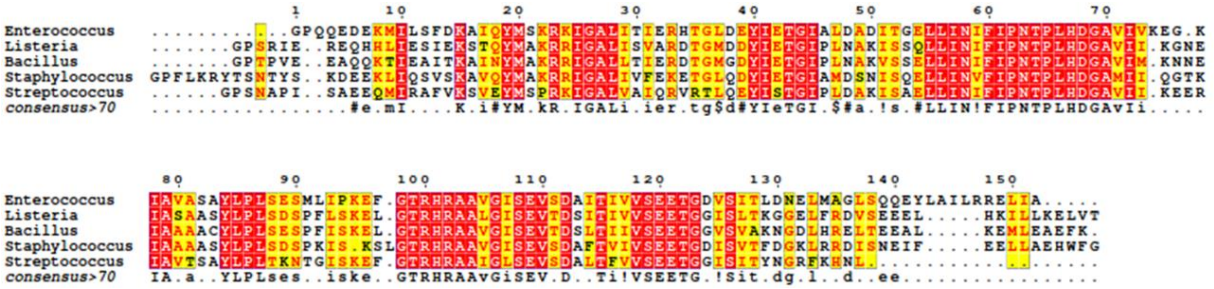

Figure S.1: Sequence alignment of all used CdaA construct. The sequences enconding for the CdaA of *Enterococcus faecium, Listeria monocytogenes, Bacillus subtilis, Staphylococcus aureus* and *Streptococcus pneumoniae* were N-and C-terminal truncated and cloned into to pet-28a vector. Alignment was performed using the T-Coffee server in combination with ESPript 3.0 (Robert & Gouet, 2014b; Floden *et al*, 2016).

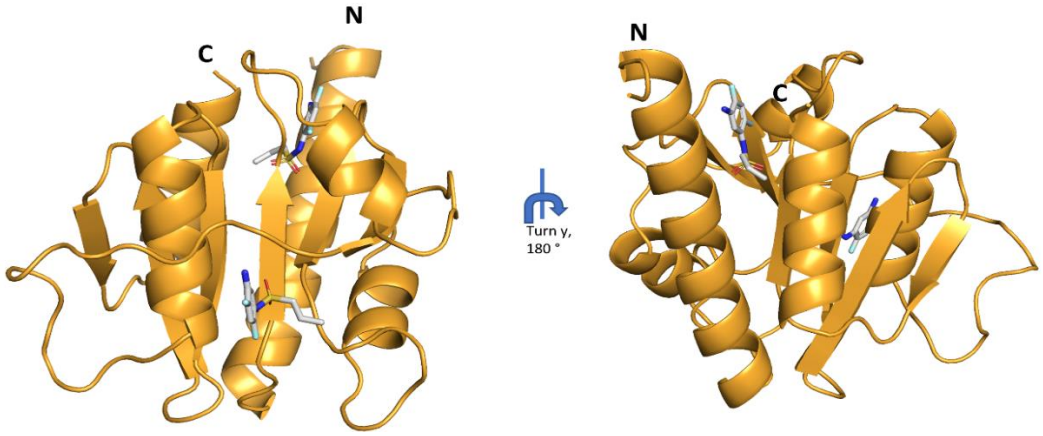

Figure S.2: *Bacillus subtilis* CdaA in complex with the fragment D02. The *Bacillus subtilis* CdaA is depicted as *cartoon* and colored in wheat. The fragment D02 from the F2X-entry screen is depicted as *sticks* (C-atom in grey, N-atom in blue, O-atom in red and F-atom in turquoise). It can be observed that the fragment binds in the active site as well as between the N-and C-terminal located α-helices.

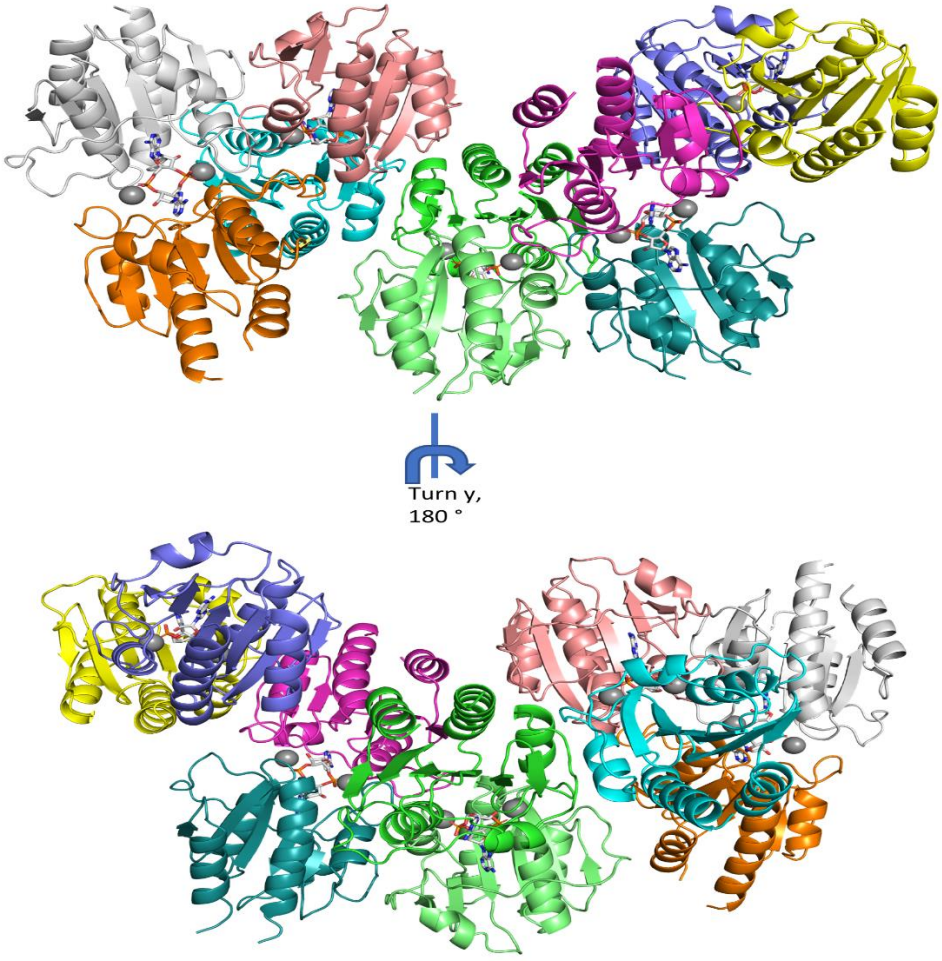

Figure S.3: Representation of the content of the asymmetric unit of *Enterococcus faecium* CdaA in complex with c-di-AMP. CdaA molecules are presented as *cartoon*. Every protomer, except the yellow and grey one is involved in the formation of an active and a back-to-back dimer. Overall, the molecules arrange in a helical manner. The manganese atoms are shown as *spheres* in grey, while c-di-amp is presented as *sticks* (C-atom in grey, N-atom in blue, O-atom in red and P-atom in orange).

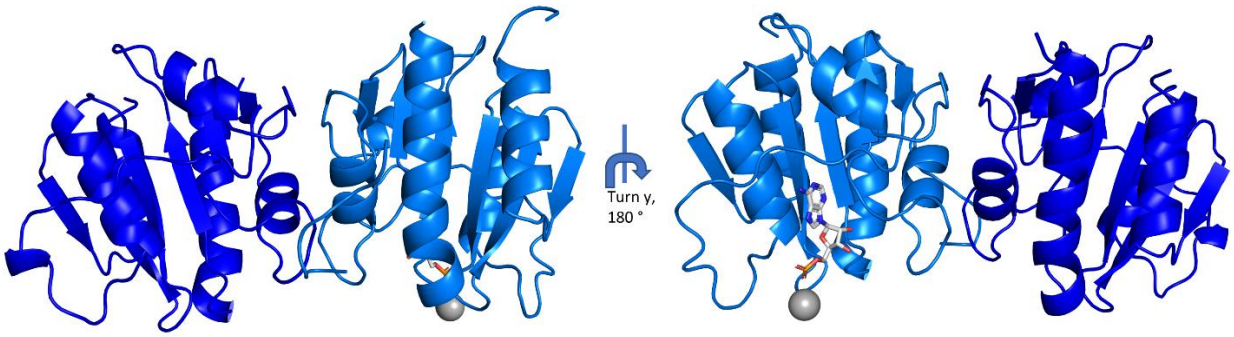

Figure S.4: Representation of the content of the asymmetric unit of *Streptococcus pneumoniae* CdaA in complex with c-di-AMP. CdaA molecules are presented as *cartoon* in blue and marine. Both protomers are forming an inactive back-to-back dimer. The magnesium atom is shown as *spheres* in grey, while AMP is presented as *sticks* (C-atom in grey, N-atom in blue, O-atom in red and P-atom in orange).

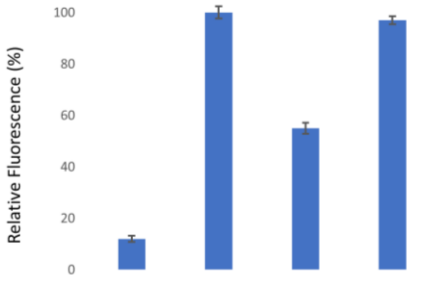

coralyne	+	+	+	+
KBr	+	+	+	+
c-di-AMP	-	+	+	+
D02	-	-	+	-
Ruxolitinib	-	-	-	+

Figure S.5: Control experiments employing the coralyne assay. To ensure that the fragment D02 or the compound Ruxolitinib does not interact with coralyne or interfere with the interaction of coralyne and c-di-AMP, these control experiments were carried out. It can be observed that the sample with the fragment exhibit just 60% of the positive control fluorescence, while the presence of Ruxolitinib does not change the measured fluorescence. All measurements were performed as triplicates, shown are mean values, the error bars correspond to standard deviation.

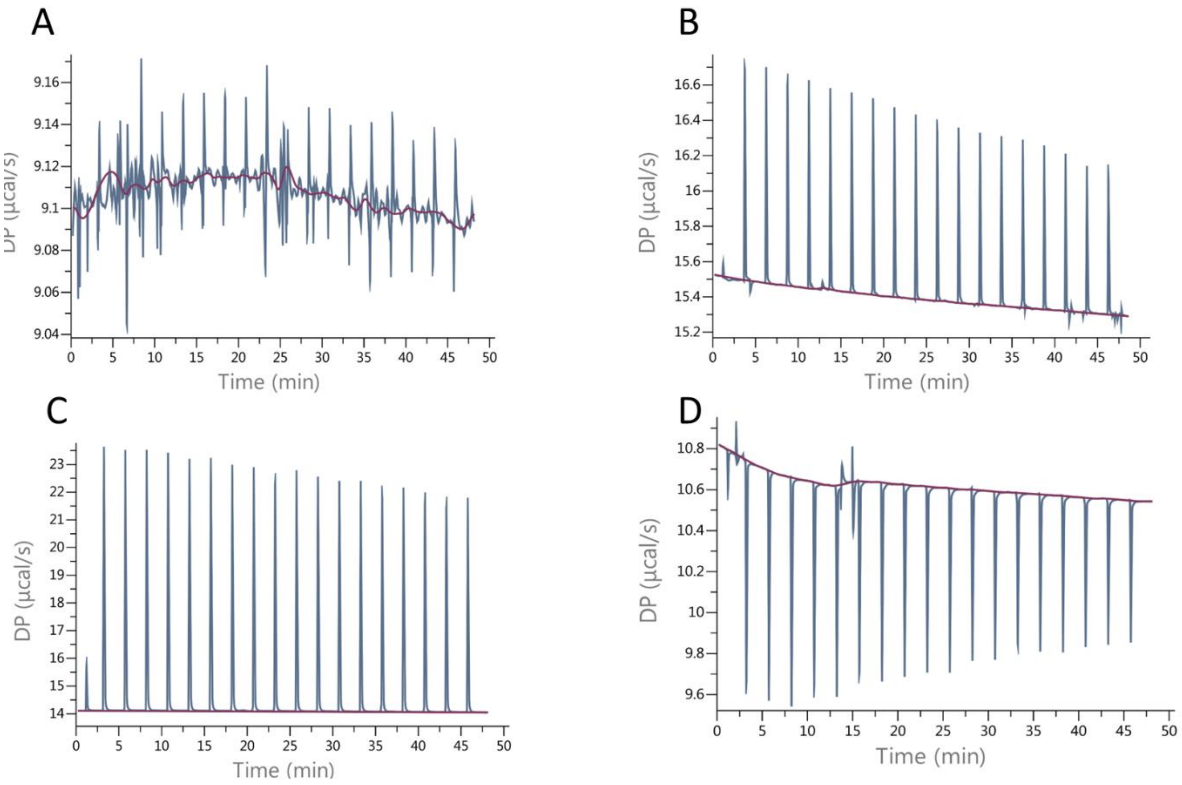

Figure S.6: ITC control measurements. **A** presents the buffer to protein control. **B** presents the results of 12 mM AMP against the buffer. **C** presents the results of 11.2 mM ATP against buffer. **D** presents the results of 1.2 mM Ruxolitinib against buffer. All these shown data were subtracted from the corresponding protein-ligand measurements via point-to-point subtraction to calculate the binding affinity.

7 References

Abbas A, Linman MJ & Cheng Q (2011) New trends in instrumental design for surface plasmon resonance-based biosensors. *Biosens Bioelectron* 26: 1815–1824

Agostoni M, Logan-Jackson AR, Heinz ER, Severin GB, Bruger EL, Waters CM & Montgomery BL (2018) Homeostasis of Second Messenger Cyclic-di-AMP Is Critical for Cyanobacterial Fitness and Acclimation to Abiotic Stress. *Front Microbiol* 9:1121

Al-Azayzih A, Missaoui WN, Cummings BS & Somanath PR (2016) Liposome-mediated delivery of the p21 activated kinase-1 (PAK-1) inhibitor IPA-3 limits prostate tumor growth in vivo. *Nanomedicine* 12: 1231–1239

Alexander Fleming (1929) On the Antibacterial Action of Cultures of a Penicillium, with Special Reference to their Use in the Isolation of B. influenzæ. *Br J Exp Pathol*

Alexandrova LA, Khandazhinskaya AL, Matyugina ES, Makarov DA & Kochetkov SN (2022) Analogues of Pyrimidine Nucleosides as Mycobacteria Growth Inhibitors. *Microorganisms* 10: 1299

Ali Syed M (2016) Antibiotics: Past, Present and Future. *J Biomol Res Ther* 5:2

Altarac D, Gutch M, Mueller J, Ronsheim M, Tommasi R & Perros M (2021) Challenges and opportunities in the discovery, development, and commercialization of pathogen-targeted antibiotics. *Drug Discov Today* 26: 2084–2089

Anashkin VA, Salminen A, Tuominen HK, Orlov VN, Lahti R & Baykov AA (2015) Cystathionine β-Synthase (CBS) Domain-containing Pyrophosphatase as a Target for Diadenosine Polyphosphates in Bacteria. *Journal of Biological Chemistry* 290: 27594–27603

Antonysamy S, Hirst G, Park F, Sprengeler P, Stappenbeck F, Steensma R, Wilson M & Wong M (2009) Fragment-based discovery of JAK-2 inhibitors. *Bioorg Med Chem Lett* 19: 279–282

Artis DR, Lin JJ, Zhang C, Wang W, Mehra U, Perreault M, Erbe D, Krupka HI, England BP, Arnold J, *et al* (2009) Scaffold-based discovery of indeglitazar, a PPAR pan-active anti-diabetic agent. *Proceedings of the National Academy of Sciences* 106: 262–267

Ashman DF, Lipton R, Melicow MM & Price TD (1963) Isolation of adenosine 3',5'-monophosphate and guanosine 3',5'-monophosphate from rat urine. *Biochem Biophys Res Commun* 11: 330–334

Bähre H, Hartwig C, Munder A, Wolter S, Stelzer T, Schirmer B, Beckert U, Frank DW, Tümmler B, Kaever V, *et al* (2015) cCMP and cUMP occur in vivo. *Biochem Biophys Res Commun* 460: 909–914

Bai Y, Yang J, Zarrella TM, Zhang Y, Metzger DW & Bai G (2014) Cyclic Di-AMP Impairs Potassium Uptake Mediated by a Cyclic Di-AMP Binding Protein in Streptococcus pneumoniae. *J Bacteriol* 196: 614–623

Bai Y, Yang J, Zhou X, Ding X, Eisele LE & Bai G (2012) Mycobacterium tuberculosis Rv3586 (DacA) Is a Diadenylate Cyclase That Converts ATP or ADP into c-di-AMP. *PLoS One* 7: e35206

Ball P (2007) The clinical development and launch of amoxicillin/clavulanate for the treatment of a range of community-acquired infections. *Int J Antimicrob Agents* 30: 113–117

Bandera AM, Bartho J, Lammens K, Drexler DJ, Kleinschwärzer J, Hopfner K-P & Witte G (2021) BusR senses bipartite DNA binding motifs by a unique molecular ruler architecture. *Nucleic Acids Res* 49: 10166–10177

Barb AW, Borgert AJ, Liu M, Barany G & Live D (2010) Intramolecular Glycan–Protein Interactions in Glycoproteins. In pp 365–388.

Basso CR, Malossi CD, Haisi A, de Albuquerque Pedrosa V, Barbosa AN, Grotto RT & Araujo Junior JP (2021) Fast and reliable detection of SARS-CoV-2 antibodies based on surface plasmon resonance. *Analytical Methods* 13: 3297–3306

Batool M, Ahmad B & Choi S (2019) A Structure-Based Drug Discovery Paradigm. *Int J Mol Sci* 20: 2783

Battye TGG, Kontogiannis L, Johnson O, Powell HR & Leslie AGW (2011) *iMOSFLM* : a new graphical interface for diffraction-image processing with *MOSFLM*. *Acta Crystallogr D Biol Crystallogr* 67: 271–281

Baybekov S, Marcou G, Ramos P, Saurel O, Galzi J-L & Varnek A (2021) DMSO Solubility Assessment for Fragment-Based Screening. *Molecules* 26: 3950

Beadle BM, Nicholas RA & Shoichet BK (2001) Interaction energies between β-lactam antibiotics and E. coli penicillin-binding protein 5 by reversible thermal denaturation. *Protein Science* 10: 1254–1259

Begley DW, Davies DR, C. Hartley R, Edwards TE, Staker BL, van Voorhis WC, Myler PJ & Stewart LJ (2011) Fragment Screening of Infectious Disease Targets in a Structural Genomics Environment. In pp 533–556.

Bhullar KS, Lagarón NO, McGowan EM, Parmar I, Jha A, Hubbard BP & Rupasinghe HPV (2018) Kinase-targeted cancer therapies: progress, challenges and future directions. *Mol Cancer* 17: 48

Blair JMA, Webber MA, Baylay AJ, Ogbolu DO & Piddock LJ v. (2015) Molecular mechanisms of antibiotic resistance. *Nat Rev Microbiol* 13: 42–51

Blötz C, Treffon K, Kaever V, Schwede F, Hammer E & Stülke J (2017) Identification of the Components Involved in Cyclic Di-AMP Signaling in Mycoplasma pneumoniae. *Front Microbiol* 8

Bollag G, Tsai J, Zhang J, Zhang C, Ibrahim P, Nolop K & Hirth P (2012) Vemurafenib: the first drug approved for BRAF-mutant cancer. *Nat Rev Drug Discov* 11: 873–886

Botsford JL & Harman JG (1992) Cyclic AMP in Prokaryotes

Boyd NK, Teng C & Frei CR (2021) Brief Overview of Approaches and Challenges in New Antibiotic Development: A Focus On Drug Repurposing. *Front Cell Infect Microbiol* 11

Braun F, Recalde A, Bähre H, Seifert R & Albers S-V (2021) Putative Nucleotide-Based Second Messengers in the Archaeal Model Organisms Haloferax volcanii and Sulfolobus acidocaldarius. *Front Microbiol* 12

Carpenter DK (1977) Dynamic Light Scattering with Applications to Chemistry, Biology, and Physics (Berne, Bruce J.; Pecora, Robert). *J Chem Educ* 54: A430

Cashel M & Gallant J (1969) Two Compounds implicated in the Function of the RC Gene of Escherichia coli. *Nature* 221: 838–841

CDC (2022) COVID-19: U.S. Impact on Antimicrobial Resistance, Special Report 2022 Atlanta, Georgia

Chan HTH, Moesser MA, Walters RK, Malla TR, Twidale RM, John T, Deeks HM, Johnston-Wood T, Mikhailov V, Sessions RB, *et al* (2022) Discovery of SARS-CoV-2 M pro Peptide Inhibitors from Modelling Substrate and Ligand Binding. *biorixv*

Chavanieu A & Pugnière M (2016) Developments in SPR Fragment Screening. *Expert Opin Drug Discov* 11: 489–499

Chen L, Li X, Zhou X, Zeng J, Ren Z, Lei L, Kang D, Zhang K, Zou J & Li Y (2018) Inhibition of Enterococcus faecalis Growth and Biofilm Formation by Molecule Targeting Cyclic di-AMP Synthetase Activity. *J Endod* 44: 1381-1388.e2

Cheng X, Zheng X, Zhou X, Zeng J, Ren Z, Xu X, Cheng L, Li M, Li J & Li Y (2016) Regulation of oxidative response and extracellular polysaccharide synthesis by a diadenylate cyclase in *S treptococcus mutans*. *Environ Microbiol* 18: 904–922

Chopra I & Roberts M (2001) Tetracycline Antibiotics: Mode of Action, Applications, Molecular Biology, and Epidemiology of Bacterial Resistance. *Microbiology and Molecular Biology Reviews* 65: 232–260

Ciulli A & Abell C (2007) Fragment-based approaches to enzyme inhibition. *Curr Opin Biotechnol* 18: 489–496

Ciulli A, Williams G, Smith AG, Blundell TL & Abell C (2006) Probing Hot Spots at Protein−Ligand Binding Sites: A Fragment-Based Approach Using Biophysical Methods. *J Med Chem* 49: 4992–5000

Collins PM, Douangamath A, Talon R, Dias A, Brandao-Neto J, Krojer T & von Delft F (2018) Achieving a Good Crystal System for Crystallographic X-Ray Fragment Screening. In *Methods Enzymology* pp 251–264.

Commichau FM, Dickmanns A, Gundlach J, Ficner R & Stülke J (2015) A jack of all trades: the multiple roles of the unique essential second messenger cyclic di-AMP. *Mol Microbiol* 97: 189–204

Commichau FM, Heidemann JL, Ficner R & Stülke J (2019) Making and Breaking of an Essential Poison: the Cyclases and Phosphodiesterases That Produce and Degrade the Essential Second Messenger Cyclic di-AMP in Bacteria. *J Bacteriol* 201

Cong Y, Yang S & Rao X (2020) Vancomycin resistant Staphylococcus aureus infections: A review of case updating and clinical features. *J Adv Res* 21: 169–176

Congreve M, Carr R, Murray C & Jhoti H (2003) A 'Rule of Three' for fragment-based lead discovery? *Drug Discov Today* 8: 876–877

Corrigan RM, Abbott JC, Burhenne H, Kaever V & Gründling A (2011) c-di-AMP Is a New Second Messenger in Staphylococcus aureus with a Role in Controlling Cell Size and Envelope Stress. *PLoS Pathog* 7: e1002217

Corrigan RM & Gründling A (2013) Cyclic di-AMP: another second messenger enters the fray. *Nat Rev Microbiol* 11: 513–524

Dalvit C, Fasolini M, Flocco M, Knapp S, Pevarello P & Veronesi M (2002) NMR-Based Screening with Competition Water−Ligand Observed via Gradient Spectroscopy Experiments: Detection of High-Affinity Ligands. *J Med Chem* 45: 2610–2614

Dé E, Baslé A, Jaquinod M, Saint N, Malléa M, Molle G & Pagès J-M (2001) A new mechanism of antibiotic resistance in Enterobacteriaceae induced by a structural modification of the major porin. *Mol Microbiol* 41: 189–198

Dengler V, McCallum N, Kiefer P, Christen P, Patrignani A, Vorholt JA, Berger-Bächi B & Senn MM (2013) Mutation in the C-Di-AMP Cyclase dacA Affects Fitness and Resistance of Methicillin Resistant Staphylococcus aureus. *PLoS One* 8: e73512

Devaux L, Sleiman D, Mazzuoli M-V, Gominet M, Lanotte P, Trieu-Cuot P, Kaminski P-A & Firon A (2018) Cyclic di-AMP regulation of osmotic homeostasis is essential in Group B Streptococcus. *PLoS Genet* 14: e1007342

Di L & Kerns EH (2012) Solubility Issues in Early Discovery and HTS. In *Solvent Systems and Their Selection in Pharmaceutics and Biopharmaceutics* pp 111–136. New York, NY: Springer New York

Douangamath A, Powell A, Fearon D, Collins PM, Talon R, Krojer T, Skyner R, Brandao-Neto J, Dunnett L, Dias A, *et al* (2021) Achieving Efficient Fragment Screening at XChem Facility at Diamond Light Source. *Journal of Visualized Experiments*

Du B & Sun JH (2015) Diadenylate cyclase evaluation of ssDacA (SSU98_1483) in Streptococcus suis serotype 2. *Genetics and Molecular Research* 14: 6917–6924

Duggar BM (1948) Aureomycin: A product of the continuing search fpr new antibiotics. *Ann N Y Acad Sci* 51: 177–181

Edink E, Rucktooa P, Retra K, Akdemir A, Nahar T, Zuiderveld O, van Elk R, Janssen E, van Nierop P, van Muijlwijk-Koezen J, *et al* (2011) Fragment Growing Induces Conformational Changes in Acetylcholine-Binding Protein: A Structural and Thermodynamic Analysis. *J Am Chem Soc* 133: 5363–5371

Eliopoulos GM & Huovinen P (2001) Resistance to Trimethoprim-Sulfamethoxazole. *Clinical Infectious Diseases* 32: 1608–1614

Emsley P, Lohkamp B, Scott WG & Cowtan K (2010) Features and development of *Coot*. *Acta Crystallogr D Biol Crystallogr* 66: 486–501

Epstein W (2003) The Roles and Regulation of Potassium in Bacteria. *Prog Nucleic Acid Res Mol Biol.*;75:293-320.

Erlanson DA, Wells JA & Braisted AC (2004) Tethering: Fragment-Based Drug Discovery. *Annu Rev Biophys Biomol Struct* 33: 199–223

Ernst O & Zor T (2010) Linearization of the Bradford Protein Assay. *Journal of Visualized Experiments* 38: 1918

Evans DR, Griffith MP, Sundermann AJ, Shutt KA, Saul MI, Mustapha MM, Marsh JW, Cooper VS, Harrison LH & van Tyne D (2020) Systematic detection of horizontal gene transfer across genera among multidrug-resistant bacteria in a single hospital. *Elife* 9:e53886

Fàbrega A, Madurga S, Giralt E & Vila J (2009) Mechanism of action of and resistance to quinolones. *Microb Biotechnol* 2: 40–61

Fahmi T, Port G & Cho K (2017) c-di-AMP: An Essential Molecule in the Signaling Pathways that Regulate the Viability and Virulence of Gram-Positive Bacteria. *Genes (Basel)* 8: 197

Fischer T & Riedl R (2013) Strategic Targeting of Multiple Water-Mediated Interactions: A Concise and Rational Structure-Based Design Approach to Potent and Selective MMP-13 Inhibitors. *ChemMedChem* 8: 1457–1461

FitzGerald EA (2021) Fragment-based drug discovery : Novel methods and strategies for identifying and evolving fragment leads

Floden EW, Tommaso PD, Chatzou M, Magis C, Notredame C & Chang J-M (2016) PSI/TM-Coffee: a web server for fast and accurate multiple sequence alignments of regular and transmembrane proteins using homology extension on reduced databases. *Nucleic Acids Res* 44: W339-43

Foloppe N (2011) The benefits of constructing leads from fragment hits. *Future Med Chem* 3: 1111–1115

Fradera X, Reutershan MH, Machacek MR, Trotter BW & McCoy MA (2022) NMR Data-Driven Docking of HDM2-Inhibitor Complexes. *ChemBioChem* 23(6): e202100570

Freidel MR & Armen RS (2021) Mapping major SARS-CoV-2 drug targets and assessment of druggability using computational fragment screening: Identification of an allosteric small-molecule binding site on the Nsp13 helicase. *PLoS One* 16: e0246181

Fuentes DE, Navarro CA, Tantaleán JC, Araya MA, Saavedra CP, Pérez JM, Calderón IL, Youderian PA, Mora GC & Vásquez CC (2005) The product of the qacC gene of Staphylococcus epidermidis CH mediates resistance to β-lactam antibiotics in Gram-positive and Gram-negative bacteria. *Res Microbiol* 156: 472–477

Furniss RCD, Kaderabkova N, Barker D, Bernal P, Maslova E, Antwi AA, McNeil HE, Pugh HL, Dortet L, Blair JM, *et al* (2022) Breaking antimicrobial resistance by disrupting extracytoplasmic protein folding. *Elife* 11: e57974

Gagic Z, Ruzic D, Djokovic N, Djikic T & Nikolic K (2020) In silico Methods for Design of Kinase Inhibitors as Anticancer Drugs. *Front Chem* 7:873

Gardete S & Tomasz A (2014) Mechanisms of vancomycin resistance in Staphylococcus aureus. *Journal of Clinical Investigation* 124: 2836–2840

Gelmedin V, Dissous C & Grevelding CG (2015) Re-positioning protein-kinase inhibitors against schistosomiasis. *Future Med Chem* 7: 737–752

Gibhardt J, Heidemann JL, Bremenkamp R, Rosenberg J, Seifert R, Kaever V, Ficner R & Commichau FM (2020) An extracytoplasmic protein and a moonlighting enzyme

modulate synthesis of c-di-AMP in *Listeria monocytogenes*. *Environ Microbiol* 22: 2771–2791

Gottesman S (2019) Trouble is coming: Signaling pathways that regulate general stress responses in bacteria. *Journal of Biological Chemistry* 294: 11685–11700

Gundlach J, Herzberg C, Hertel D, Thürmer A, Daniel R, Link H & Stülke J (2017a) Adaptation of *Bacillus subtilis* to Life at Extreme Potassium Limitation. *mBio* 8(4) :e00861-17

Gundlach J, Herzberg C, Kaever V, Gunka K, Hoffmann T, Weiß M, Gibhardt J, Thürmer A, Hertel D, Daniel R, *et al* (2017b) Control of potassium homeostasis is an essential function of the second messenger cyclic di-AMP in *Bacillus subtilis*. *Sci Signal* 10(475):eaal3011

Gundlach J, Krüger L, Herzberg C, Turdiev A, Poehlein A, Tascón I, Weiss M, Hertel D, Daniel R, Hänelt I, *et al* (2019a) Sustained sensing in potassium homeostasis: Cyclic di-AMP controls potassium uptake by KimA at the levels of expression and activity. *Journal of Biological Chemistry* 294: 9605–9614

Gundlach J, Mehne FMP, Herzberg C, Kampf J, Valerius O, Kaever V & Stülke J (2015) An Essential Poison: Synthesis and Degradation of Cyclic Di-AMP in Bacillus subtilis. *J Bacteriol* 197: 3265–3274

Günther S, Reinke PYA, Fernández-García Y, Lieske J, Lane TJ, Ginn HM, Koua FHM, Ehrt C, Ewert W, Oberthuer D, *et al* (2021) X-ray screening identifies active site and allosteric inhibitors of SARS-CoV-2 main protease. *Science (1979)* 372: 642–646

Haenni M & Moreillon P (2006) Mutations in Penicillin-Binding Protein (PBP) genes and in non-PBP genes during selection of penicillin-resistant Streptococcus gordonii. *Antimicrob Agents Chemother* 50: 4053–4061

Hajduk PJ & Greer J (2007) A decade of fragment-based drug design: strategic advances and lessons learned. *Nat Rev Drug Discov* 6: 211–219

Hamilton DJ, Beemsterboer M, Carter CM, Elsayed J, Huiberts REM, Klein HF, O'Brien P, Esch IJP & Wijtmans M (2022) Puckering the Planar Landscape of Fragments: Design and Synthesis of a 3D Cyclobutane Fragment Library. *ChemMedChem* 17 (9): e202200113

Hao X, Zhou X, Zhang Y, Han Y, Xu Z, Ma C, Qi K, Fan S & Li M (2022) Structure and function of diadenylate cyclase DacM from Mycoplasma ovipneumoniae: Preprint from bioRxiv

Harrison C, Kiladjian J-J, Al-Ali HK, Gisslinger H, Waltzman R, Stalbovskaya V, McQuitty M, Hunter DS, Levy R, Knoops L, *et al* (2012) JAK Inhibition with Ruxolitinib versus Best Available Therapy for Myelofibrosis. *New England Journal of Medicine* 366: 787–798

Heidemann JL, Neumann P, Dickmanns A & Ficner R (2019) Crystal structures of the c-di-AMP–synthesizing enzyme CdaA. *Journal of Biological Chemistry* 294: 10463–10470

Heidemann JL, Neumann P, Krüger L, Wicke D, Vinhoven L, Linden A, Dickmanns A, Stülke J, Urlaub H & Ficner R (2022) Structural basis for c-di-AMP–dependent regulation of the bacterial stringent response by receptor protein DarB. *Journal of Biological Chemistry* 298: 102144

Hengge R, Häussler S, Pruteanu M, Stülke J, Tschowri N & Turgay K (2019) Recent Advances and Current Trends in Nucleotide Second Messenger Signaling in Bacteria. *J Mol Biol* 431: 908–927

Henning LN, Carpenter S, Stark G v. & Serbina N v. (2018) Development of Protective Immunity in New Zealand White Rabbits Challenged with Bacillus anthracis Spores and Treated with Antibiotics and Obiltoxaximab, a Monoclonal Antibody against Protective Antigen. *Antimicrob Agents Chemother* 62 (2):e01590-17

Hopkins AL, Groom CR & Alex A (2004) Ligand efficiency: a useful metric for lead selection. *Drug Discov Today* 9: 430–431

Hopkins AL, Keserü GM, Leeson PD, Rees DC & Reynolds CH (2014) The role of ligand efficiency metrics in drug discovery. *Nat Rev Drug Discov* 13: 105–121

Hughes D & Karlén A (2014) Discovery and preclinical development of new antibiotics. *Ups J Med Sci* 119: 162–169

Hutchings MI, Truman AW & Wilkinson B (2019) Antibiotics: past, present and future. *Curr Opin Microbiol* 51: 72–80

Huynh K & Partch CL (2015) Analysis of Protein Stability and Ligand Interactions by Thermal Shift Assay. *Curr Protoc Protein Sci* 79 :28.9.1-28.9.14

Jackson-Litteken CD, Ratliff CT, Kneubehl AR, Siletti C, Pack L, Lan R, Huynh TN, Lopez JE & Blevins JS (2021) The Diadenylate Cyclase CdaA Is Critical for Borrelia turicatae Virulence and Physiology. *Infect Immun* 89 (6):e00787-20

Jencks WP (1981) On the attribution and additivity of binding energies. *Proceedings of the National Academy of Sciences* 78: 4046–4050

Ji X, Zhang Y, Zhang L, Chen H, Peng Y & Tang P (2016) Inhibition of p21-Activated Kinase 1 by IPA-3 Promotes Locomotor Recovery After Spinal Cord Injury in Mice. *Spine (Phila Pa 1976)* 41: 919–925

Johnston T, Hendricks GL, Shen S, Chen RF, Kwon B, Kelso MJ, Kim W, Burgwyn Fuchs B & Mylonakis E (2016) Raf-kinase inhibitor GW5074 shows antibacterial activity against

methicillin-resistant *Staphylococcus aureus* and potentiates the activity of gentamicin. *Future Med Chem* 8: 1941–1952

Kabsch W (2010) *XDS*. *Acta Crystallogr D Biol Crystallogr* 66: 125–132

Karawajczyk A, Giordanetto F, Benningshof J, Hamza D, Kalliokoski T, Pouwer K, Morgentin R, Nelson A, Müller G, Piechot A, *et al* (2015) Expansion of chemical space for collaborative lead generation and drug discovery: the European Lead Factory Perspective. *Drug Discov Today* 20: 1310–1316

Kashyap A, Singh PK & Silakari O (2019) Counting on Fragment Based Drug Design Approach for Drug Discovery. *Curr Top Med Chem* 18: 2284–2293

Khoshbakht R, Kabiri M, Neshani A, Khaksari MN, Sadrzadeh SM, Mousavi SM, Ghazvini K & Ghavidel M (2022) Assessment of antibiotic resistance changes during the Covid-19 pandemic in northeast of Iran during 2020–2022: an epidemiological study. *Antimicrob Resist Infect Control* 11: 121

Kim BS, Howell MD, Sun K, Papp K, Nasir A & Kuligowski ME (2020) Treatment of atopic dermatitis with ruxolitinib cream (JAK1/JAK2 inhibitor) or triamcinolone cream. *Journal of Allergy and Clinical Immunology* 145: 572–582

King A & Blackledge MS (2021) Evaluation of small molecule kinase inhibitors as novel antimicrobial and antibiofilm agents. *Chem Biol Drug Des* 98: 1038–1064

Kleywegt GJ (1996) Use of Non-crystallographic Symmetry in Protein Structure Refinement. *Acta Crystallogr D Biol Crystallogr* 52: 842–857

Kong H-K, Pan Q, Lo W-U, Liu X, Law COK, Chan T, Ho P-L & Lau TC-K (2018) Fine-tuning carbapenem resistance by reducing porin permeability of bacteria activated in the selection process of conjugation. *Sci Rep* 8: 15248

Kozakov D, Hall DR, Jehle S, Luo L, Ochiana SO, Jones E v., Pollastri M, Allen KN, Whitty A & Vajda S (2015) Ligand deconstruction: Why some fragment binding positions are conserved and others are not. *Proceedings of the National Academy of Sciences* 112

Krause KM, Serio AW, Kane TR & Connolly LE (2016) Aminoglycosides: An overview. *Cold Spring Harb Perspect Med* 6 (6):a027029

Kricker JA, Page CP, Gardarsson FR, Baldursson O, Gudjonsson T & Parnham MJ (2021) Nonantimicrobial Actions of Macrolides: Overview and Perspectives for Future Development. *Pharmacol Rev* 73: 1404–1433

Krishna SN, Luan C-H, Mishra RK, Xu L, Scheidt KA, Anderson WF & Bergan RC (2013) A Fluorescence-Based Thermal Shift Assay Identifies Inhibitors of Mitogen Activated Protein Kinase Kinase 4. *PLoS One* 8: e81504

Krüger L, Herzberg C, Wicke D, Bähre H, Heidemann JL, Dickmanns A, Schmitt K, Ficner R & Stülke J (2021) A meet-up of two second messengers: the c-di-AMP receptor DarB controls (p)ppGpp synthesis in Bacillus subtilis. *Nat Commun* 12: 1210

Krüger L, Herzberg C, Wicke D, Scholz P, Schmitt K, Turdiev A, Lee VT, Ischebeck T & Stülke J (2022) Sustained Control of Pyruvate Carboxylase by the Essential Second Messenger Cyclic di-AMP in Bacillus subtilis. *mBio* 13(1):e0360221

Kundra S, Lam LN, Kajfasz JK, Casella LG, Andersen MJ, Abranches J, Flores-Mireles AL & Lemos JA (2021) c-di-AMP Is Essential for the Virulence of *Enterococcus faecalis*. *Infect Immun* 89 (11):e0036521

Kuželová K, Grebeňová D, Holoubek A, Röselová P & Obr A (2014) Group I PAK Inhibitor IPA-3 Induces Cell Death and Affects Cell Adhesivity to Fibronectin in Human Hematopoietic Cells. *PLoS One* 9: e92560

Ladbury JE, Klebe G & Freire E (2010) Adding calorimetric data to decision making in lead discovery: a hot tip. *Nat Rev Drug Discov* 9: 23–27

Laemmli UK (1970) Cleavage of Structural Proteins during the Assembly of the Head of Bacteriophage T4. *Nature* 227: 680–685

Lai C-C, Chen S-Y, Ko W-C & Hsueh P-R (2021) Increased antimicrobial resistance during the COVID-19 pandemic. *Int J Antimicrob Agents* 57: 106324

Lamoree B & Hubbard RE (2017) Current perspectives in fragment-based lead discovery (FBLD). *Essays Biochem* 61: 453–464

Lamoree B & Hubbard RE (2018) Using Fragment-Based Approaches to Discover New Antibiotics. *SLAS Discovery* 23: 495–510

Le P, Kunold E, Macsics R, Rox K, Jennings MC, Ugur I, Reinecke M, Chaves-Moreno D, Hackl MW, Fetzer C, *et al* (2020) Repurposing human kinase inhibitors to create an antibiotic active against drug-resistant Staphylococcus aureus, persisters and biofilms. *Nat Chem* 12: 145–158

Lee Ventola C (2015) The Antibiotic Resistance Crisis Part 1: Causes and Threats. P T. 40(4): 277–283.

Li H, Li T, Zou W, Ni M, Hu Q, Qiu X, Yao Z, Fan J, Li L, Huang Q, *et al* (2022) IPA-3: An Inhibitor of Diadenylate Cyclase of Streptococcus suis with Potent Antimicrobial Activity. *Antibiotics* 11: 418

Li L, Wang L, You Q-D & Xu X-L (2020) Heat Shock Protein 90 Inhibitors: An Update on Achievements, Challenges, and Future Directions. *J Med Chem* 63: 1798–1822

Li Q (2020) Application of Fragment-Based Drug Discovery to Versatile Targets. *Front Mol Biosci* 7: 180

Liebschner D, Afonine P v., Baker ML, Bunkóczi G, Chen VB, Croll TI, Hintze B, Hung L-W, Jain S, McCoy AJ, *et al* (2019) Macromolecular structure determination using X-rays, neutrons and electrons: recent developments in *Phenix*. *Acta Crystallogr D Struct Biol* 75: 861–877

Lima GMA, Jagudin E, Talibov VO, Benz LS, Marullo C, Barthel T, Wollenhaupt J, Weiss MS & Mueller U (2021) *FragMAXapp* : crystallographic fragment-screening data-analysis and project-management system. *Acta Crystallogr D Struct Biol* 77: 799–808

Lima GMA, Talibov VO, Jagudin E, Sele C, Nyblom M, Knecht W, Logan DT, Sjögren T & Mueller U (2020) FragMAX: the fragment-screening platform at the MAX IV Laboratory. *Acta Crystallogr D Struct Biol* 76: 771–777

Lipinski CA, Lombardo F, Dominy BW & Feeney PJ (2001) Experimental and computational approaches to estimate solubility and permeability in drug discovery and development settings 1PII of original article: S0169-409X(96)00423-1. The article was originally published in Advanced Drug Delivery Reviews 23 (1997) 3–25. 1. *Adv Drug Deliv Rev* 46: 3–26

Long F, Nicholls RA, Emsley P, Gražulis S, Merkys A, Vaitkus A & Murshudov GN (2017) *AceDRG* : a stereochemical description generator for ligands. *Acta Crystallogr D Struct Biol* 73: 112–122

Luan B & Huynh T (2022) <scp>Crystal-structures-guided</scp> design of <scp>fragment-based</scp> drugs for inhibiting the main protease of <scp>SARS-CoV</scp> -2. *Proteins: Structure, Function, and Bioinformatics* 90: 1081–1089

Lundquist KP, Panchal V, Gotfredsen CH, Brenk R & Clausen MH (2021) Fragment-Based Drug Discovery for RNA Targets. *ChemMedChem* 16: 2588–2603

Ma S, Damfo S, Lou J, Pinotsis N, Bowler MW, Haider S & Kozielski F (2022) Two Ligand-Binding Sites on SARS-CoV-2 Non-Structural Protein 1 Revealed by Fragment-Based X-ray Screening. *Int J Mol Sci* 23 (20):12448

Makman MH & Sutherland EW (1964) Use of Liver Adenyl Cyclase for Assay of Glucagon in Human Gastro-intestinal Tract and Pancreas1. *Endocrinology* 75: 127–134

Mallah N, Orsini N, Figueiras A & Takkouche B (2022) Education level and misuse of antibiotics in the general population: a systematic review and dose–response meta-analysis. *Antimicrob Resist Infect Control* 11: 24

Manikandan K, Sabareesh V, Singh N, Saigal K, Mechold U & Sinha KM (2014) Two-Step Synthesis and Hydrolysis of Cyclic di-AMP in Mycobacterium tuberculosis. *PLoS One* 9: e86096

Martinez JL (2014) General principles of antibiotic resistance in bacteria. *Drug Discov Today Technol* 11: 33–39

Maveyraud L & Mourey L (2020) Protein X-ray Crystallography and Drug Discovery. *Molecules* 25: 1030

Maya-Bernal JL, Ávila A, Ruiz-Gayosso A, Trejo-Fregoso R, Pulido N, Sosa-Peinado A, Zúñiga-Sánchez E, Martínez-Barajas E, Rodríguez-Sotres R & Coello P (2017) Expression of recombinant SnRK1 in E. coli. Characterization of adenine nucleotide binding to the SnRK1.1/AKINβγ-β3 complex. *Plant Science* 263: 116–125

McCoy AJ, Grosse-Kunstleve RW, Adams PD, Winn MD, Storoni LC & Read RJ (2007) *Phaser* crystallographic software. *J Appl Crystallogr* 40: 658–674

McMartin C (1991) Pharmacokinetic requirements for successful site-directed targeting of drugs. *Biotherapy* 3: 9–23

Medina JR, Blackledge CW, Heerding DA, Campobasso N, Ward P, Briand J, Wright L & Axten JM (2010) Aminoindazole PDK1 Inhibitors: A Case Study in Fragment-Based Drug Discovery. *ACS Med Chem Lett* 1: 439–442

Mehne FMP, Gunka K, Eilers H, Herzberg C, Kaever V & Stülke J (2013) Cyclic Di-AMP Homeostasis in Bacillus subtilis. *Journal of Biological Chemistry* 288: 2004–2017

Mehne FMP, Schröder-Tittmann K, Eijlander RT, Herzberg C, Hewitt L, Kaever V, Lewis RJ, Kuipers OP, Tittmann K & Stülke J (2014) Control of the Diadenylate Cyclase CdaS in Bacillus subtilis. *Journal of Biological Chemistry* 289: 21098–21107

Melander RJ & Melander C (2017) The Challenge of Overcoming Antibiotic Resistance: An Adjuvant Approach? *ACS Infect Dis* 3: 559–563

Meyer S, Savaresi S, Forster IC & Dutzler R (2007) Nucleotide recognition by the cytoplasmic domain of the human chloride transporter ClC-5. *Nat Struct Mol Biol* 14: 60–67

Miller JR, Dunham S, Mochalkin I, Banotai C, Bowman M, Buist S, Dunkle B, Hanna D, Harwood HJ, Huband MD, *et al* (2009) A class of selective antibacterials derived from a protein

kinase inhibitor pharmacophore. *Proceedings of the National Academy of Sciences* 106: 1737–1742

Mitchell SL (2018) A Fragment-Based Drug Discovery Approach for the Development of Selective Inhibitors of Protein Kinase CK2

Mittal AK, Bhardwaj R, Mishra P & Rajput SK (2020) Antimicrobials Misuse/Overuse: Adverse Effect, Mechanism, Challenges and Strategies to Combat Resistance. *Open Biotechnol J* 14: 107–112

Müller M, Deimling T, Hopfner K-P & Witte G (2015) Structural analysis of the diadenylate cyclase reaction of DNA-integrity scanning protein A (DisA) and its inhibition by 3′-dATP. *Biochemical Journal* 469: 367–374

Murray CW & Blundell TL (2010) Structural biology in fragment-based drug design. *Curr Opin Struct Biol* 20: 497–507

Murray CW & Rees DC (2009) The rise of fragment-based drug discovery. *Nat Chem* 1: 187–192

Napolitano V, Mróz P, Marciniak M, Kalel VC, Softley CA, Janna Olmos JD, Tippler BG, Schorpp K, Rioton S, Fröhlich T, *et al* (2022) Structure-based design, synthesis and evaluation of a novel family of PEX5-PEX14 interaction inhibitors against Trypanosoma. *Eur J Med Chem* 243: 114778

Nelson JW, Sudarsan N, Furukawa K, Weinberg Z, Wang JX & Breaker RR (2013) Riboswitches in eubacteria sense the second messenger c-di-AMP. *Nat Chem Biol* 9: 834–839

Newman JA, Douangamath A, Yadzani S, Yosaatmadja Y, Aimon A, Brandão-Neto J, Dunnett L, Gorrie-stone T, Skyner R, Fearon D, *et al* (2021) Structure, mechanism and crystallographic fragment screening of the SARS-CoV-2 NSP13 helicase. *Nat Commun* 12: 4848

O'Connor S, le Bihan Y-V, Westwood IM, Liu M, Mak OW, Zazeri G, Povinelli APR, Jones AM, van Montfort R, Reynisson J, *et al* (2022) Discovery and Characterization of a Cryptic Secondary Binding Site in the Molecular Chaperone HSP70. *Molecules* 27: 817

Oldenburg KR, Zhang J-H, Chen T, Maffia A, Blom KF, Combs AP & Chung TDY (1998) Assay Miniaturization for Ultra-High Throughput Screening of Combinatorial and Discrete Compound Libraries: A 9600-Well (0.2 Microliter) Assay System. *SLAS Discovery* 3: 55–62

Olivieri C, Li GC, Wang Y, V.S. M, Walker C, Kim J, Camilloni C, de Simone A, Vendruscolo M, Bernlohr DA, *et al* (2022) ATP-competitive inhibitors modulate the substrate binding cooperativity of a kinase by altering its conformational entropy. *Sci Adv* 8(30):eabo0696

Oltersdorf T, Elmore SW, Shoemaker AR, Armstrong RC, Augeri DJ, Belli BA, Bruncko M, Deckwerth TL, Dinges J, Hajduk PJ, *et al* (2005) An inhibitor of Bcl-2 family proteins induces regression of solid tumours. *Nature* 435: 677–681

O'Neill (2014) Antimicrobial Resistance: Tackling a crisis for the health and wealth of nations

O'Neill (2016) Tackling Drug-resistant infections globally: Final report and recommendations: The review on antimicrobial resistance

van Oosten L (2020) A novel high-throughput and label-free phenotypic drug screening approach: MALDI-TOF mass spectrometry combined with machine learning strategies Referees

Opoku-Temeng C & Sintim HO (2016a) Potent inhibition of cyclic diadenylate monophosphate cyclase by the antiparasitic drug, suramin. *Chemical Communications* 52: 3754–3757

Opoku-Temeng C & Sintim HO (2016b) Inhibition of cyclic diadenylate cyclase, DisA, by polyphenols. *Sci Rep* 6: 25445

Orth P, Xiao L, Hernandez LD, Reichert P, Sheth PR, Beaumont M, Yang X, Murgolo N, Ermakov G, DiNunzio E, *et al* (2014) Mechanism of Action and Epitopes of Clostridium difficile Toxin B-neutralizing Antibody Bezlotoxumab Revealed by X-ray Crystallography. *Journal of Biological Chemistry* 289: 18008–18021

Otten H (1986) Domagk and the development of the sulphonamides. *Journal of Antimicrobial Chemotherapy* 17: 689–690

Pang L, Weeks SD, Juhás M, Strelkov S v., Zitko J & van Aerschot A (2021) Towards Novel 3-Aminopyrazinamide-Based Prolyl-tRNA Synthetase Inhibitors: In Silico Modelling, Thermal Shift Assay and Structural Studies. *Int J Mol Sci* 22: 7793

Papp-Wallace KM, Endimiani A, Taracila MA & Bonomo RA (2011) Carbapenems: Past, present, and future. *Antimicrob Agents Chemother* 55: 4943–4960

Park J, Pandya VR, Ezekiel SJ & Berghuis AM (2021) Phosphonate and Bisphosphonate Inhibitors of Farnesyl Pyrophosphate Synthases: A Structure-Guided Perspective. *Front Chem* 8:612728

Patel D, Bauman JD & Arnold E (2014a) Advantages of crystallographic fragment screening: Functional and mechanistic insights from a powerful platform for efficient drug discovery. *Prog Biophys Mol Biol* 116: 92–100

Pathania M, Tosi T, Millership C, Hoshiga F, Morgan RML, Freemont PS & Gründling A (2021) Structural basis for the inhibition of the Bacillus subtilis c-di-AMP cyclase CdaA by the phosphoglucomutase GlmM. *Journal of Biological Chemistry* 297: 101317

Pearce NM, Krojer T, Bradley AR, Collins P, Nowak RP, Talon R, Marsden BD, Kelm S, Shi J, Deane CM, *et al* (2017a) A multi-crystal method for extracting obscured crystallographic states from conventionally uninterpretable electron density. *Nat Commun* 8: 15123

Pearce NM, Krojer T & von Delft F (2017b) Proper modelling of ligand binding requires an ensemble of bound and unbound states. *Acta Crystallogr D Struct Biol* 73: 256–266

Pedro L & Quinn R (2016) Native Mass Spectrometry in Fragment-Based Drug Discovery. *Molecules* 21: 984

Pereira Moreira B, Weber MHW, Haeberlein S, Mokosch AS, Spengler B, Grevelding CG & Falcone FH (2022) Drug Repurposing and De Novo Drug Discovery of Protein Kinase Inhibitors as New Drugs against Schistosomiasis. *Molecules* 27: 1414

Pham HT, Nhiep NTH, Vu TNM, Huynh TN, Zhu Y, Huynh ALD, Chakrabortti A, Marcellin E, Lo R, Howard CB, *et al* (2018) Enhanced uptake of potassium or glycine betaine or export of cyclic-di-AMP restores osmoresistance in a high cyclic-di-AMP Lactococcus lactis mutant. *PLoS Genet* 14: e1007574

Qiu W, Zhou M, Mazumdar M, Azzi A, Ghanmi D, Luu-The V, Labrie F & Lin S-X (2007) Structure-based Inhibitor Design for an Enzyme That Binds Different Steroids. *Journal of Biological Chemistry* 282: 8368–8379

Rhoads RE (1999) Signal Transduction Pathways That Regulate Eukaryotic Protein Synthesis. *Journal of Biological Chemistry* 274: 30337–30340

Rismondo J, Gibhardt J, Rosenberg J, Kaever V, Halbedel S & Commichau FM (2016) Phenotypes Associated with the Essential Diadenylate Cyclase CdaA and Its Potential Regulator CdaR in the Human Pathogen Listeria monocytogenes. *J Bacteriol* 198: 416–426

Robert X & Gouet P (2014a) Deciphering key features in protein structures with the new ENDscript server. *Nucleic Acids Res* 42: W320–W324

Römling U (2008) Great Times for Small Molecules: c-di-AMP, a Second Messenger Candidate in Bacteria and Archaea. *Sci Signal* 1 (33):pe39

Rørvik GH, Liskiewicz KA, Kryuchkov F, Naemi A-O, Aasheim H-C, Petersen FC, Küntziger TM & Simm R (2020) Cyclic Di-adenosine Monophosphate Regulates Metabolism and Growth in the Oral Commensal Streptococcus mitis. *Microorganisms* 8: 1269

Rosenberg J, Dickmanns A, Neumann P, Gunka K, Arens J, Kaever V, Stülke J, Ficner R & Commichau FM (2015) Structural and Biochemical Analysis of the Essential Diadenylate Cyclase CdaA from Listeria monocytogenes. *Journal of Biological Chemistry* 290: 6596–6606

Ross P, Weinhouse H, Aloni Y, Michaeli D, Weinberger-Ohana P, Mayer R, Braun S, de Vroom E, van der Marel GA, van Boom JH, *et al* (1987) Regulation of cellulose synthesis in Acetobacter xylinum by cyclic diguanylic acid. *Nature* 325: 279–281

Sanchez TW, Ronzetti MH, Owens AE, Antony M, Voss T, Wallgren E, Talley D, Balakrishnan K, Leyes Porello SE, Rai G, *et al* (2022) Real-Time Cellular Thermal Shift Assay to Monitor Target Engagement. *ACS Chem Biol* 17: 2471–2482

Schaenzer AJ, Wlodarchak N, Drewry DH, Zuercher WJ, Rose WE, Striker R & Sauer J-D (2017) A screen for kinase inhibitors identifies antimicrobial imidazopyridine aminofurazans as specific inhibitors of the Listeria monocytogenes PASTA kinase PrkA. *Journal of Biological Chemistry* 292: 17037–17045

Schiavina M, Pontoriero L, Tagliaferro G, Pierattelli R & Felli IC (2022) The Role of Disordered Regions in Orchestrating the Properties of Multidomain Proteins: The SARS-CoV-2 Nucleocapsid Protein and Its Interaction with Enoxaparin. *Biomolecules* 12: 1302

Schuster CF, Bellows LE, Tosi T, Campeotto I, Corrigan RM, Freemont P & Gründling A (2016) The second messenger c-di-AMP inhibits the osmolyte uptake system OpuC in *Staphylococcus aureus*. *Sci Signal* :9(441):ra81

Scott AD, Phillips C, Alex A, Flocco M, Bent A, Randall A, O'Brien R, Damian L & Jones LH (2009) Thermodynamic Optimisation in Drug Discovery: A Case Study using Carbonic Anhydrase Inhibitors. *ChemMedChem* 4: 1985–1989

Selim KA, Haffner M, Burkhardt M, Mantovani O, Neumann N, Albrecht R, Seifert R, Krüger L, Stülke J, Hartmann MD, *et al* (2021) Diurnal metabolic control in cyanobacteria requires perception of second messenger signaling molecule c-di-AMP by the carbon control protein SbtB. *Sci Adv* 7(50):eabk0568

Severin GB & Waters CM (2019) Pyrimidines and Cyclic Trinucleotides Join the Second Messenger Symphony. *Cell Host Microbe* 25: 471–473

Sharma D, Misba L & Khan AU (2019) Antibiotics versus biofilm: an emerging battleground in microbial communities. *Antimicrob Resist Infect Control* 8: 76

Sheikh A, Rafique W, Owais R, Malik F & Ali E (2022) FDA approves Ruxolitinib (Opzelura) for Vitiligo Therapy: A breakthrough in the field of dermatology. *Annals of Medicine and Surgery* 81: 104499

Sherwood AR, Paasch BC, Worby CA & Gentry MS (2013) A malachite green-based assay to assess glucan phosphatase activity. *Anal Biochem* 435: 54–56

Shuker SB, Hajduk PJ, Meadows RP & Fesik SW (1996) Discovering High-Affinity Ligands for Proteins: SAR by NMR. *Science (1979)* 274: 1531–1534

Sink R, Gobec S, Pecar S & Zega A (2010) False Positives in the Early Stages of Drug Discovery. *Curr Med Chem* 17: 4231–4255

Stein N (2008) *CHAINSAW* : a program for mutating pdb files used as templates in molecular replacement. *J Appl Crystallogr* 41: 641–643

Studier FW (2005) Protein production by auto-induction in high-density shaking cultures. *Protein Expr Purif* 41: 207–234

Stülke J & Krüger L (2020) Cyclic di-AMP Signaling in Bacteria. *Annu Rev Microbiol* 74: 159–179

Sugiki T, Furuita K, Fujiwara T & Kojima C (2018) Current NMR Techniques for Structure-Based Drug Discovery. *Molecules* 23: 148

Sureka K, Choi PH, Precit M, Delince M, Pensinger DA, Huynh TN, Jurado AR, Goo YA, Sadilek M, Iavarone AT, *et al* (2014) The Cyclic Dinucleotide c-di-AMP Is an Allosteric Regulator of Metabolic Enzyme Function. *Cell* 158: 1389–1401

Szymański P, Markowicz M & Mikiciuk-Olasik E (2011) Adaptation of High-Throughput Screening in Drug Discovery—Toxicological Screening Tests. *Int J Mol Sci* 13: 427–452

Tang SK, Davey RJ, Sacchi P & Cruz-Cabeza AJ (2021) Can molecular flexibility control crystallization? The case of *para* substituted benzoic acids. *Chem Sci* 12: 993–1000

Tavares IM, Jolly L, Pompeo F, Leitão JH, Fialho AM, Sá-Correia I & Mengin-Lecreulx D (2000) Identification of the *Pseudomonas aeruginosa glmM* Gene, Encoding Phosphoglucosamine Mutase. *J Bacteriol* 182: 4453–4457

Thanassi DG, Cheng LW & Nikaido H (1997) Active efflux of bile salts by Escherichia coli. *J Bacteriol* 179: 2512–2518

Thomas SE, Collins P, James RH, Mendes V, Charoensutthivarakul S, Radoux C, Abell C, Coyne AG, Floto RA, von Delft F, *et al* (2019) Structure-guided fragment-based drug discovery at the synchrotron: screening binding sites and correlations with hotspot mapping. *Philosophical Transactions of the Royal Society A: Mathematical, Physical and Engineering Sciences* 377: 20180422

Thompson CM & Malone JG (2020) Nucleotide second messengers in bacterial decision making. *Curr Opin Microbiol* 55: 34–39

Toledo LM, Lydon NB & Elbaum D (1999) The structure-based design of ATP-site directed protein kinase inhibitors. *Curr Med Chem* 6: 775–805

Tosi T, Hoshiga F, Millership C, Singh R, Eldrid C, Patin D, Mengin-Lecreulx D, Thalassinos K, Freemont P & Gründling A (2019) Inhibition of the Staphylococcus aureus c-di-AMP

cyclase DacA by direct interaction with the phosphoglucosamine mutase GlmM. *PLoS Pathog* 15: e1007537

Tsai J, Lee JT, Wang W, Zhang J, Cho H, Mamo S, Bremer R, Gillette S, Kong J, Haass NK, *et al* (2008) Discovery of a selective inhibitor of oncogenic B-Raf kinase with potent antimelanoma activity. *Proceedings of the National Academy of Sciences* 105: 3041–3046

Vaaltyn MC, Mateos-Jimenez M, Müller R, Mackay CL, Edkins AL, Clarke DJ & Veale CGL (2022) Native Mass Spectrometry-Guided Screening Identifies Hit Fragments for HOP-HSP90 PPI Inhibition. *ChemBioChem* 23(21):e202200322

Verlinde C, Fan E, Shibata S, Zhang Z, Sun Z, Deng W, Ross J, Kim J, Xiao L, Arakaki T, *et al* (2009) Fragment-Based Cocktail Crystallography by the Medical Structural Genomics of Pathogenic Protozoa Consortium. *Curr Top Med Chem* 9: 1678–1687

Viegas A, Macedo AL & Cabrita EJ (2010) Ligand-Based Nuclear Magnetic Resonance Screening Techniques. Methods Mol Biol 572:81-100

Viegas A, Manso J, Nobrega FL & Cabrita EJ (2011) Saturation-Transfer Difference (STD) NMR: A Simple and Fast Method for Ligand Screening and Characterization of Protein Binding. *J Chem Educ* 88: 990–994

Vornhagen J, Burnside K, Whidbey C, Berry J, Qin X & Rajagopal L (2015) Kinase Inhibitors that Increase the Sensitivity of Methicillin Resistant Staphylococcus aureus to β-Lactam Antibiotics. *Pathogens* 4: 708–721

Vuckovic I, Denic A, Charlesworth MC, Šuvakov M, Bobart S, Lieske JC, Fervenza FC & Macura S (2021) ^{1} H Nuclear Magnetic Resonance Spectroscopy-Based Methods for the Quantification of Proteins in Urine. *Anal Chem* 93: 13177–13186

Walsh CT & Fischbach MA (2009) Repurposing libraries of eukaryotic protein kinase inhibitors for antibiotic discovery. *Proceedings of the National Academy of Sciences* 106: 1689–1690

Wang D, Li W, Zhao R, Chen L, Liu N, Tian Y, Zhao H, Xie M, Lu F, Fang Q, *et al* (2019) Stabilized Peptide HDAC Inhibitors Derived from HDAC1 Substrate H3K56 for the Treatment of Cancer Stem–Like Cells *In Vivo*. *Cancer Res* 79: 1769–1783

Wang S, Wang L-J, Jiang B, Wu N, Li X, Liu S, Luo J & Shi D (2015) Anti-Angiogenic Properties of BDDPM, a Bromophenol from Marine Red Alga Rhodomela confervoides, with Multi Receptor Tyrosine Kinase Inhibition Effects. *Int J Mol Sci* 16: 13548–13560

Ward RA, Brassington C, Breeze AL, Caputo A, Critchlow S, Davies G, Goodwin L, Hassall G, Greenwood R, Holdgate GA, *et al* (2012) Design and Synthesis of Novel Lactate Dehydrogenase A Inhibitors by Fragment-Based Lead Generation. *J Med Chem* 55: 3285–3306

Wehrli W (1983) Rifampin: Mechanisms of Action and Resistance. *Clinical Infectious Diseases* 5: S407–S411

Whiteley AT, Eaglesham JB, de Oliveira Mann CC, Morehouse BR, Lowey B, Nieminen EA, Danilchanka O, King DS, Lee ASY, Mekalanos JJ, *et al* (2019) Bacterial cGAS-like enzymes synthesize diverse nucleotide signals. *Nature* 567: 194–199

Whitley MJ, Cardona DM, Lazarides AL, Spasojevic I, Ferrer JM, Cahill J, Lee C-L, Snuderl M, Blazer DG, Hwang ES, *et al* (2016) A mouse-human phase 1 co-clinical trial of a protease-activated fluorescent probe for imaging cancer. *Sci Transl Med* 8 (320):320ra4

WHO (2015) WHO Library Cataloguing-in-Publication Data Global Action Plan on Antimicrobial Resistance

WHO (2019a) No time to wait: Securing the future from drug-resistan infections report to the secretary-general of the united states

WHO (2019b) ANTIBACTERIAL AGENTS IN CLINICAL DEVELOPMENT an analysis of the antibacterial clinical development pipeline.

Wilkins MR, Gasteiger E, Bairoch A, Sanchez J-C, Williams KL, Appel RD & Hochstrasser DF Protein Identification and Analysis Tools in the ExPASy Server. In *2-D Proteome Analysis Protocols* (8) 531–552.

Wilson DM, Deacon AM, Duncton MAJ, Pellicena P, Georgiadis MM, Yeh AP, Arvai AS, Moiani D, Tainer JA & Das D (2021) Fragment- and structure-based drug discovery for developing therapeutic agents targeting the DNA Damage Response. *Prog Biophys Mol Biol* 163: 130–142

Winn MD, Ballard CC, Cowtan KD, Dodson EJ, Emsley P, Evans PR, Keegan RM, Krissinel EB, Leslie AGW, McCoy A, *et al* (2011) Overview of the *CCP* 4 suite and current developments. *Acta Crystallogr D Biol Crystallogr* 67: 235–242

Witte G, Hartung S, Büttner K & Hopfner K-P (2008) Structural Biochemistry of a Bacterial Checkpoint Protein Reveals Diadenylate Cyclase Activity Regulated by DNA Recombination Intermediates. *Mol Cell* 30: 167–178

Wojdyr M, Keegan R, Winter G & Ashton A (2013) *DIMPLE* - a pipeline for the rapid generation of difference maps from protein crystals with putatively bound ligands. *Acta Crystallogr A* 69: 299

Wollenhaupt J, Barthel T, Lima GMA, Metz A, Wallacher D, Jagudin E, Huschmann FU, Hauß T, Feiler CG, Gerlach M, *et al* (2021) Workflow and Tools for Crystallographic Fragment Screening at the Helmholtz-Zentrum Berlin. *Journal of Visualized Experiments* 169

Wollenhaupt J, Metz A, Barthel T, Lima GMA, Heine A, Mueller U, Klebe G & Weiss MS (2020) F2X-Universal and F2X-Entry: Structurally Diverse Compound Libraries for Crystallographic Fragment Screening. *Structure* 28: 694-706

Woodward JJ, Iavarone AT & Portnoy DA (2010) c-di-AMP Secreted by Intracellular *Listeria monocytogenes* Activates a Host Type I Interferon Response. *Science (1979)* 328: 1703–1705

Wyatt PG, Woodhead AJ, Berdini V, Boulstridge JA, Carr MG, Cross DM, Davis DJ, Devine LA, Early TR, Feltell RE, *et al* (2008) Identification of *N* -(4-Piperidinyl)-4-(2,6-dichlorobenzoylamino)-1 *H* -pyrazole-3-carboxamide (AT7519), a Novel Cyclin Dependent Kinase Inhibitor Using Fragment-Based X-Ray Crystallography and Structure Based Drug Design. *J Med Chem* 51: 4986–4999

Wyss DF, Wang Y-S, Eaton HL, Strickland C, Voigt JH, Zhu Z & Stamford AW (2011) Combining NMR and X-ray Crystallography in Fragment-Based Drug Discovery: Discovery of Highly Potent and Selective BACE-1 Inhibitors. Top Curr Chem. 317: 83–114.

Yamamoto KZ, Yasuo N & Sekijima M (2022) Screening for Inhibitors of Main Protease in SARS-CoV-2: In Silico and In Vitro Approach Avoiding Peptidyl Secondary Amides. *J Chem Inf Model* 62: 350–358

Ye Q, Belabed H, Wang Y, Yu Z, Palaniappan M, Li J, Kalovidouris SA, MacKenzie KR, Teng M, Young DW, *et al.* (2022) Advancing ASMS with LC-MS/MS for the discovery of novel PDCL2 ligands from DNA-Encoded chemical library selections. *Andrology* Epub ahead of print

Yue S, Duncan JC, Yama-Moto Y, Hutchinson CR, Knowles JR, Hopwood DA, Lam PYS, Jadhav PK, Eyermann CJ, Hodge CN, *et al.* (1987) Rational Design of Potent, Bioavailable, Nonpeptide Cyclic Ureas as HIV Protease Inhibitors *Science* ;263(5145):380-4

Zarrella TM, Yang J, Metzger DW & Bai G (2020) Bacterial Second Messenger Cyclic di-AMP Modulates the Competence State in Streptococcus pneumoniae. *J Bacteriol* 202 (4):e00691-19

Zhang C, Ibrahim PN, Zhang J, Burton EA, Habets G, Zhang Y, Powell B, West BL, Matusow B, Tsang G, *et al* (2013) Design and pharmacology of a highly specific dual FMS and KIT kinase inhibitor. *Proceedings of the National Academy of Sciences* 110: 5689–5694

Zheng C, Ma Y, Wang X, Xie Y, Ali MK & He J (2015) Functional analysis of the sporulation-specific diadenylate cyclase CdaS in Bacillus thuringiensis. *Front Microbiol* 14;6:908

Zheng Y, Zhou J, Cooper SM, Opoku-Temeng C, de Brito AM & Sintim HO (2016) Structure–activity relationship studies of c-di-AMP synthase inhibitor, bromophenol-thiohydantoin. *Tetrahedron* 72: 3554–3558

Zheng Y, Zhou J, Sayre DA & Sintim HO (2014) Identification of bromophenol thiohydantoin as an inhibitor of DisA, a c-di-AMP synthase, from a 1000 compound library, using the coralyne assay. *Chem Commun* 50: 11234–11237

Zhou J, Sayre DA, Zheng Y, Szmacinski H & Sintim HO (2014) Unexpected Complex Formation between Coralyne and Cyclic Diadenosine Monophosphate Providing a Simple Fluorescent Turn-on Assay to Detect This Bacterial Second Messenger. *Anal Chem* 86: 2412–2420

Zweigenbaum J, Heinig K, Steinborner S, Wachs T & Henion J (1999) High-Throughput Bioanalytical LC/MS/MS Determination of Benzodiazepines in Human Urine: 1000 Samples per 12 Hours. *Anal Chem* 71: 2294–2300

8 Abbreviations

°C	Degree Celsius
3’ OH	3’ hydroxyl
3’3’ cGAMP	Adenosine-Guanosine-3',3'-cyclic monophosphate
3’dATP	3’ deoxy Adenosine triphosphate
5’pApA	5'- Phosphoadenylyl- adenosine
Å	Angstrom ($1Å = 10^{-10}\ m$)
Ala (A)	Alanine
AMP	Adenosine monophosphate
Asp (D)	Aspartic acid
ATP	adenosine triphosphate
Arg (R)	Arginine
BESSY II	Berliner Elektronenspeicherring-Gesellschaft für Synchrotronstrahlung
BDC	Background Density Correction factor
B. subtilis	*Bacillus subtilis*
*Bs*CdaA	*Bacillus subtilis cyclic* di-AMP synthase A
Ca^{2+}	Calcium ion
$CaCl_2$	Calcium chloride
CADD	Computer aided drug design
cAMP	Cyclic adenosine monophosphate
CBS	cystathionine-beta-synthase domain
CC	Coiled-coil
CdaA/DacA	cyclic di-AMP synthase A
CdaM	c-di-AMP synthase of Mycoplasma
CdaR	cyclic di-AMP synthase A regulator
CdaS	cyclic di-AMP synthase S, sporulation-specific
c-di-AMP	Bis-(3'-5')-cyclic dimeric adenosine monophosphate
c-di-GMP	bis-(3’,5’)-cyclic dimeric guanosine monophosphate
CFS	Crystallographic fragment screen
Co^{2+}	Cobalt ion
$CoCl_2$	Cobalt chlorid
C-terminal	Carboxy-terminal
DAC	Diadenylate cyclase

DFG	Deutsche Forschungsgemeinschaft
DESY	Deutsches Elektronen-Synchrotron
DisA	DNA integrity scanning protein A
DMSO	Dimethylsulfoxid
DNA	deoxyribonucleic acid
E. coli	*Escherichia coli*
EDTA	ethylenediaminetetraacetic acid
*Ef*CdaA	*Enterococcus faecium* cyclic di-AMP synthase A
EMBL	European Molecular Biology Laboratory
ESRF	European Synchrotron Radiation Facility
GlmM	phosphoglucoseamine mutase
Glu (E)	Glutamic acid
Gly (G)	Glycine
H1	inhibitory helix 1
H2	inhibitory helix 2
HEPES	4-(2-hydroxyethyl)-1-piperazineethanesulfonic acid
HhH	helix-hinge-helix domain
HZB	Helmholtz-Zentrum Berlin
His (H)	Histidine
IC_{50}	50 % inhibitor concentration
IPTG	isopropyl-β-D-thiogalactopyranosid
Ile (I)	Isoleucine
ITC	Isothermal titration calorimetry
K^+	Potassium ion
K_D	Dissociation constant
kDa	Kilodalton 1 kDa = 1.000 Dalton
LB medium	lysogeny broth medium
Leu (L)	Leucine
L.monocytogenes	*Listeria monocytogenes*
*Lm*CdaA	*Listeria monocytogenes* cyclic di-AMP synthase A
MDR	multidrug efflux pumps
Mg^{2+}	Magnesium ion
$MgCl_2$	Magnesium chloride
min	minute

Mn^{2+}	Manganese ion
$MnCl_2$	Manganese chloride
N-terminus	Amino terminal
OD	Optical density
PanDDA	Pan-Density Dataset Analysis
PAS	Per-Arnt-Sim
PCR	polymerase chain reaction
PDB	Protein Data Bank
PDE	Phosphodiesterase
PEG	Polyethylene glycol
PETRA III	Positron-Elektron-Tandem-Ring-Anlage III
Phe (F)	phenylalanine
p(p)pGpp	guanosine-(penta)-tetraphosphate
PPi	Pyrophosphate
PYK	Pyruvate kinase-like domain
RNA	Ribonucleic acid
rpm	Rounds per minute
SAXS	small-angle x-ray scattering
SDS	sodium dodecyl sulfate
SDS-PAGE	SDS polyacrylamide gel electrophoresis
sec/s	Second
SEC	size exclusion chromatography
Ser (S)	Serine
S. aureus	*Staphylococcus aureus*
*Sa*CdaA	*Staphylococcus aureus* cyclic di-AMP synthase A
S. pneumoniae	*Strepptococcus pneumoniae*
*Sp*CdaA	*Strepptococcus pneumoniae* cyclic di-AMP synthase A
SUMO	small ubiquitin-like modifier
T. maritima	*Thermotoga maritima*
Thr (T)	Threonine
TM	Transmembrane domain
TRIS	tris(hydroxymethyl)aminomethane
wt	Wild type
WHO	World Healthcare organization

9 Acknowledgments

This thesis could have not been accomplished without the support und help which I would like to express my deepest thanks.

Frist of all, I want to thank Prof. Dr. Ralf Ficner for his continuous support and encouragement over the past few years. Thank you for providing a great research environment even during the Covid crisis and letting me develop my own research ideas with guidance. Fruthermore, I would like to thank him for the multiple opportunities to present the results of my work at national and international meetings.

Additionally, I want to thank the members of my thesis committee, Prof. Dr. Kai Tittmann for his ideas and helpful advice regarding and Prof. Dr. Jörg Stülke for his support, discussions and fruitful collaboration. Further, I want to thank Prof. Dr. Carsten Lüder, Prof. Dr. Kai Heimel and Prof. Dr. Ivo Feußner to be part of my examination board.

Furthermore, I would like to thank our collaboration partners from the microbiology department, Prof. Dr. Jörg Stülke and Robert Warnecke for the excellent collaboration. I would also express my gratitude to our collaboration partner from the Helmholz Zentrum Berlin Dr. Manfred Weiss and Dr. Jan Wollenhaupt for all the help and tips concerning planning and exaction of a fragment screen campaign.

I am deeply thankful for the support of Dr. Piotr Neumann. Thank you for continuous answering my questions concerning crystallography in general. Your ideas and advice had a great impact on the work presented here. Our discussions have been inspiring and encouraging, helping me to improve my understanding of crystallography.

Moreover, I want to thank Dr. Achim Dickmanns who always answered my questions regarding technical challenges in the wet lab and your constant efforts to keep the lab running. Your scientific expertise on lab work was always helpful.

Of course, I am very grateful to all present and former members of the Department of Molecular and Structural Biology for the nice working atmosphere. Thanks to Marieke, Alaa, Katharina, Patrick, Kathi, Jana and Flo for the joyful lunch breaks, welcoming environment and walks to the Caphy. I am also grateful to Marita Kalck and Daniel Weinrich for their bureaucratic and technical help and support. Moreover, I want to thank my students Luca Genz, Melin Günzel and Leonie Krause for their contributions to this work.

Thank you all!